NAVAL POSTGRADUATE SCHOOL

MONTEREY, CALIFORNIA

THESIS

AUTOMATED TECHNIQUES FOR RAPID ANALYSIS OF MOMENTUM EXCHANGE DEVICES

by

Reid W. Smythe

December 2013

Co-Advisors: Mark Karpenko
Isaac M. Ross

THIS PAGE INTENTIONALLY LEFT BLANK

REPORT DOCUMENTATION PAGE	Form Approved OMB No. 0704-0188

1. AGENCY USE ONLY *(Leave blank)*	2. REPORT DATE	3. REPORT TYPE AND DATES COVERED
	December 2013	Master's Thesis

4. TITLE AND SUBTITLE	5. FUNDING NUMBERS
AUTOMATED TECHNIQUES FOR RAPID ANALYSIS OF MOMENTUM EXCHANGE DEVICES	
6. AUTHOR(S) Reid W. Smythe	
7. PERFORMING ORGANIZATION NAME(S) AND ADDRESS(ES) Naval Postgraduate School Monterey, CA 93943-5000	**8. PERFORMING ORGANIZATION REPORT NUMBER**
9. SPONSORING /MONITORING AGENCY NAME(S) AND ADDRESS(ES) N/A	**10. SPONSORING/MONITORING AGENCY REPORT NUMBER**

11. SUPPLEMENTARY NOTES The views expressed in this thesis are those of the author and do not reflect the official policy or position of the Department of Defense or the U.S. Government. IRB Protocol number_N/A.

12a. DISTRIBUTION / AVAILABILITY STATEMENT	12b. DISTRIBUTION CODE
Approved for public release; distribution is unlimited	

13. ABSTRACT (maximum 200 words)

This thesis develops a suite of automated techniques aimed at analyzing the characteristics of arrays of control moment gyroscopes (CMGs) and/or reaction wheels (RWs). Three specific areas, relevant to the design of new spacecraft, are examined: momentum space, torque space, and reaction forces. The momentum space analysis creates a maximum saturation envelope for both pure CMG/RW arrays and for hybrid arrays. The torque space analysis creates a maximum envelope for RWs and presents the idea of state-space analysis for CMGs, which leads to the ability to determine singularity free operational envelopes. These envelopes allow satellite slew performance to be estimated, allowing for an initial determination of component size. The reaction forces and moments seen at the attachment points of the RWs and CMGs during maneuvers is also analyzed. This analysis, which has not been reported in the literature, utilizes telemetry data and the geometry of the spacecraft to explore the relationship between maneuver types and the loads seen by the CMG/RW mechanism.

14. SUBJECT TERMS Reaction Wheel, Control Moment Gyroscope, Reaction Forces	15. NUMBER OF PAGES 169
	16. PRICE CODE

17. SECURITY CLASSIFICATION OF REPORT	18. SECURITY CLASSIFICATION OF THIS PAGE	19. SECURITY CLASSIFICATION OF ABSTRACT	20. LIMITATION OF ABSTRACT
Unclassified	Unclassified	Unclassified	UU

NSN 7540-01-280-5500 Standard Form 298 (Rev. 2-89)
Prescribed by ANSI Std. 239-18

THIS PAGE INTENTIONALLY LEFT BLANK

Approved for public release; distribution is unlimited

AUTOMATED TECHNIQUES FOR RAPID ANALYSIS OF MOMENTUM EXCHANGE DEVICES

Reid W. Smythe
Lieutenant, United States Navy
B.S., United States Naval Academy, 2007

Submitted in partial fulfillment of the
requirements for the degree of

MASTER OF SCIENCE IN ASTRONAUTICAL ENGINEERING
AND
ASTRONAUTICAL ENGINEER

from the

NAVAL POSTGRADUATE SCHOOL
December 2013

Author: Reid W. Smythe

Approved by: Mark Karpenko, PhD
Co-Advisor

Isaac M. Ross, PhD
Co-Advisor

Knox T. Millsaps, PhD
Chair, Department of Mechanical and
Aerospace Engineering

THIS PAGE INTENTIONALLY LEFT BLANK

ABSTRACT

This thesis develops a suite of automated techniques aimed at analyzing the characteristics of arrays of control moment gyroscopes (CMGs) and/or reaction wheels (RWs). Three specific areas, relevant to the design of new spacecraft, are examined: momentum space, torque space, and reaction forces. The momentum space analysis creates a maximum saturation envelope for both pure CMG/RW arrays and for hybrid arrays. The torque space analysis creates a maximum envelope for RWs and presents the idea of state-space analysis for CMGs, which leads to the ability to determine singularity free operational envelopes. These envelopes allow satellite slew performance to be estimated, allowing for an initial determination of component size. The reaction forces and moments seen at the attachment points of the RWs and CMGs during maneuvers is also analyzed. This analysis, which has not been reported in the literature, utilizes telemetry data and the geometry of the spacecraft to explore the relationship between maneuver types and the loads seen by the CMG/RW mechanism.

THIS PAGE INTENTIONALLY LEFT BLANK

TABLE OF CONTENTS

LIST OF FIGURES

LIST OF TABLES

THIS PAGE INTENTIONALLY LEFT BLANK

LIST OF ACRONYMS AND ABBREVIATIONS

ACS	attitude control system
CMG	control moment gyroscope
DCM	direction cosine matrix
MED	momentum exchange device
RW	reaction wheel
${}^{y}_{x}R$	DCM from frame x to frame y
${}^{x}v$	vector expressed in frame x
$\omega^{x/y}$	angular rate of frame x with respect to frame y
$\hat{v}$	vector of unit length
$\dot{v}$	vector derivative in its frame
$\ddot{v}$	vector second order derivative in its frame

THIS PAGE INTENTIONALLY LEFT BLANK

ACKNOWLEDGMENTS

I would like to thank the constant efforts by my advisors, Dr. Mark Karpenko and Dr. Isaac Ross, who gave more consideration to the off-the-wall ideas spawned by this research than would normally be advisable and who encouraged me to push beyond material I was comfortable with. Without them, this thesis would have been two-thirds the size and much less interesting.

I must also acknowledge the long list of professors both in and out of SSAG who helped build the foundation of knowledge on which this thesis is based. Without their expertise, this research could not have been completed.

Finally, I would like to thank my wife, Courtney, who was always willing to look at my plots and listen to my explanations whether they were right, wrong or just plain abstruse.

THIS PAGE INTENTIONALLY LEFT BLANK

I. INTRODUCTION

Changing the attitude of an object generally relies on a common technique: modifying its angular momentum. The mechanisms available to effect this change differ depending on whether the object resides in a medium such as air or water or if it exists in a vacuum. Everyday experiences such as the turning of a car or boat or the banking of an airplane have given many people an intuitive feel for how objects react on Earth. This intuition does not translate to objects in space because the motive forces used on Earth are not available: there is nothing in the environment to push off of, hold on to or generate lift from. One solution that has been developed is to trade the angular momentum of the spacecraft with a component mounted inside the spacecraft. This allows the total angular momentum of the system to nominally remain constant, conservation of momentum, while still allowing the spacecraft to spin via momentum transfer. These devices are generally referred to as momentum exchange devices (MEDs).

A. MOMENTUM EXCHANGE DEVICES

Although there are several different types of MEDs, the majority of those used today can be divided into two groups. The first group, reaction wheels (RWs) consist of a relatively large mass (a rotor) mounted on a shaft and attached to a motor. The motor allows the RW to change its angular momentum, by changing the rotational speed of the rotor, and thus the angular momentum of the spacecraft to which the RW is mounted. The second group of momentum exchange devices is single gimbal control moment gyroscopes

(CMGs). The basic idea behind CMGs is to mount a reaction wheel rotating at a nominally constant speed on a second shaft that can gimbal. As the second shaft gimbals, the direction of the momentum vector of the rotating wheel changes, thus changing the angular momentum vector of the spacecraft as a whole. Note that variable speed CMGs can be implemented to combine the characteristics of both RWs and CMGs into one device [1, p. 179].

Combining several MEDs in different orientations results in an MED array and allows control of the spacecraft momentum along additional dimensions.

B. OBJECTIVES AND SCOPE OF THESIS

When conducting an initial design of an attitude control system (ACS), attitude control devices are selected based on the mission of the satellite, gross design characteristics (spin-stabilized, tumbling, three-axis stabilized), mission life and other big picture specifications. Using back-of-the-envelope calculations, initial sizing is performed, and then a simulation is developed to verify and iterate on the decisions. This process continues until a final design has been established that meets various requirements such as mass, performance and service life.

The goal of this thesis is to develop equations and algorithms to help automate the process of analyzing the expected performance of an arbitrary MED array. This will assist in determining an initial component size and location more accurately than back-of-the-envelope computations, based on required performance.

The developed algorithms are designed for ease of implementation in a vector- or matrix-based language such as MATLAB and can utilize the benefits of parallel processing when available.

The initial analyses will consider the well-studied areas of angular momentum and torque. These provide important characteristics of the array performance. By using a clearly defined system to describe the orientation of MEDs inside a spacecraft, universal base equations were derived to eliminate the need for the creation of one-off solutions for a given array. These equations are not restricted by array size or component orientation.

One issue with performing a direct comparison between RWs and CMGs comes from the fact that any torque trajectory for a system of RWs results in a continuous trajectory in state-space. This relationship stems from the fact that torque is not state dependent. This is not the case for CMGs, as the torque available to a CMG at any given moment depends on the current state of the CMG array. To overcome this problem, a state space analysis for CMG arrays is developed as part of this thesis.

The final objective of this work is to examine the reaction forces and moments seen by the MEDs as a spacecraft maneuvers. This particular area has received little to no attention in the literature.

In general, momentum exchange between MEDs and the host spacecraft is discussed in precisely that term: angular momentum of the system as a whole is conserved by exchanging angular momentum between the two bodies. The mechanism for this exchange, however, has a physical

consequence in the form of applied forces and moments on the attachment points between the spacecraft and the MED.

When operating under rigid body assumptions and modeling spacecraft maneuvers, these reactions can be ignored as they are conservative. However, they represent possible failure modes and thus must be either considered when designing the connections, such as bearings, otherwise the connections may be significantly over-engineered adding to cost and mass.

The force analysis will also allow for the comparison between different control laws. This can be useful, for example, if it is desired to extend the life of components by minimizing the peak forces and moments applied during maneuvers through a redesign of the attitude control system.

C. THESIS LAYOUT

Chapter II presents background material necessary to understand the derivations of equations in matrix form rather than vector form.

Chapter III describes the derivation of the equations used to calculate the angular momentum space for RW and CMG arrays. It also presents the momentum inversion algorithm that can be used to find the gimbal angles necessary for a CMG array to orient the maximum net angular momentum vector in a given direction.

Chapter IV derives the equations used to determine RW array torque space. For CMGs, it shows the background and principles behind state space analysis, including the determination of singularity-free momentum space.

Chapter V steps through the derivation of the equations used in the reaction force analysis. This includes determining both the inertial motion of the MED as well as the applied forces and moments used in the force and moment balance equation.

Chapter VI presents several applications of the topics discussed in previous chapters. These applications include both notional array constructs and telemetry from previously validated simulations.

Chapter VII gives the overall conclusions noted from the research and provides some areas that would benefit from future analysis.

THIS PAGE INTENTIONALLY LEFT BLANK

II. MATRIX-BASED SOLUTIONS

Although coordinate transformations and other vector mathematics associated with space systems engineering tends to favor vector or dyadic based solutions, the equivalent matrix form will be used for the derivations in this thesis. The primary purpose for this decision is to allow for simple implementation in matrix-based languages as MATLAB. The bulk of the following derivation is based heavily on Hughes [2, pp. 22-24].

Equation (1) gives one of the most used relationships when analyzing spacecraft dynamics: the transport theorem [1, pg. 12]. It allows a vector expressed in one frame to be differentiated with respect to another frame.

$$ {}^{N}\frac{d}{dt}\left({}^{a}v\right) = {}^{a}\frac{d}{dt}\left({}^{a}v\right) + \omega^{a/N} \times {}^{a}v \tag{1} $$

Equation (1) is generally used to find the inertial derivatives of vectors that are more easily expressed in a non-inertial frame. The equivalent matrix expression, Equation (2), involves transforming the vector into the appropriate frame, then using the product rule to differentiate.

$$ \begin{aligned} {}^{N}v &= {}^{N}_{a}R\,{}^{a}v \\ {}^{N}\dot{v} &= {}^{N}_{a}\dot{R}\,{}^{a}v + {}^{N}_{a}R\,{}^{a}\dot{v} \end{aligned} \tag{2} $$

${}^{N}_{a}R$ is the direction cosine matrix (DCM) that transforms the vector ${}^{a}v$ from the a frame to the N frame.

Although Equations (1) and (2) are mathematically equivalent, Equation (2) is not written in a generally

useful form as the time derivative of the DCM between two frames is not a physically measured quantity. This results in additional computational overhead as that quantity must be calculated. To overcome this, the DCM rate can be rewritten as the product between the DCM and a skew-symmetric matrix of the rotation rates between the frames.

First, consider the non-collinear frames a and N fixed in inertial space and described by the vectrices[1] [2, p. 8] $\{a\}$ and $\{b\}$, defined as Equation (3).

$$\{a\} = \begin{Bmatrix} \hat{a}_1 \\ \hat{a}_2 \\ \hat{a}_3 \end{Bmatrix}, \quad \{b\} = \begin{Bmatrix} \hat{b}_1 \\ \hat{b}_2 \\ \hat{b}_3 \end{Bmatrix} \tag{3}$$

The DCM (R) between the two frames has the properties noted in Equation (4).

$$\begin{aligned} \{a\} &= {}^{a}_{b}R\{b\} \\ \{b\} &= {}^{b}_{a}R\{a\} \\ {}^{b}_{a}R &= {}^{a}_{b}R^{T} = \{b\}\{a\}^{T} \\ {}^{b}_{a}R\,{}^{a}_{b}R &= {}^{a}_{b}R\,{}^{b}_{a}R = I_{3x3} \end{aligned} \tag{4}$$

Now, allow the frames to rotate at different rates with respect to the inertial frame. These rates can be represented by the free vectors $\omega^{a/Inertial}$ and $\omega^{b/Inertial}$. The relative rate between the frames is simply the vector difference between the two as given in Equation (5).

[1] The term vectrix (plural: vectrices) was “coined” by Hughes to describe a convenient notation with which to keep track of the multitude of reference frames used in spacecraft attitude dynamics. They are particularly useful when converting vector equations to their scalar equivalents [1, pg. 522].

$$\begin{aligned}\omega^{a/b} &= \omega^{a/Inertial} - \omega^{b/inertial} \\ \omega^{b/a} &= -\omega^{a/b}\end{aligned} \tag{5}$$

Equation (6) differentiates $\{a\}$ in frame b with respect to time using the transport theorem and gives the expected result.

$$\begin{aligned}{}^{b}\left(\frac{d\{a\}}{dt}\right) &= {}^{a}\left(\frac{d\{a\}}{dt}\right) + \omega^{a/b} \times \{a\} \\ {}^{a}\left(\frac{d\{a\}}{dt}\right) &= 0\end{aligned} \tag{6}$$

Differentiating $\{b\}$ in its own frame with respect to time yields an important equality, shown in Equation (7):

$$\begin{aligned}{}^{b}\left(\frac{d\{b\}}{dt}\right) &= {}^{b}\left(\frac{d\,{}^{b}_{a}R}{dt}\right)\{a\} + {}^{b}_{a}R\,{}^{b}\left(\frac{d\{a\}}{dt}\right) \\ 0 &= {}^{b}_{a}\dot{R}\{a\} + {}^{b}_{a}R\left(\omega^{a/b} \times \{a\}\right) \\ 0 &= \left({}^{b}_{a}\dot{R} + {}^{b}_{a}R\tilde{\omega}^{a/b}\right)\{a\}, \qquad \tilde{\omega}^{a/b} = \begin{bmatrix} 0 & -\omega_3^{a/b} & \omega_2^{a/b} \\ \omega_3^{a/b} & 0 & -\omega_1^{a/b} \\ -\omega_2^{a/b} & \omega_1^{a/b} & 0 \end{bmatrix}\end{aligned} \tag{7}$$

Since $\{a\}$ cannot be zero, this forces the parenthetical sum to add to zero to satisfy the equality in Equation (8).

$$\begin{aligned}0 &= {}^{b}_{a}\dot{R} + {}^{b}_{a}R\tilde{\omega}^{a/b} \\ \tilde{\omega}^{a/N} &= -{}^{b}_{a}\dot{R}\,{}^{b}_{a}R^{T} = {}^{b}_{a}R\,{}^{b}_{a}\dot{R}^{T}\end{aligned} \tag{8}$$

Returning to v, consider v as a free vector in $\mathbb{R}^3$ (Equation (9)).

$$v = \begin{bmatrix} v_1 \\ v_2 \\ v_3 \end{bmatrix} \tag{9}$$

To express the vector in either frame, use the inner product between the vectrix and the vector, given in Equation (10).

$$\begin{aligned} v &= \{a\}^T \, {}^a v \\ v &= \{b\}^T \, {}^b v \end{aligned} \tag{10}$$

This changes Equation (2) to the form found in Equation (11).

$$\begin{aligned} {}^b\frac{d\,{}^a v}{dt} &= {}^b\frac{d\{a\}^T}{dt}\,{}^a v + \{a\}^T \, {}^a\dot{v} \\ &= {}^a\frac{d\{a\}^T \, {}^a v}{dt} + \omega^{a/b} \times \{a\} \, {}^a v \\ &= {}^a\frac{dv}{dt} + \omega^{a/b} \times {}^a v \end{aligned} \tag{11}$$

Equation (11) matches Equation (1), which is an expected result. The penultimate step of Equation (12) involves expressing $\omega^{a/N}$ in terms of frame a and then using matrix identities to rewrite Equation (11) in the same form as Equation (2).

$$\begin{aligned} &\omega^{a/N} = \{a\}^T \, {}^a\omega^{a/N} = \left[{}^a\omega^{a/N} \right]^T \{a\} \\ &{}^N\left(\frac{d\{a\}^T}{dx}\right) = \omega^{a/N} \times \{a\}^T = \left\{ \left[{}^a\omega^{a/N} \right]^T \{a\} \right\}^{\times} \{a\}^T, \quad M^{\times} = \underset{\sim}{M} \\ &\qquad = \{a\}^T \, {}^a\underset{\sim}{\omega}^{a/N} \{a\} \{a\}^T = \{a\}^T \, {}^a\underset{\sim}{\omega}^{a/N} \end{aligned} \tag{12}$$

Finally, combining Equation (10)-(12) gives the desired result in Equation (13).

$$\begin{aligned} \{b\}^T \, {}^b\dot{v} &= \{a\}^T \, {}^a\dot{v} + \{a\}^T \left[{}^a\underset{\sim}{\omega}^{a/b} \right] {}^a v \\ {}^b\dot{v} &= \{N\}\{a\}^T \, {}^a\dot{v} + \{b\}\{a\}^T \left[{}^a\underset{\sim}{\omega}^{a/b} \right] {}^a v \\ {}^b\dot{v} &= {}^b_a R \, {}^a\dot{v} + {}^b_a R \left[{}^a\underset{\sim}{\omega}^{a/b} \right] {}^a v \end{aligned} \tag{13}$$

By inspection with Equation (2), it is clear that Equation (14) holds.

$$\overset{N}{}_{a}\dot{R} = \overset{N}{}_{a}R^{a}\tilde{\omega}^{a/N} \tag{14}$$

A more detailed proof of this fact can be found in Likins [3, pp. 107-110].

Although performing second order derivatives on equations with several rotations can become unwieldy based on the number of terms generated with the product rule, the relatively small number of coordinate frames to be analyzed circumvents this problem. An additional benefit is seen in the removal of the cross-product as a function. This eliminates the need for additional function calls within an equation, improving both readability and speed. It will be necessary, however, to create the skew-symmetric matrices manually, slightly adding to the length of the code.

THIS PAGE INTENTIONALLY LEFT BLANK

III. ANGULAR MOMENTUM SPACE

The momentum space available to an MED array provides an indication of how much momentum the array can exchange with the spacecraft in any given direction, stemming from the fact that by the law of conservation of angular momentum, Equation (15), angular momentum must be conserved in the absence of external torques.

$$h_{total} = h_{S/C} + h_{MED} = const. \tag{15}$$

Physically, this "maximum momentum exchange" value represents the maximum rate the array can cause the spacecraft to spin (or the maximum spacecraft rate that the array can stabilize), shown by Equation (15). The shape of the MED array momentum space is unique to each individual array and is based on both the orientation and the physical and mechanical properties of each MED.

$$h_{S/C} + h_{MED} = J_{S/C}\omega_{S/C} + h_{MED} \tag{15}$$

A. REACTION WHEELS

1. Overview

Consider a perfectly constructed RW rotating about its z-axis, as shown by Figure 1. A scalar calculation of the rotational momentum of the RW is given by Equation (16) [2, pg. 158], assuming the reference frame is body fixed to the RW and lies along the principal axes and the RW is fixed in inertial space.

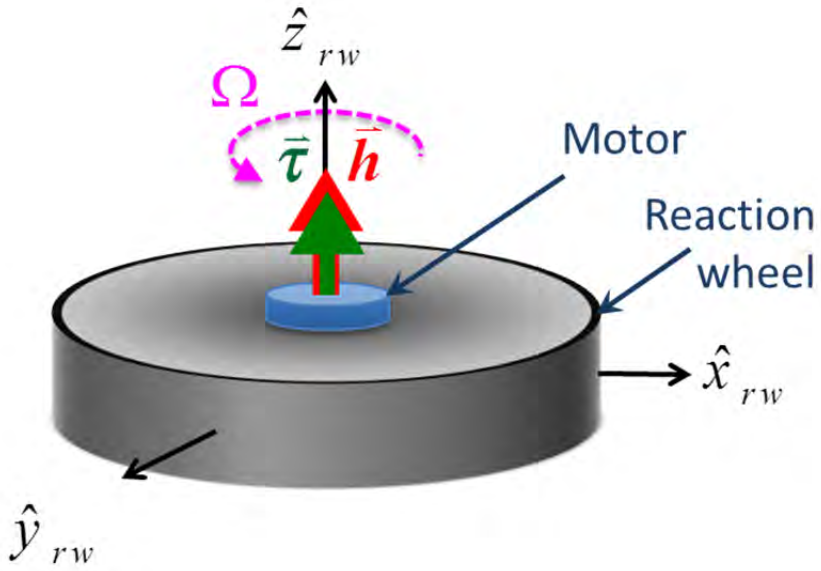

Figure 1. Typical reaction wheel, after [4]

$$h_z = I_z \Omega_{rw} \tag{16}$$

Generalizing to three dimensions, while still assuming the same reference frame as above, yields Equation (17), while Equation (18) gives the most general body fixed case where the principal axes and reference frame axes are not collinear [5, p. 40].

$$\begin{bmatrix} h_x \\ h_y \\ h_z \end{bmatrix} = \begin{bmatrix} I_x & 0 & 0 \\ 0 & I_y & 0 \\ 0 & 0 & I_z \end{bmatrix} \begin{bmatrix} \Omega_x \\ \Omega_y \\ \Omega_{rw} \end{bmatrix} \tag{17}$$

$$\begin{bmatrix} h_x \\ h_y \\ h_z \end{bmatrix} = \begin{bmatrix} I_x & -I_{xy} & -I_{xz} \\ -I_{xy} & I_y & -I_{yz} \\ -I_{xz} & -I_{yz} & I_z \end{bmatrix} \begin{bmatrix} \Omega_x \\ \Omega_y \\ \Omega_{rw} \end{bmatrix} \tag{18}$$

Applying the assumption that the RW spins only about the body z-axis ($\omega_x = \omega_y = 0$) to Equation (17) yields the same as Equation (1), showing that the scalar equation holds only when the body frame and principal axes are aligned (or

aligned close enough to make the products of inertia of negligible magnitude).

2. Converting to the Spacecraft Body Frame

Since Equation (17) only describes how the RW changes angular momentum with respect to its own reference frame, determining what the angular momentum change means to the spacecraft as a whole is the next logical step. Completing that step involves converting the angular momentum vector from the RW frame to the spacecraft body frame. Figure 2 provides a spatial representation of the relationship between the two frames.

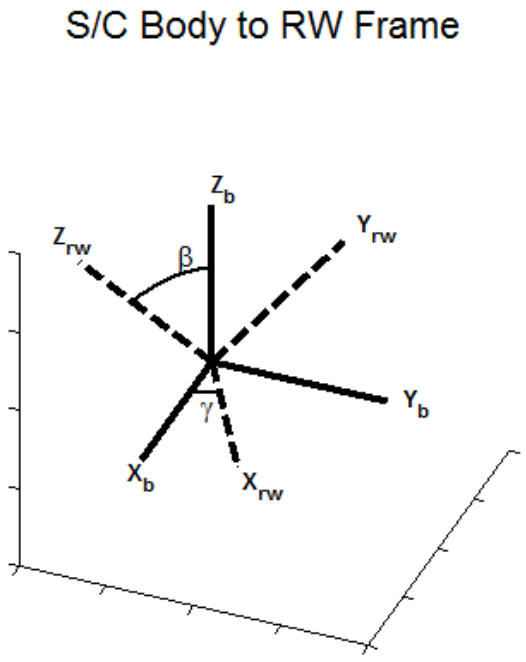

Figure 2. Example Spacecraft Body and RW coordinate systems

Multiplying successive orthonormal rotations creates the necessary DCM. In this case, the first rotation is

about the x_{rw}-axis with a magnitude of -β. The second rotation is about the z_{rw}-axis with a magnitude of -γ. Equation (19) gives the resulting DCM ${}^{b}_{w}R$.

$$
\begin{aligned}
{}^{b}_{w}R &= \begin{bmatrix} \cos(-\gamma) & \sin(-\gamma) & 0 \\ -\sin(-\gamma) & \cos(-\gamma) & 0 \\ 0 & 0 & 1 \end{bmatrix} \begin{bmatrix} 1 & 0 & 0 \\ 0 & \cos(-\beta) & \sin(-\beta) \\ 0 & -\sin(-\beta) & \cos(-\beta) \end{bmatrix} \\
&= \begin{bmatrix} \cos(\gamma) & -\sin(\gamma)\cos(\beta) & -\sin(\gamma)\sin(\beta) \\ \sin(\gamma) & \cos(\beta)\cos(\gamma) & -\cos(\gamma)\sin(\beta) \\ 0 & \sin(\beta) & \cos(\beta) \end{bmatrix}
\end{aligned} \tag{19}
$$

Using the assumptions identified above for the RW, the final relationship between the angular momentum in the two frames is given by Equation (20).

$$
\begin{aligned}
{}^{b}h_{rw} &= {}^{b}_{w}R\,{}^{w}h_{rw} \\
&= \begin{bmatrix} \cos(\gamma) & -\sin(\gamma)\cos(\beta) & -\sin(\gamma)\sin(\beta) \\ \sin(\gamma) & \cos(\beta)\cos(\gamma) & -\cos(\gamma)\sin(\beta) \\ 0 & \sin(\beta) & \cos(\beta) \end{bmatrix} \begin{bmatrix} I_x & 0 & 0 \\ 0 & I_y & 0 \\ 0 & 0 & I_z \end{bmatrix} \begin{bmatrix} \cancel{\Omega}_x \\ \cancel{\Omega}_y \\ \Omega_{rw} \end{bmatrix} \\
&= \begin{bmatrix} \cos(\gamma) & -\sin(\gamma)\cos(\beta) & -\sin(\gamma)\sin(\beta) \\ \sin(\gamma) & \cos(\beta)\cos(\gamma) & -\cos(\gamma)\sin(\beta) \\ 0 & \sin(\beta) & \cos(\beta) \end{bmatrix} \begin{bmatrix} 0 \\ 0 \\ I_z\Omega_{rw} \end{bmatrix} \\
&= \begin{bmatrix} -\sin(\gamma)\sin(\beta) \\ -\cos(\gamma)\sin(\beta) \\ \cos(\beta) \end{bmatrix} I_z\Omega_{rw}
\end{aligned} \tag{20}
$$

The angular momentum in the body frame for the entire RW array is simply the summation of the angular momentum of each individual wheel (Equation (21)).

$$
{}^{b}h_{array} = \sum_{i=1}^{n} {}^{b}h_{rw_i} \tag{21}
$$

Equation (22) provides the vectorized form of Equation (21).

$$ {}^{b}h_{array} = \begin{bmatrix} -\sin(\gamma_1)\sin(\beta_1) & & -\sin(\gamma_n)\sin(\beta_n) \\ -\cos(\gamma_1)\sin(\beta_1) & \cdots & -\cos(\gamma_n)\sin(\beta_n) \\ \cos(\beta_1) & & \cos(\beta_n) \end{bmatrix} \begin{bmatrix} I_{z_1}\Omega_{rw_1} \\ \vdots \\ I_{z_n}\Omega_{z_n} \end{bmatrix} \tag{22} $$

Given a set *k* of different combinations of RW wheel rates, an array of angular momentum points, ${}^{b}\tilde{h}_{array}$, can be created by a matrix form of Equation (22), leading to Equation (23).

$$ {}^{b}\tilde{h}_{array} = \begin{bmatrix} -\sin(\gamma_1)\sin(\beta_1) & & -\sin(\gamma_n)\sin(\beta_n) \\ -\cos(\gamma_1)\sin(\beta_1) & \cdots & -\cos(\gamma_n)\sin(\beta_n) \\ \cos(\beta_1) & & \cos(\beta_n) \end{bmatrix} \begin{bmatrix} I_{z_1} & 0 & 0 \\ 0 & \ddots & 0 \\ 0 & 0 & I_{z_n} \end{bmatrix} \begin{bmatrix} \Omega_{1_1} & & \Omega_{1_k} \\ \vdots & \cdots & \vdots \\ \Omega_{n_1} & & \Omega_{n_k} \end{bmatrix} \tag{23} $$

Use of matrix Equation (23) greatly speeds up execution time in the MATLAB by obviating the need for explicit *for* loops. This allows additional data points to be analyzed in a given amount of time, allowing for a finer analysis.

For the more general case where the wheel frame is not aligned with the principal frame, a slight modification to Equation (22) is required. Although the RW still only spins about the z_{rw}-axis, the coupling from the products of inertia, as seen in Equation (24), results in angular momentum being distributed along all axes in the RW frame.

$$ \begin{aligned} {}^{w}h_{rw} &= \begin{bmatrix} I_x & -I_{xy} & -I_{xz} \\ -I_{xy} & I_y & -I_{yz} \\ -I_{xz} & -I_{yz} & I_z \end{bmatrix} \begin{bmatrix} 0 \\ 0 \\ \Omega_{rw} \end{bmatrix} \\ {}^{w}h_{rw} &= \begin{bmatrix} -I_{xz} \\ -I_{yz} \\ I_z \end{bmatrix} \Omega_{rw} \end{aligned} \tag{24} $$

When converting to the body frame, the entire DCM must now be included rather than just the third column, giving Equations (25) and (26).

$$ {}^{b}h_{rw} = \begin{bmatrix} {}^{b}_{w}R_{rw_1} & {}^{b}_{w}R_{rw_2} & \cdots & {}^{b}_{w}R_{rw_n} \end{bmatrix} \begin{bmatrix} {}^{w}h_{rw_1} \\ {}^{w}h_{rw_2} \\ \vdots \\ {}^{w}h_{rw_n} \end{bmatrix} \tag{25} $$

$$ \begin{aligned} {}^{b}h_{rw} &= {}^{b}_{rw}R\,{}^{w}h_{rw} \\ {}^{b}h_{rw} &= \begin{bmatrix} \cos(\gamma) & -\sin(\gamma)\cos(\beta) & -\sin(\gamma)\sin(\beta) \\ \sin(\gamma) & \cos(\beta)\cos(\gamma) & -\cos(\gamma)\sin(\beta) \\ 0 & \sin(\beta) & \cos(\beta) \end{bmatrix} \begin{bmatrix} -I_{xz} \\ -I_{yz} \\ I_z \end{bmatrix} \Omega_{rw} \end{aligned} \tag{26} $$

In order to create the equivalent form seen in Equation (22), an augmented DCM and column array must be created. It will be of the form seen in Equation (27).

$$ {}^{b}h_{array} = \begin{bmatrix} {}^{b}_{w}R_{rw_1} & {}^{b}_{w}R_{rw_2} & \cdots & {}^{b}_{w}R_{rw_n} \end{bmatrix} \begin{bmatrix} {}^{w}h_{rw_1} \\ {}^{w}h_{rw_2} \\ \vdots \\ {}^{w}h_{rw_n} \end{bmatrix} \tag{27} $$

Finally, to carry out multiple calculations simultaneously, Equation (27) can be expanded as shown in Equation (28).

$$ {}^{b}h_{array} = \begin{bmatrix} {}^{b}_{w}R_{rw_1} & {}^{b}_{w}R_{rw_2} & \cdots & {}^{b}_{w}R_{rw_n} \end{bmatrix} \begin{bmatrix} {}^{w}h_{rw_{1_1}} & \cdots & {}^{w}h_{rw_{1_k}} \\ {}^{w}h_{rw_{2_1}} & \cdots & {}^{w}h_{rw_{2_k}} \\ \vdots & & \vdots \\ {}^{w}h_{rw_{n_1}} & \cdots & {}^{w}h_{rw_{n_k}} \end{bmatrix} \tag{28} $$

Creating the wheel frame angular momentum matrix can be done efficiently by generating it row by row (as in Equation (29)) vice column by column.

$$\begin{bmatrix} {}^{w}h_{rw_{n_1}} & \cdots & {}^{w}h_{rw_{n_k}} \end{bmatrix} = \begin{bmatrix} -I_{XZ_n} \\ -I_{YZ_n} \\ I_{Z_n} \end{bmatrix} \begin{bmatrix} \Omega_{rw_{n_1}} & \cdots & \Omega_{rw_{n_k}} \end{bmatrix} \tag{29}$$

Note that the augmented matrices only give the actual momentum at a specific instant in time. Including the time dependency would additionally require fixing the RW frame to the wheel and keeping track of the angle of rotation over time.

3. Angular Momentum Space

Due to the fact that a maximum wheel speed exists for each RW as a mechanical limitation, there is a limit to the angular momentum magnitude that the array can produce in any given direction. Although methods exist for the analytical determination of the maximum momentum envelope [4], Equation (22) provides a basis for the rapid creation of a large set of momentum points within the momentum space based on a rigorous sweep through all combinations of RW speeds. A simple algorithm can then be used to find the maximal points for all directions around a sphere to determine the angular space for further analysis.

A geometrical approach to creating this volume also exists [6], however the point cloud approach presented here allows additional flexibility when dealing with hybrid RW/CMG arrays.

The momentum space itself assumes that the RW array is fixed to the body which is, in turn, not rotationally accelerating in inertial space. If the array is not fixed, the DCM created in Equation (19) would change over time. Although this can be accounted for by using the appropriate

time history of the angles associated with the DCM, the shape of the momentum space itself would change over time. Similarly, if the array had a rotational acceleration component in inertial space then this acceleration would have to be included in the wheel speed term, affecting the momentum vector direction for each RW changing the net momentum vector direction for the RW array as a whole, thus affecting the shape of the momentum space.

Although this seems to indicate that the momentum envelope would, in general, not apply since the spacecraft is always accelerating in inertial space, the magnitude of spacecraft rotation is much less than the magnitude of wheel rotation so the effect of the spacecraft rotation on the momentum space of the RW array is, in fact, negligible.

B. CONTROL MOMENT GYRO ANGULAR MOMENTUM

1. Overview

Although the basic principles for determining the angular momentum of a CMG matches those used for a reaction wheel, the extra degree of freedom of the CMG slightly complicates the equations. The rotor now rotates about the local x-axis, which is the CMG body-centered direction of the angular momentum vector, shown in Figure 3.

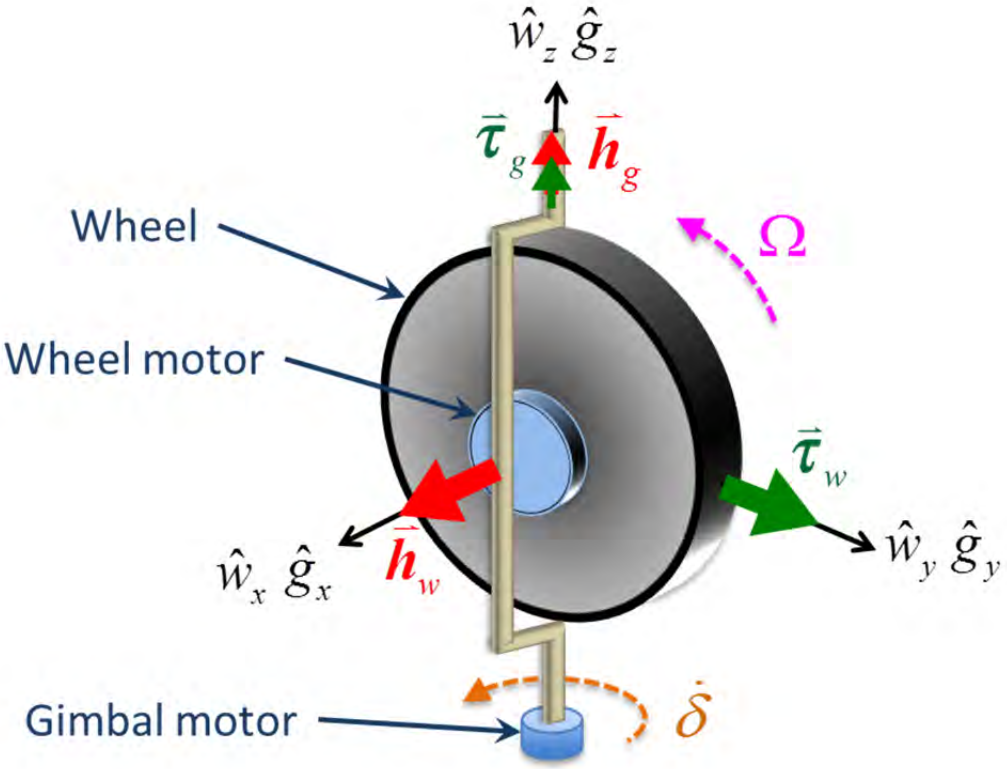

Figure 3. Typical CMG, from [4]

The CMG gimbal rotates about the local z-axis, and this rotation must be accounted for when converting the angular momentum from the gimbal frame of the CMG to the spacecraft body frame. This rotation is accomplished by performing a z-axis rotation in the opposite direction of the gimbal angle, δ, prior to doing the first rotation from Equation (19). The additional rotation is included in Equation (30).

$$
{}^{b}_{g}R = \begin{bmatrix} \cos(-\gamma) & \sin(-\gamma) & 0 \\ -\sin(-\gamma) & \cos(-\gamma) & 0 \\ 0 & 0 & 1 \end{bmatrix} \begin{bmatrix} 1 & 0 & 0 \\ 0 & \cos(-\beta) & \sin(-\beta) \\ 0 & -\sin(-\beta) & \cos(-\beta) \end{bmatrix} \begin{bmatrix} \cos(-\delta) & \sin(-\delta) & 0 \\ -\sin(-\delta) & \cos(-\delta) & 0 \\ 0 & 0 & 1 \end{bmatrix}
$$

$$
= \begin{bmatrix} \cos(\delta)\cos(\gamma) - \cos(\beta)\sin(\delta)\sin(\gamma) & -\cos(\gamma)\sin(\delta) - \cos(\beta)\cos(\delta)\sin(\gamma) & \sin(\beta)\sin(\gamma) \\ \cos(\delta)\sin(\gamma) + \cos(\beta)\cos(\gamma)\sin(\delta) & \cos(\beta)\cos(\delta)\cos(\gamma) - \sin(\delta)\sin(\gamma) & -\cos(\gamma)\sin(\beta) \\ \sin(\beta)\sin(\delta) & \cos(\delta)\sin(\beta) & \cos(\beta) \end{bmatrix}
$$

(30)

The final equation for determining the orientation of the angular momentum vector for a CMG in the spacecraft body frame can thus be determined, as shown in Equation (31) (or by the more general form of Equation (32)).

$$
{}^{b}h_{cmg} = {}^{b}_{g}R\,{}^{g}h_{cmg} = {}^{b}_{g}R \begin{bmatrix} I_r & 0 & 0 \\ 0 & I_y & 0 \\ 0 & 0 & I_z \end{bmatrix} \begin{bmatrix} \Omega_r \\ \cancel{\Omega}_y \\ \cancel{\Omega}_z \end{bmatrix} = {}^{b}_{g}R \begin{bmatrix} I_r\Omega_r \\ 0 \\ 0 \end{bmatrix} \tag{31}
$$

$$
{}^{b}h_{cmg} = {}^{b}_{g}R\,{}^{g}h_{cmg} = {}^{b}_{g}R \begin{bmatrix} I_r & -I_{ry} & -I_{rz} \\ -I_{ry} & I_y & -I_{yz} \\ -I_{rz} & -I_{yz} & I_z \end{bmatrix} \begin{bmatrix} \Omega_r \\ \cancel{\Omega}_y \\ \cancel{\Omega}_z \end{bmatrix} = {}^{b}_{g}R \begin{bmatrix} I_r \\ -I_{ry} \\ -I_{rz} \end{bmatrix} \Omega_r \tag{32}
$$

2. Angular Momentum Space

a. Momentum Inversion Algorithm (MIA)

Although a sweep analysis through all possible combinations of gimbal angles would provide a similarly maximal result as that performed for the reaction wheels, the presence of singular surfaces [7] presented an opportunity to develop a more unique approach that greatly improves the speed with which the analysis is conducted. Essentially, this technique is an inversion of the CMG array angular momentum equations typically seen in literature, such as Equation (33) [8, p. 466].

$$\mathbf{h} = \sum_{i=1}^{4} \mathbf{H}_i(\delta_i)$$
$$= \begin{bmatrix} -\cos(\beta)\sin(\delta_1) \\ \cos(\delta_1) \\ \sin(\beta)\sin(\delta_1) \end{bmatrix} + \begin{bmatrix} -\cos(\delta_2) \\ -\cos(\beta)\sin(\delta_2) \\ \sin(\beta)\sin(\delta_2) \end{bmatrix} + \begin{bmatrix} \cos(\beta)\sin(\delta_3) \\ -\cos(\delta_3) \\ \sin(\beta)\sin(\delta_3) \end{bmatrix} + \begin{bmatrix} \cos(\delta_4) \\ \cos(\beta)\sin(\delta_4) \\ \sin(\beta)\sin(\delta_4) \end{bmatrix} \quad (33)$$

The basis for the MIA analysis lies in the fact that maximizing the amount of angular momentum each individual CMG places in the desired direction will yield a maximum result for the array as a whole. This allows the overall problem to be decomposed into n smaller problems, where the direction vector is projected onto the rotational plane of each CMG in the array to determine the appropriate gimbal angle for that CMG to maximize the momentum it places in the desired direction. The momentum vectors for each CMG are then added, resulting in a least squares solution to the inversion problem. Figure 4 shows the result of this algorithm on a four CMG array.

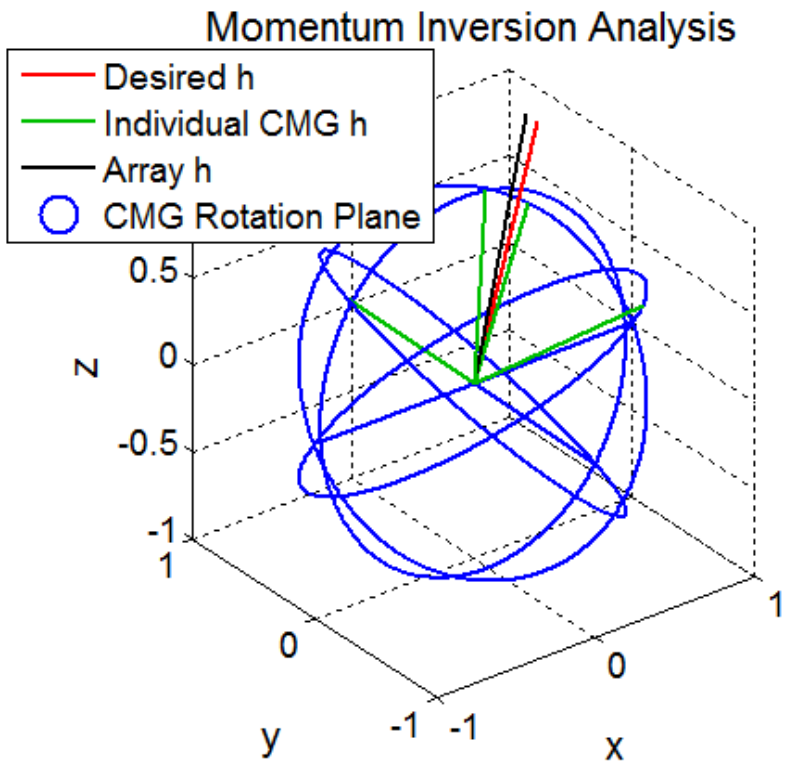

Figure 4. Schematic of the inversion algorithm

For the i^{th} CMG, consider Equation (30), rewritten in the standard $Ax = b$ form as Equation (34). In this case, $\hat{d}$ is the unit vector along the desired angular momentum direction, Δ is the unknown gimbal angle vector, and K is the remainder of the matrix from Equation (30).

$$\underbrace{\begin{bmatrix} \cos(\gamma) & -\sin(\gamma)\cos(\beta) & -\sin(\gamma)\sin(\beta) \\ \sin(\gamma) & \cos(\beta)\cos(\gamma) & -\cos(\gamma)\sin(\beta) \\ 0 & \sin(\beta) & \cos(\beta) \end{bmatrix}}_{K} \underbrace{\begin{bmatrix} \cos(\delta) \\ \sin(\delta) \\ 0 \end{bmatrix}}_{\Delta} = \hat{d} \qquad (34)$$

One problem that becomes immediately apparent is the fact that in Equation (34), there is only one angle being solved for. Using standard methods for solving the problem will not work since, in the absence of additional constraints, they will treat the two terms as decoupled and

solve one independently of the other. Analyzing this problem in a vectoral manner provides a means to move forward. Figure 5 represents the initial problem for a single CMG.

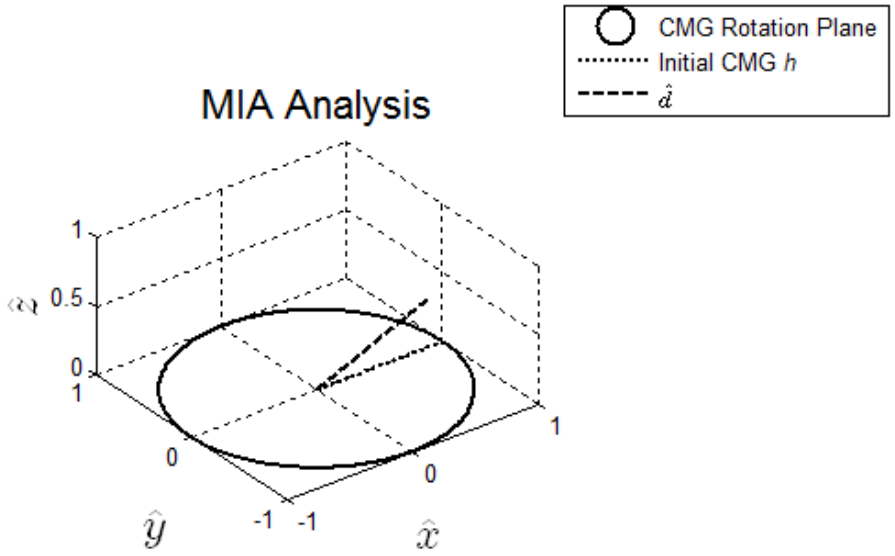

Figure 5. Gimbal rotation plane and desired direction vector in the CMG frame

Geometrically, the left hand side of Equation (34) describes a plane in the spacecraft body frame. Figure 5 provides a visual example of this, with the circle describing the possible orientations of the CMG angular momentum vector and $\hat{d}$ describing the desired angular momentum direction. If $\hat{d}$ lies in the rotation plane, the CMG can orient itself such that its angular momentum vector lies parallel to the direction of $\hat{d}$. If $\hat{d}$ does not lie in the rotational plane, then the ideal direction for the angular momentum vector would be along the projection of $\hat{d}$

onto the plane. To do the projection, the normal (n^+) and anti-normal (n^-) vectors are calculated based on the momentum directions at two orthogonal gimbal angles, such as 0° and 90° ($\Delta(0°)$ and $\Delta(90°)$ respectively), shown in Equation (35) and diagrammatically by Figure 6.

$$\hat{n}^+ = K\Delta(0°)\times K\Delta(90°)$$
$$\hat{n}^- = K\Delta(90°)\times K\Delta(0°) \tag{35}$$

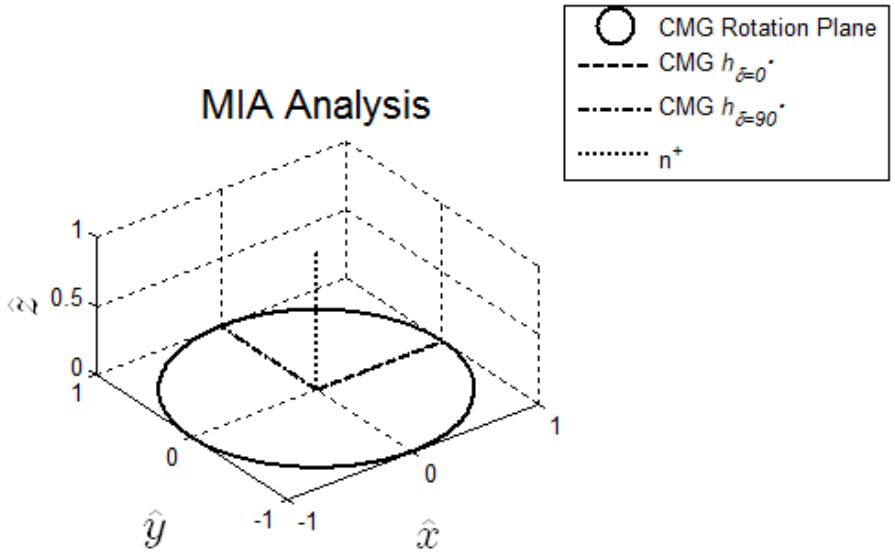

Figure 6. Finding the Rotation Plane Normal Vectors

The appropriate normal or anti-normal vector is chosen such that the relationship given in equation (36) is satisfied.

$$\hat{n}\bullet\hat{d} \geq 0 \tag{36}$$

The projection can now be determined by subtracting the perpendicular component in Equation (37) and Figure 7.

$$\hat{d}_{proj} = \frac{\hat{d} - \left(\hat{n} \bullet \hat{d}\right)\hat{n}}{\left\| \hat{d} - \left(\hat{n} \bullet \hat{d}\right)\hat{n} \right\|} \tag{37}$$

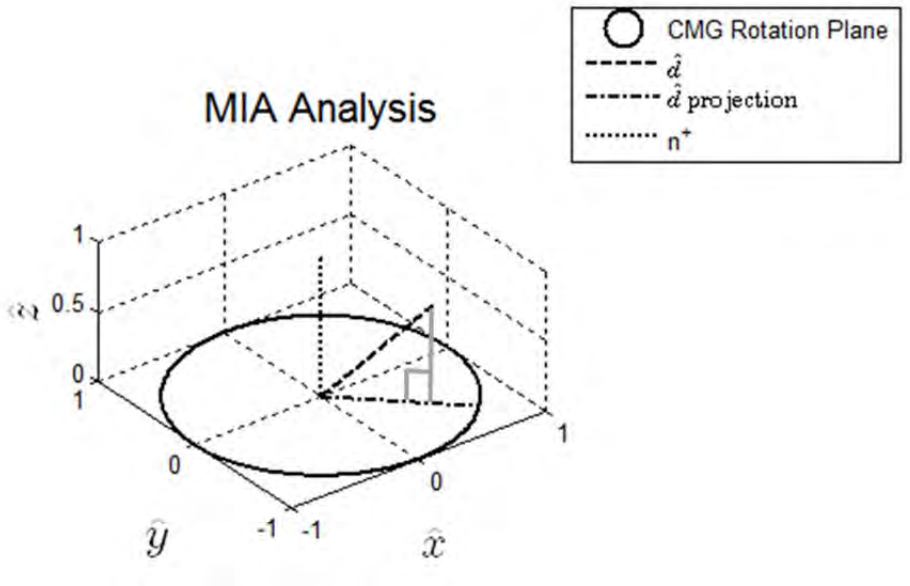

Figure 7. Projecting $\hat{d}$ onto the Rotation Plane

The least squares gimbal angle can thus be calculated using Equation (38), as described in Figure 8.

$$\delta_f = \begin{cases} \cos^{-1}\left(K\Delta(0°) \bullet \hat{d}_{proj}\right) & if \left(K\Delta(0°) \times \hat{d}_{proj}\right) \bullet \hat{n}^+ \geq 0 \\ 360° - \cos^{-1}\left(K\Delta(0°) \bullet \hat{d}_{proj}\right) & otherwise \end{cases} \tag{38}$$

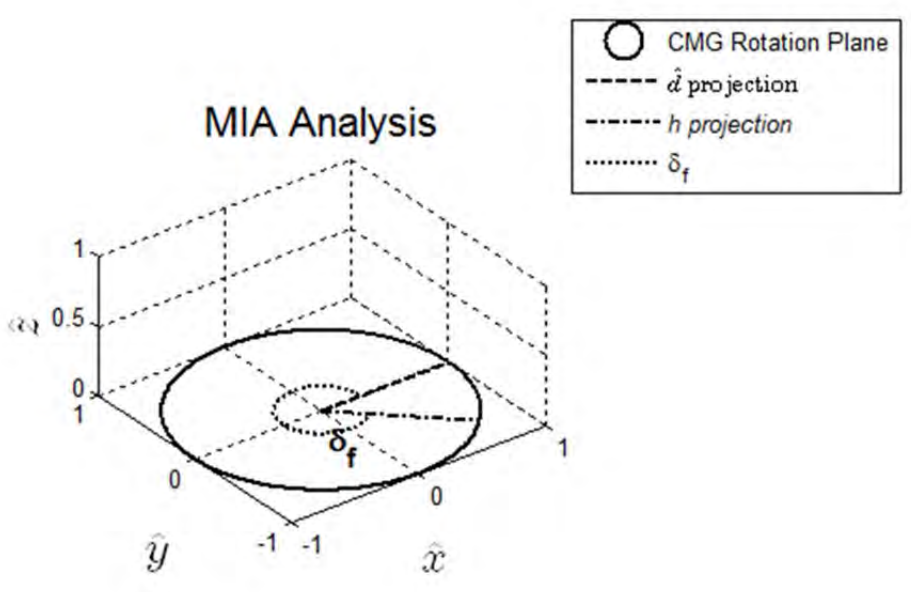

Figure 8. Determining the Gimbal Angle of the Projection

The resulting CMG momentum vector described by placing the CMG at the calculated gimbal angle provides the least squares solution for that particular CMG. Orienting the CMG at any other gimbal angle would increase the norm of the difference between the normalized CMG momentum vector and the normalized direction vector. Performing the same algorithm on each of the other CMGs in the array provides the individual least squares solution for those CMGs as well. Summing the momentum vectors provided by those solutions gives a net momentum vector for the array.

As seen in Figure 4 there may be some angular difference (or angle residual) between the desired direction and the least squares net momentum vector. It is possible to construct equations that calculate this angle residual as a function of solved gimbal angles. This equation can be used with a numeric solver to reduce the residual to near zero and thus determine a quasi-least

squares gimbal angle solution for any given direction in which a solution exists (a solution will not exist, for example, in a direction that is perpendicular to the rotational planes of all CMGs). In effect, the preceding algorithm simply provides an initial guess so that a numeric solver can find a set of gimbal angles that give a near maximum net momentum vector for a CMG array. This, therefore, allows for the construction of a quasi-maximal surface by sweeping around a sphere rather than sweeping through all possible gimbal angle combinations.

b. MIA Angle Correction

Assuming unit momentum, the momentum vector for each CMG is calculated via Equation (39), using the gimbal angle given by Equation (38).

$$\begin{bmatrix} \cos(\gamma) & -\sin(\gamma)\cos(\beta) & -\sin(\gamma)\sin(\beta) \\ \sin(\gamma) & \cos(\beta)\cos(\gamma) & -\cos(\gamma)\sin(\beta) \\ 0 & \sin(\beta) & \cos(\beta) \end{bmatrix} \begin{bmatrix} \cos(\delta) \\ \sin(\delta) \\ 0 \end{bmatrix} = {}^{b}\hat{h}_{cmg} \tag{39}$$

Since all vectors are known at this point, the angle residual can be determined using the dot product definition in Equation (40).

$$\theta_{res} = \cos^{-1}\left(\hat{d} \bullet {}^{b}\hat{h}_{cmg}\right) \tag{40}$$

If θ_{res} falls outside of a given threshold, the dot product itself can be used to solve for the gimbal angles that reduce the residual to near zero based on the identity given in Equation (41).

$$\begin{aligned} &\hat{u} \parallel \hat{v} \\ &\hat{u} \bullet \hat{v} = 1 \end{aligned} \tag{41}$$

Therefore, when the angle residual is zero, Equation (42) will be true.

$$\hat{d} \bullet {}^{b}\hat{h}_{cmg} - 1 = 0 \tag{42}$$

Rapidly finding the solution to Equation (42) is well within the capability of modern numerical solvers, assuming the solution exists.

If the products of inertia are non-zero for the CMG wheel, the angular momentum vector will be offset from the spin axis of the rotor. This will induce an error not taken into account by the equations as developed. In general, the products of inertia will be orders of magnitude smaller than the moments of inertia, greatly reducing the size of the error. To correct for this error, the projection of the angular momentum onto the rotational plane should be used in place of $K\Delta$.

c. Momentum Space Analysis

A maximum momentum surface for the CMG array based on the MIA can now be quickly constructed. Similar to finding the maximum surface for RW arrays given a point cloud, the first step involves creating a unit sphere with the point density determining the fidelity of the CMG surface construction. Iteration through the spherical envelope provides the direction vectors for the algorithm.

The output of the algorithm provides both a maximal surface for all analyzed directions, as well as an angle residual which gives a measurement for how well the CMG array can point its momentum vector in a given direction.

C. SUMMARY

This chapter developed the equations and algorithms necessary to create maximum momentum volumes for both RW and CMG arrays. These momentum volumes can be used to estimate the maximum theoretical performance of an arbitrary array and for more advanced techniques such as the analysis of hybrid arrays and performance comparison between gimbal angle-limited singularity free CMG array momentum volumes.

THIS PAGE INTENTIONALLY LEFT BLANK

IV. TORQUE SPACE

A. OVERVIEW

The general equation of motion for a spacecraft is given by Equations (43) and (44) [8, p. 463], where J is the total moment of inertia of the system, ω is the spacecraft body rate vector and ${}^{b}h_{MED}$ is the MED momentum vector expressed in the spacecraft body frame.

$$ {}^{b}\dot{H}_{s} + \omega^{b/N} \times {}^{b}H_{s} = {}^{b}\tau_{ext} \tag{43} $$

$$ {}^{b}H_{s} = J\omega^{b/N} + {}^{b}h_{MED} \tag{44} $$

Substituting Equation (44) into Equation (43) and assuming a torque-free environment yields Equation (45) [8, p. 463]:

$$ \left(J\dot{\omega}^{b/N} + {}^{b}\dot{h}_{MED}\right) + \omega^{b/N} \times \left(J\omega^{b/N} + {}^{b}h_{MED}\right) = 0\,. \tag{45} $$

Equation (45) can then be rewritten to separate the spacecraft terms and the MED terms, shown in Equations (46) -(48).

$$ \left[J\dot{\omega}^{b/N} + \omega^{B/N} \times J\omega^{b/N}\right]_{S/C} + \left[{}^{b}\dot{h}_{MED} + \omega^{b/N} \times {}^{b}h_{MED}\right]_{MED} = 0 \tag{46} $$

$$ {}^{b}h_{MED} = {}^{b}h_{rw} + {}^{b}h_{cmg} \tag{47} $$

$$ {}^{b}\dot{h} = {}^{b}\dot{h}_{rw} + {}^{b}\dot{h}_{cmg} \tag{48} $$

Recalling Equations (16)-(18) and applying them to Equation (47) yields Equation (49). Equations (46)-(49) hold regardless of the reference frame they are expressed in, so long as all terms are expressed in a consistent frame.

$$h_{MED} = I_{rw}\Omega_{rw} + I_{cmg}\Omega_r \tag{49}$$

Equation (49) allows Equation (46) to be further generalized into Equation (50).

$$\begin{aligned}&\left[J\dot{\omega}^{b/N} + \omega^{b/N} \times J\omega^{b/N}\right]_{S/C} + \\ &\left[\dot{I}_{rw}\omega^{rw/N} + I_{rw}\dot{\omega}^{rw/N} + \dot{I}_{cmg}\omega^{cmg/N} + I_{cmg}\dot{\omega}^{cmg/N} + \omega^{b/N} \times \left(I_{rw}\omega^{rw/N} + I_{cmg}\omega^{cmg/N}\right)\right]_{MED} = 0\end{aligned} \tag{50}$$

Equation (50) can be expressed by Equation (51) by assuming that $\dot{I}_{RW} = 0$ in the spacecraft body frame. This is a reasonable assumption as reaction wheels will be nearly axisymmetric about their spin axis, which is fixed in the body frame. Note that there is also the implicit assumption that the overall inertia of the spacecraft, J, is much greater than I_{CMG}, so it will remain roughly constant. Since the CMG terms are much more complex, they will be folded back into quantities that will be developed separately [8, p. 464].

$$\begin{aligned}&{}^b\left[J\dot{\omega}^{b/N} + \omega^{b/N} \times J\omega^{b/N}\right]_{S/C} = {}^b\left[\tau_{rw} + \tau_{cmg}\right] \\ &{}^b\left[I_{rw}\dot{\omega}^{rw/N} + \omega^{b/N} \times \left(I_{rw}\omega^{rw/N}\right)\right] = -{}^b\tau_{rw} \\ &{}^b\dot{h}_{cmg} + \omega^{b/N} \times {}^b h_{cmg} = -{}^b\tau_{cmg}\end{aligned} \tag{51}$$

B. REACTION WHEELS

1. Derivation

Although Equation (51) provides a method for determining the inertial torque for the MED arrays, analyzing the torque capability in the body frame (as was done for momentum in Equation (23)) removes the complication of having to include inertial motion.

Equation (52) provides the relationship between momentum and torque within the local wheel frame.

$$ {}^{w}\dot{h} = {}^{w}\tau \tag{52} $$

Recalling Equation (16), Equation (52) becomes Equation (53):

$$ {}^{w}\tau = {}^{w}\left[\dot{I}_{rw}\omega^{rw/N} + I_{rw}\dot{\omega}^{rw/N} \right]. \tag{53} $$

The RW is axisymmetric about its spin axis, so the wheel inertia will remain constant. Converting to the body frame is done in a similar matter as done for momentum, as given by Equation (54).

$$ {}^{b}\tau = {}^{b}_{w}\dot{R}\,{}^{w}\left[I_{rw}\omega^{rw/N} \right] + {}^{b}_{w}R\,{}^{w}\left[I_{rw}\dot{\omega}^{rw/N} \right] \tag{54} $$

Since the wheel frame is fixed with respect to the body frame, the DCM remains constant, yielding the final torque equation, Equation (55), for a single RW.

$$ {}^{b}\tau = {}^{b}_{w}R\,{}^{w}\left[I_{rw}\dot{\omega}^{rw/N} \right] \tag{55} $$

Assuming the body is not accelerating in inertial space, Equation (55) can be reduced to Equation (56), which, as expected, is the time derivative of Equation (20) .

$$ {}^{b}\tau = {}^{b}_{w}R\,{}^{w}\left[I_{rw} \right] \begin{bmatrix} 0 \\ 0 \\ \dot{\Omega}_{rw} \end{bmatrix} \tag{56} $$

To determine the torque generated by the entire array, Equations (21) and (23) can be differentiated and rewritten as Equations (57) and (58).

$$ {}^{b}\tau_{array} = \sum_{i=1}^{n} {}^{b}\tau_{rw_i} \tag{57} $$

$$ {}^{b}\tilde{\tau}_{array} = \begin{bmatrix} -\sin(\gamma_1)\sin(\beta_1) & & -\sin(\gamma_n)\sin(\beta_n) \\ -\cos(\gamma_1)\sin(\beta_1) & \cdots & -\cos(\gamma_n)\sin(\beta_n) \\ \cos(\beta_1) & & \cos(\beta_n) \end{bmatrix} \begin{bmatrix} I_{z_1} & 0 & 0 \\ 0 & \ddots & 0 \\ 0 & 0 & I_{z_n} \end{bmatrix} \begin{bmatrix} \dot{\Omega}_{1_1} & & \dot{\Omega}_{1_k} \\ \vdots & \cdots & \vdots \\ \dot{\Omega}_{n_1} & & \dot{\Omega}_{n_k} \end{bmatrix} \tag{58} $$

A maximal torque space can then be developed via the same method used to develop the maximal momentum space.

Since the geometry of the RW array does not change with respect to the body, the shape resulting from Equation (57) will be similar to the shape developed by Equation (23).

C. CMGS

Although the torque-momentum relationship given in Equation (52) holds for CMGs as well, the resulting derivative is more complex due to the time variant gimbal angle, δ. This additional degree of freedom causes the available torque to become state dependent. In other words, each individual CMG configuration has its own torque space. Among other problems, this makes visualization difficult as the torque currently available to the CMG array is not a constant function of the gimbal angle and will change with time and for each gimbal trajectory.

Traditionally, this issue causes most analyses to be conducted on the momentum space of CMG arrays, and significant work has been done in that area [9;10;11;12;8, pp. 466-470]. In particular, much of the work has focused on singularity analysis and either developing control laws

to avoid singularities or to create CMG arrays that minimize singularities [12]. An alternative analysis involves looking at the state space of the array.

Developing a state space analysis for CMG arrays is numerically intensive, especially if a high fidelity is desired. Furthermore, there is an issue of dimensionality. By definition, a state dependent plot of available torque would describe the momentum output of the array for each gimbal angle and gimbal rate. When considering a four wheel array, this implies there are eight input dimensions that must be mapped onto three output dimensions.

Despite the problems associated with working in state space, there are several benefits that can be realized. For example, by identifying regions of the space that are composed exclusively of non-singular states it is possible to constrain the allowable gimbal angles for the array so that the basic pseudoinverse control law is sufficient to maneuver the satellite. Without constraining the gimbal angles, this approach would normally result in the loss of control of the spacecraft after a short period of time due to singularities. Another option would be to select a larger region by allowing only hyperbolic singularities to be included, as these can be avoided by standard techniques such as adding null motion to the pseudoinverse control law [8, p. 468].

1. State Space Analysis

Equation (59) represents one of the key assumptions for this analysis. This assumption allows the input dimensionality to be reduced by half, greatly shrinking the scope of the problem. There is still the issue of

visualizing data that lives in $\mathbb{R}^{n+3}$, however, where n is the number of CMGs in the array. By constraining the output of the analysis to be a scalar rather than a vector, the three output dimensions can be further reduced to one. This will result in the loss of some information; however the information may be unnecessary, depending on the particular analysis performed.

$$\ddot{\delta} \gg \dot{\delta} \tag{59}$$

2. Contiguousness

At this point, it is necessary to introduce the concept of contiguousness. In this thesis, a state space analysis representation is considered contiguous if all continuous trajectories that can be traced in the state space are physically realizable. When analyzing a single CMG, it would require some effort to present a state space visualization that is not contiguous. When reducing dimensionality during a CMG array analysis, however, it is very important to keep this property in mind. When considering the problem at hand, developing gimbal angle limits to achieve a singularity free operational momentum space for a CMG array, a non-contiguous analysis may allow for a state within this space that can only physically be reached by violating gimbal angle limits.

For example, consider a four CMG array. Using the previously discussed assumptions, the state space of this array can be reduced from $\mathbb{R}^{11}$ to $\mathbb{R}^{5}$. To convert this down to $\mathbb{R}^{3}$, the gimbal angles for two of the four CMGs can be represented by an index number along the X and Y axes of a topographic plot. This state index number refers to a

specific state combination of the two CMGs chosen for that axis. Assuming that adjacent state index numbers represent gimbal angle combinations that are physically next to each other, the resulting plot will give a semi-contiguous representation of the system, shown in Figure 9 and Figure 10. The remaining two CMGs in the array would be represented in state index two and have a similar plot to Figure 10.

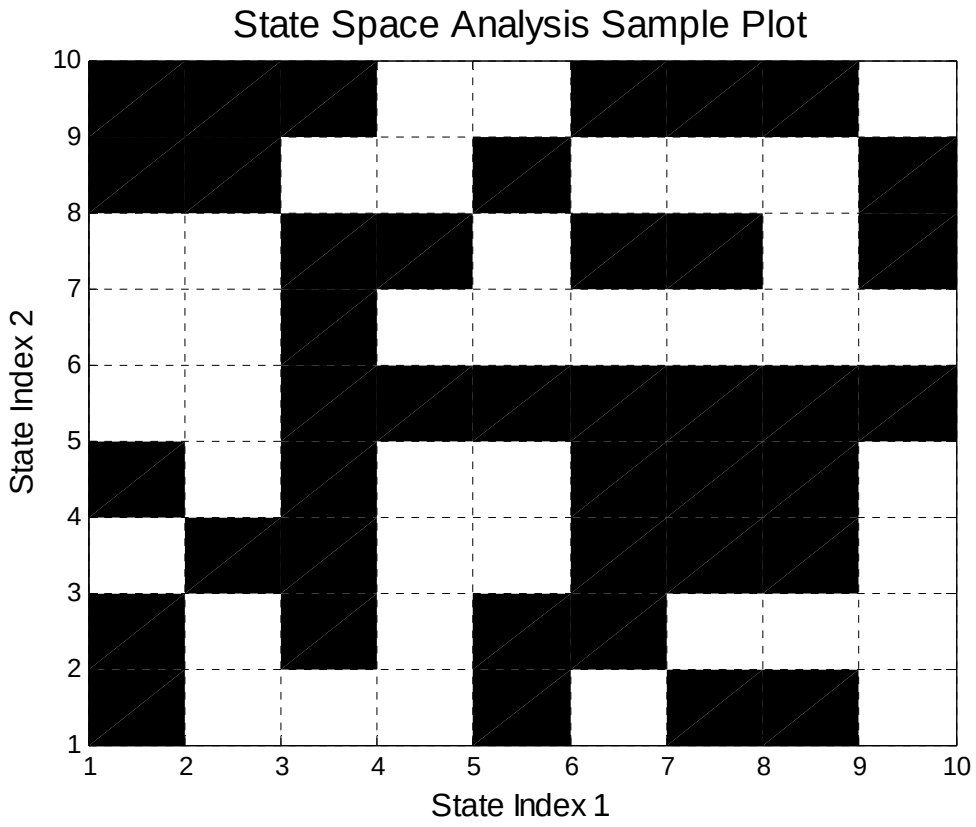

Figure 9. Four CMG semi-adjacent state space

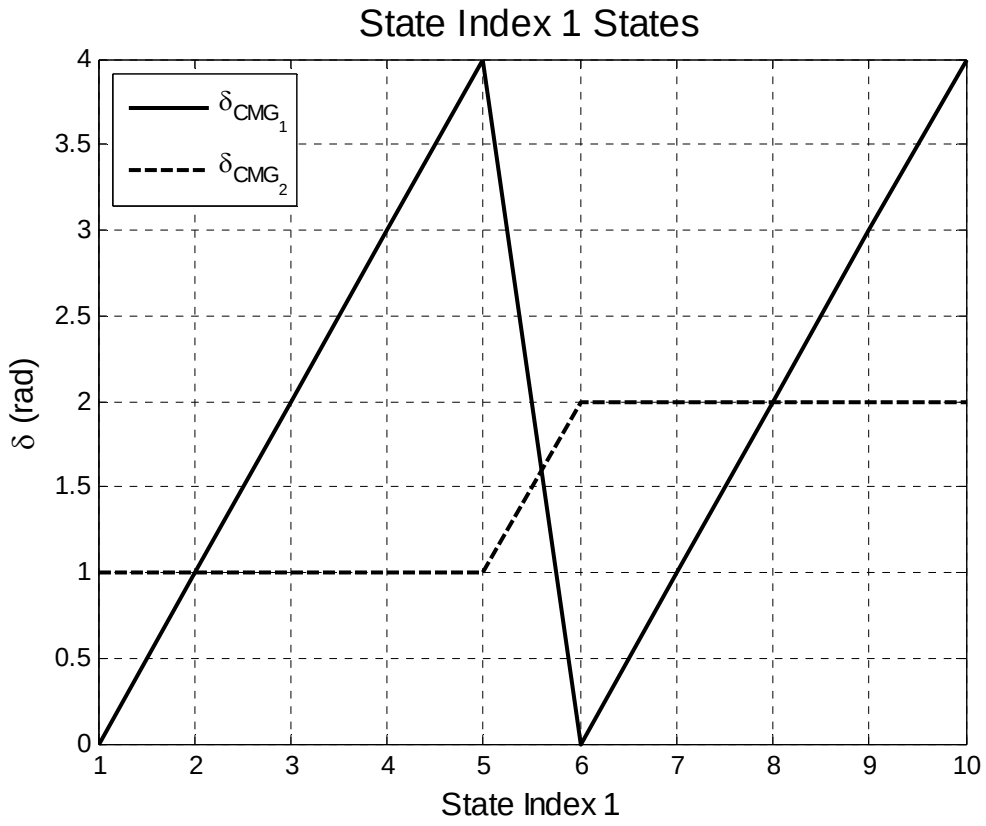

Figure 10. Reduced dimensional state space analysis state index array with two CMGs

This semi-contiguousness arises from the loss of one degree of freedom in each axis. This implies that although any trajectories drawn in this representation will result in valid physical trajectories for the CMG array, it does not represent the full set of possible trajectories. To achieve this, each CMG has to be able to change independently, requiring a plot of greater than three dimensions, which is very difficult to visualize.

Aside from indicating the problem with dimensional reduction and maintaining full contiguousness, Figure 9 and Figure 10 provide a guide for how to determine gimbal angle limits. Assume that the plot in Figure 9 shows locations

that result in singular (black) and non-singular (white) states in the CMG array state space. Gimbal angle limits for singularity free space can now be pulled from that plot by finding state index limits that bound only white areas. Specifically, if the gimbals were limited to those represented by the gimbal angles in states one and two for state index one and five through eight for state index two, the resulting momentum space for the array would be singularity free. By Figure 10, the first CMG in the array, as defined by the user, must operate between zero and one radians while the second CMG must remain at one radian. An additional plot for state index two would be required to determine the gimbal angle limits for the rest of the CMGs.

D. SUMMARY

This chapter developed the equations necessary to determine the torque envelope for a RW array and showed that the geometry of the torque envelope will have the same shape as the momentum envelope.

For CMG arrays, the groundwork was laid to use a state space based analysis to examine the possibility of operating in singularity free momentum space. The concept of contiguousness was established to ensure that the results of the analysis would allow for the CMGs to reach every state in the defined non-singular region without having to violate the established boundaries. Subsequent chapters will look at how the limited momentum envelope compares to the theoretical maximum developed in the Chapter III, and test the feasibility of operating within this region.

THIS PAGE INTENTIONALLY LEFT BLANK

V. ANALYSIS OF REACTION FORCES

One important area that has received little attention in the literature is examining the reaction forces at the attachment points of the RWs and CMGs throughout a spacecraft maneuver. Current pedagogy on this topic focuses on the transfer of momentum between the spacecraft and the MED. The vehicle of this transfer, reaction forces and moments on the attachment points between the MED and the spacecraft, is rarely discussed. There are several possible causes for this. One reason may be that experimental data determined that standard attachment design was robust enough. Or that other loading such as vibrational loading greatly exceeded the expected magnitude of maneuver loading. It is even possible that the analysis sits in a particularly bad convergence between two fields such that neither dynamicists nor structural engineers have a desire to study the problem. Regardless of the reason, it is important to understand what is happening at the attachment points in order to appropriately size the motors, bearings and gimbals so that total mass can be minimized while maintaining an appropriate safety factor to protect against failure.

For the analysis presented in this chapter, all motion between adjacent surfaces is assumed to be frictionless and all forces on bearing surfaces are assumed to be acting as a single resultant force at the centroid. The effect of gravity is neglected. All final reactions are defined as acting on the component being analyzed.

A. INERTIAL MOTION

Solving for the reaction forces for the MEDs begins with determining the motion of each component part within inertial space. To calculate the motion specific to these components, data such as satellite orientation, gimbal angles, etc… must be known. The rates and accelerations associated with these motions can be estimated using numerical differentiation techniques, but the fidelity of the analysis may suffer. The most accurate results require complete knowledge of the system during the time period analyzed.

The inertial motion for both the RW and the gimbal frame of the CMGs is the same. To begin, the inertial position vector for the RW center of mass must be expressed as in Equation (60).

$$ {}^{N}r_{rw} = {}^{N}P_{S/C} + {}^{b}r_{rw} \tag{60} $$

As noted in the introduction, there are two equivalent methods to proceed from here. The first method, shown in Equations (61) and (62), uses the transport theorem and differentiates twice, then uses the appropriate DCMs to convert all terms to the correct frames.

$$ \begin{aligned} {}^{N}v_{rw} &= {}^{N}\dot{P}_{S/C} + \left(\cancel{\omega}^{N/N} \times {}^{N}P_{S/C}\right) + {}^{b}\dot{r}_{rw} + \omega^{b/N} \times {}^{b}r_{rw} \\ {}^{N}a_{rw} &= {}^{N}\ddot{P}_{S/C} + {}^{b}\ddot{r}_{rw} + \omega^{b/N} \times {}^{b}\dot{r}_{RW} + \dot{\omega}^{b/N} \times {}^{b}r_{rw} + \omega^{b/N} \times {}^{b}\dot{r}_{rw} + \omega^{b/N} \times \omega^{b/N} \times {}^{b}r_{rw} \\ {}^{N}a_{rw} &= {}^{N}\ddot{P}_{S/C} + {}^{b}\ddot{r}_{rw} + 2\left(\omega^{b/N} \times {}^{b}\dot{r}_{rw}\right) + \dot{\omega}^{b/N} \times {}^{b}r_{rw} + \omega^{b/N} \times \omega^{b/N} \times {}^{b}r_{rw} \end{aligned} \tag{61} $$

To maintain all vectors in a consistent basis, all body terms must be expressed in the inertial frame.

$$ {}^{N}a_{rw} = {}^{N}\ddot{P}_{S/C} + {}^{N}_{b}R\left[{}^{b}\ddot{r}_{rw} + 2\left(\omega^{b/N} \times {}^{b}\dot{r}_{rw}\right) + \alpha^{b/N} \times {}^{b}r_{rw} + \omega^{b/N} \times \omega^{b/N} \times {}^{b}r_{rw}\right] \tag{62} $$

Alternatively, Equation (60) can be expressed so that all quantities are expressed in the inertial frame and the differentiation operations performed (Equations (63) and (64)).

$$ {}^{N}r_{rw} = {}^{N}P_{S/C} + {}^{N}_{b}R\,{}^{b}r_{rw} \tag{63} $$

$$ \begin{aligned} {}^{N}v_{rw} &= {}^{N}\dot{P} + {}^{N}_{b}\dot{R}\,{}^{b}r_{rw} + {}^{N}_{b}R\,{}^{b}\dot{r}_{rw} \\ {}^{N}a_{rw} &= {}^{N}\ddot{P} + {}^{N}_{b}\ddot{R}\,{}^{b}r_{rw} + {}^{N}_{b}\dot{R}\,{}^{b}\dot{r}_{rw} + {}^{N}_{b}R\,{}^{b}\ddot{r}_{rw} + {}^{N}_{b}\dot{R}\,{}^{b}\dot{r}_{rw} \\ {}^{N}a_{rw} &= {}^{N}\ddot{P} + {}^{N}_{b}\ddot{R}\,{}^{b}r_{rw} + 2\left({}^{N}_{b}\dot{R}\,{}^{b}\dot{r}_{rw}\right) + {}^{N}_{b}R\,{}^{b}\ddot{r}_{rw} \end{aligned} \tag{64} $$

Then, using the identities in Equation (65), Equation (64) can be written in the same form as Equation (62) as shown in Equation (66).

$$ \begin{aligned} & a = \begin{bmatrix} a_1 \\ a_2 \\ a_3 \end{bmatrix} \Rightarrow [\underset{\sim}{a}] = \begin{bmatrix} 0 & -a_3 & a_2 \\ a_3 & 0 & -a_1 \\ -a_2 & a_1 & 0 \end{bmatrix} \\ & a \times b = [\underset{\sim}{a}]b \\ & {}^{y}_{x}\dot{R} = {}^{y}_{x}R\left[\underset{\sim}{\omega}^{x/y}\right] \\ & {}^{y}_{x}\ddot{R} = {}^{y}_{x}\dot{R}\left[\underset{\sim}{\omega}^{x/y}\right] + {}^{y}_{x}R\left[\dot{\underset{\sim}{\omega}}^{x/y}\right] = {}^{y}_{x}R\left[\underset{\sim}{\alpha}^{x/y}\right] + {}^{y}_{x}R\left[\underset{\sim}{\omega}^{x/y}\right]\left[\underset{\sim}{\omega}^{x/y}\right] \end{aligned} \tag{65} $$

$$ \begin{aligned} {}^{N}a_{rw} &= {}^{N}\ddot{P}_{S/C} + {}^{N}_{b}\ddot{R}\,{}^{b}r_{rw} + 2\left({}^{N}_{b}\dot{R}\,{}^{b}\dot{r}_{rw}\right) + {}^{N}_{b}R\,{}^{b}\ddot{r}_{rw} \\ {}^{N}a_{rw} &= {}^{N}\ddot{P}_{S/C} + \left[{}^{N}_{b}R\left[\underset{\sim}{\alpha}^{b/N}\right] + {}^{N}_{b}R\left[\underset{\sim}{\omega}^{b/N}\right]\left[\underset{\sim}{\omega}^{b/N}\right]\right]{}^{b}r_{rw} + 2\left({}^{N}_{b}R\left[\underset{\sim}{\omega}^{b/N}\right]{}^{b}\dot{r}_{rw}\right) + {}^{N}_{b}R\,{}^{b}\ddot{r}_{rw} \\ {}^{N}a_{rw} &= {}^{N}\ddot{P}_{S/C} + {}^{N}_{b}R\left[{}^{b}\ddot{r}_{rw} + 2\left(\omega^{b/N} \times {}^{b}\dot{r}_{rw}\right) + \alpha^{b/N} \times {}^{b}r_{rw} + \omega^{b/N} \times \omega^{b/N} \times {}^{b}r_{rw}\right] \end{aligned} \tag{66} $$

Equation (66) gives the same expression as Equation (62). The primary difference between the two approaches lies in the fact that the product-rule approach, the second approach, requires that the vector be resolved in the inertial frame prior to differentiation while the transport theorem approach does not. This can cause the product-rule approach to create a large amount of terms as additional

frames are added to the problem, making it fairly unwieldy to solve by hand. The primary benefits of the product-rule approach deal with the simplicity in creating an algorithm to do symbolic differentiation on a computer as well as explicitly maintaining all terms in a consistent reference frame. In this case, there are sufficiently few reference frames that both approaches are reasonable to work with.

If the RW center of mass is assumed to be fixed within the structure, a valid assumption for a rigid spacecraft, then some of the terms can be eliminated to give:

$$ {}^{N}a_{rw} = {}^{N}\ddot{P}_{S/C} + {}^{N}_{b}R\left[\left[\tilde{\alpha}^{b/N}\right] + \left[\tilde{\omega}^{b/N}\right]\left[\tilde{\omega}^{b/N}\right]\right]{}^{b}r_{rw} \tag{67} $$

As mentioned earlier, the CMG gimbal frame has the same equations of motion as the RW frame, rewritten as Equation (68):

$$ \begin{aligned} {}^{N}r_{g} &= {}^{N}P_{S/C} + {}^{N}_{b}R^{b}r_{g} \\ {}^{N}a_{g} &= {}^{N}\ddot{P}_{S/C} + {}^{N}_{b}R\left[\left[\tilde{\alpha}^{b/N}\right] + \left[\tilde{\omega}^{b/N}\right]\left[\tilde{\omega}^{b/N}\right]\right]{}^{b}r_{g} \end{aligned} . \tag{68} $$

For a CMG, the presence of an additional rotor frame adds another term to the initial position vector and requires an additional DCM to go from the gimbal frame to body frame. Using a similar analysis as above and applying the rigid body assumptions yields the rotor equations of motion (Equation (69)).

$$
\begin{aligned}
{}^{N}r_r &= {}^{N}P_{S/C} + {}^{N}_{b}R\,{}^{b}r_g + {}^{N}_{b}R\,{}^{b}_{g}R\,{}^{g}r_r \\
{}^{N}a_r &= {}^{N}a_g + {}^{N}_{b}R\left(\left[\underset{\sim}{\alpha}^{b/N}\right]+\left[\underset{\sim}{\omega}^{b/N}\right]\left[\underset{\sim}{\omega}^{b/N}\right]\right){}^{b}_{g}R\,{}^{g}r_r \\
&\quad +2\,{}^{N}_{b}R\left[\underset{\sim}{\omega}^{b/N}\right]{}^{b}_{g}R\left[\underset{\sim}{\omega}^{g/b}\right]{}^{g}r_r + 2\,{}^{N}_{b}R\left[\underset{\sim}{\omega}^{b/N}\right]{}^{b}_{g}R\,{}^{g}\dot{r}_r \\
&\quad +2\,{}^{N}_{b}R\,{}^{b}_{g}R\left[\underset{\sim}{\omega}^{g/b}\right]{}^{g}\dot{r}_r + {}^{N}_{b}R\,{}^{b}_{g}R\left(\left[\underset{\sim}{\alpha}^{g/b}\right]+\left[\underset{\sim}{\omega}^{g/b}\right]\left[\underset{\sim}{\omega}^{g/b}\right]\right){}^{g}r_r \\
&\quad +{}^{N}_{b}R\,{}^{b}_{g}R\,{}^{g}\ddot{r}_r \\
{}^{N}a_r &= {}^{N}a_g + {}^{N}_{b}R\left(\left[\underset{\sim}{\alpha}^{b/N}\right]+\left[\underset{\sim}{\omega}^{b/N}\right]\left[\underset{\sim}{\omega}^{b/N}\right]\right){}^{b}_{g}R\,{}^{g}r_r \\
&\quad +2\,{}^{N}_{b}R\left[\underset{\sim}{\omega}^{b/N}\right]{}^{b}_{g}R\left[\underset{\sim}{\omega}^{g/b}\right]{}^{g}r_r + {}^{N}_{b}R\,{}^{b}_{g}R\left(\left[\underset{\sim}{\alpha}^{g/b}\right]+\left[\underset{\sim}{\omega}^{g/b}\right]\left[\underset{\sim}{\omega}^{g/b}\right]\right){}^{g}r_r
\end{aligned}
\tag{69}
$$

When using the transport theorem to develop Equation (69), an additional step is required to determine the angular rates, since it is very unlikely that the inertial angular rate and acceleration of the gimbal frame is measured. This quantity can, however, be determined from the spacecraft body rates and the gimbal rate (shown in Equation (70)), both of which are typically measured quantities.

$$
\begin{aligned}
\omega^{g/N} &= \omega^{b/N} + \omega^{g/b} \\
\dot{\omega}^{g/N} &= \dot{\omega}^{b/N} + \dot{\omega}^{g/b} + \omega^{g/N} \times \omega^{g/b} \\
&= \dot{\omega}^{b/N} + \dot{\omega}^{g/b} + \left(\omega^{b/N} + \omega^{g/b}\right) \times \omega^{g/b} \\
&= \dot{\omega}^{b/N} + \dot{\omega}^{g/b} + \omega^{b/N} \times \omega^{g/b}
\end{aligned}
\tag{70}
$$

B. REACTION WHEELS

1. Case One – Cantilever

For RWs, two cases have been considered, as represented by Figure 11 and Figure 12. For case one (which represents a cantilever arrangement), there is exactly one reaction force and one reaction moment, leading to Equations (71) and (72).

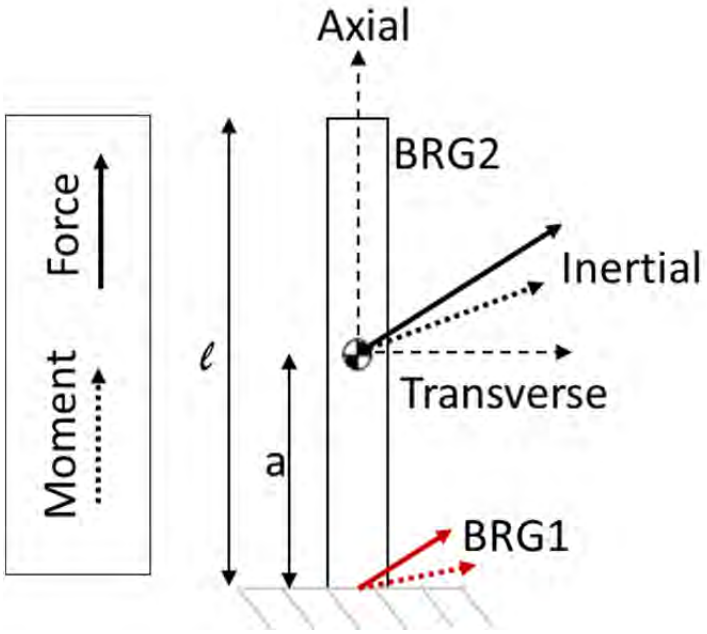

Figure 11. Schematic of RW cantilever arrangement

$$\begin{aligned} \sum F &= ma \\ \sum\nolimits_A M &= \dot{h} \end{aligned} \tag{71}$$

$$\begin{aligned} F_{R_{BRG1}} &= m_{rw} a_{rw} \\ M_{R_{BRG1}} + r \times \left(F_{Inertial} \right) &= I_{rw} \dot{\omega}^{rw/N} + \omega^{rw/N} \times I_{rw} \omega^{rw/N} \\ F_{Inertial} &= m_{rw} a_{rw} \\ M_{Inertial} &= \left(I_{rw} \dot{\omega}^{rw/N} + \omega^{rw/N} \times I_{rw} \omega^{rw/N} \right) \end{aligned} \tag{72}$$

The RW motor, assumed to be mounted with bearing one, is not explicitly included on the left hand side of Equation (72). It is, however, implicitly included in the $M_{Inertial}$ term as the effect of that torque on the system: $\dot{\omega}_{RW_Z}$. If it is desired to use actual motor torque output instead of measured or calculated wheel acceleration, the additional torque should be included. The wheel

acceleration due to the motor torque, however, should then *not* be included in the equations of motion. Doing so will cause the terms to cancel out and remove the motor torque from the overall reactions.

The right hand side of the force balance equation is straightforward as the acceleration term was developed in Equation (67) and all quantities in that equation are known. The right hand side of the moment balance equation requires some additional analysis to be put into a useful form.

Since the rotation of the RW frame in inertial space is not directly measured, it must be calculated from known quantities as shown by Equation (73).

$$\omega^{rw/N} = {}^{rw}_{b}R\omega^{b/N} + \omega^{rw/b} \tag{73}$$

As noted in Section A, to utilize the product-rule approach of differentiation it is important to initially express the vector in the inertial frame. After differentiation, the frame may be changed as desired.

The angular momentum of the RW can now be calculated and differentiated (Equations (74) and (75)). The moment of inertia for the RW is assumed to be constant about the spin axis.

$$\begin{aligned}
{}^{N}h_{rw} &= {}^{N}_{b}R\,{}^{b}_{rw}R\,I_{rw}\,{}^{rw}_{b}R\omega^{b/N} + {}^{N}_{b}R\,{}^{b}_{rw}R\,I_{rw}\omega^{rw/b} \\
{}^{N}\dot{h}_{rw} &= {}^{N}_{b}\dot{R}\,{}^{b}_{rw}R\,I_{rw}\,{}^{rw}_{b}R\,\omega^{b/N} + {}^{N}_{b}R\,{}^{b}_{rw}\dot{R}\,I_{rw}\,{}^{rw}_{b}R\,\omega^{b/N} \\
&\quad + {}^{N}_{b}R\,{}^{b}_{rw}R\,I_{rw}\,{}^{rw}_{b}\dot{R}\,\omega^{b/N} + {}^{N}_{b}R\,{}^{b}_{rw}R\,I_{rw}\,{}^{rw}_{b}R\,\dot{\omega}^{b/N} \\
&\quad + {}^{N}_{b}\dot{R}\,{}^{b}_{rw}R\,I_{rw}\,\omega^{rw/b} + {}^{N}_{b}R\,{}^{b}_{rw}\dot{R}\,I_{rw}\,\omega^{rw/b} + {}^{N}_{b}R\,{}^{b}_{rw}R\,I_{rw}\,\dot{\omega}^{rw/b}
\end{aligned} \tag{74}$$

$$
\begin{aligned}
{}^{N}\dot{h}_{RW} &= {}^{N}_{B}R\left[\tilde{\omega}^{B/N}\right]{}^{B}_{RW}RI_{RW}{}^{RW}_{B}R\omega^{B/N} + {}^{N}_{B}R\,{}^{B}_{RW}R\left[\tilde{\omega}^{RW/B}\right]I_{RW}{}^{RW}_{B}R\omega^{B/N} \\
&+ {}^{N}_{B}R\,{}^{B}_{RW}RI_{RW}{}^{RW}_{B}R\left[\tilde{\omega}^{B/RW}\right]\omega^{B/N} + {}^{N}_{B}R\,{}^{B}_{RW}RI_{RW}{}^{RW}_{B}R\dot{\omega}^{B/N} \\
&+ {}^{N}_{B}R\left[\tilde{\omega}^{B/N}\right]{}^{B}_{RW}RI_{RW}\omega^{RW/B} + {}^{N}_{B}R\,{}^{B}_{RW}R\left[\tilde{\omega}^{RW/B}\right]I_{RW}\omega^{RW/B} + {}^{N}_{B}R\,{}^{B}_{RW}RI_{RW}\dot{\omega}^{RW/B}
\end{aligned}
\tag{75}
$$

The third term of Equation (75) includes the matrix $\left[\tilde{\omega}^{b/rw}\right]$. Physically, this matrix is the rotation of the body with respect to the RW frame, given in body frame coordinates. Since it is a skew symmetric matrix, there are two equivalent approaches: change the basis of the rotation vector prior to converting it to a skew symmetric matrix, or use a similarity transformation to transform it. Since the data will be given in the form of a rotation rate in the RW frame, the first method should be used. Thus, Equation (76) now contains terms which designate given or easily calculated data.

$$
\begin{aligned}
{}^{rw}\omega^{b/rw} &= -{}^{rw}\omega^{rw/b} \\
{}^{b}\omega^{b/rw} &= -{}^{b}_{rw}R\,\omega^{rw/b}
\end{aligned}
\tag{76}
$$

Finally, converting into the RW frame yields Equation (77).

$$
\begin{aligned}
{}^{rw}\dot{h}_{rw} &= {}^{rw}_{b}R\,{}^{b}_{N}R\,{}^{N}\dot{h}_{rw} \\
{}^{rw}\dot{h}_{rw} &= {}^{rw}_{b}R\left[\tilde{\omega}^{b/N}\right]{}^{b}_{rw}R\,I_{rw}{}^{rw}_{b}R\,\omega^{b/N} + \left[\tilde{\omega}^{rw/b}\right]I_{rw}{}^{rw}_{b}R\,\omega^{b/N} \\
&+ I_{rw}{}^{rw}_{b}R\left[\tilde{\omega}^{b/rw}\right]\omega^{b/N} + I_{rw}{}^{rw}_{b}R\,\dot{\omega}^{b/N} + {}^{rw}_{b}R\left[\tilde{\omega}^{b/N}\right]{}^{b}_{rw}R\,I_{rw}\,\omega^{rw/b} \\
&+ \left[\tilde{\omega}^{rw/b}\right]I_{rw}\,\omega^{rw/b} + I_{rw}\,\dot{\omega}^{rw/b}
\end{aligned}
\tag{77}
$$

The motor torque is equal to the third component of Equation (77) [1, pp. 179-185]. Under ideal conditions, the motor would resist any change in wheel speed with respect to the body due to the motion of the spacecraft around the RW spin axis unless a torque input is desired.

The inclusion of an additional motor torque term in the left hand side of the torque balance equation would (assuming ideal data) negate the spin-axis torque and corrupt the output.

2. Case Two – Fixed-Fixed

The solution for case two (given in Figure 12) requires some additional assumptions due to the overdetermined nature of the fixed-fixed system. These assumptions, along with solutions based on continuity and compatibility conditions allow for determining the bearing reactions.

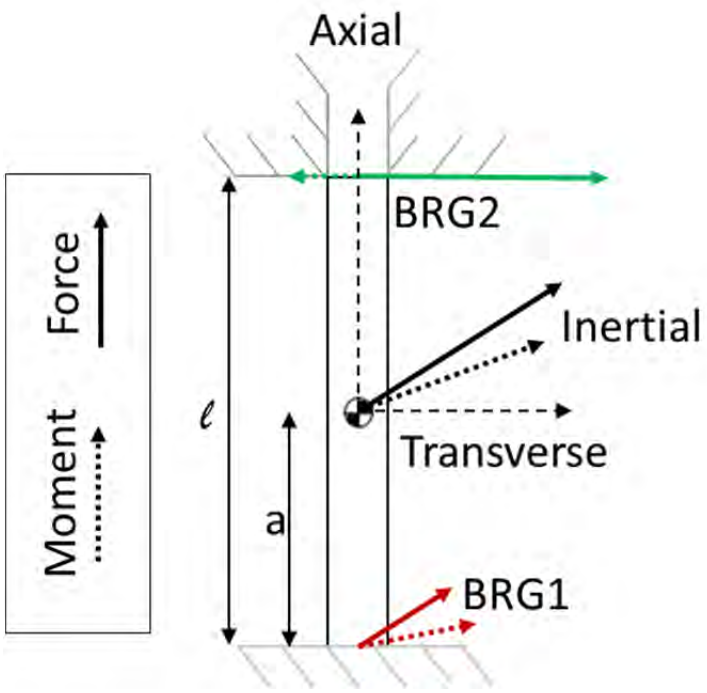

Figure 12. Schematic of RW fixed-fixed arrangement

For forces along the axial direction, it is assumed that the non-motor bearing, bearing two, is allowed to translate and thus cannot support a load. This places all

axial loading on bearing one. Similarly, for torques in the axial direction, bearing two is assumed frictionless so all axial reaction moments are resisted by the motor at bearing one.

For the transverse cases, reaction forces and moments for each axis can be calculated via superposition using the solved cases in a reference book such as Table 8.1 of *Roark's Formulas for Stress and Strain* [13, pp. 208-223].

To place the problem in the format of the standard tables, d'Alembert's principle as applied to rigid bodies is used to rewrite Equations (71) and (72) in the quasi-static form of Equations (78) and (79) [3, p. 142]. Additionally, all forces and moments must be resolved into the RW frame prior to the analysis.

$$\begin{aligned} \sum F - F_{Inertial} &= 0 \\ \sum\nolimits_A M - M_{Inertial} &= 0 \end{aligned} \tag{78}$$

$$\begin{aligned} F_{R_{BRG1}} + F_{R_{BRG2}} - F_{Inertial} &= 0 \\ M_{R_{BRG1}} + M_{R_{BRG2}} - M_{Inertial} &= 0 \\ F_{R_{BRG1}} &= F_{F_{Inertial_{BRG1}}} + F_{M_{Inertial_{BRG1}}} \\ M_{R_{BRG2}} &= M_{M_{Inertial_{BRG2}}} + M_{F_{Inertial_{BRG2}}} \\ M_{R_{BRG1}} &= M_{M_{Inertial_{BRG1}}} + M_{F_{Inertial_{BRG1}}} \\ F_{R_{BRG2}} &= F_{F_{Inertial_{BRG2}}} + F_{M_{Inertial_{BRG2}}} \end{aligned} \tag{79}$$

The final reactions are given in Equations (80)-(85).

$$F_{R_{BRGn}} = \begin{bmatrix} F_{R_{BRGnx}} \\ F_{R_{BRGny}} \\ F_{R_{BRGnz}} \end{bmatrix}; \qquad M_{R_{BRGn}} = \begin{bmatrix} M_{R_{BRGnx}} \\ M_{R_{BRGny}} \\ M_{R_{BRGnz}} \end{bmatrix} \tag{80}$$

$$F_{R_{BRG1z}} = F_{Inertial_z}; \qquad M_{R_{BRG1z}} = M_{Inertial_z}$$
$$F_{R_{BRG2z}} = 0; \qquad M_{R_{BRG2z}} = 0 \tag{81}$$

$$F_{F_{Inertial_{BRG1_{x.y}}}} = \frac{F_{Inertial_{x,y}}}{l^3}(l-a)^2(l+2a)$$
$$F_{F_{Inertial_{BRG2_{x.y}}}} = \frac{F_{Inertial_{x,y}}}{l^3}a^2(3l-2a) \tag{82}$$

$$M_{F_{Inertial_{BRG1_{x,y}}}} = sign\left(r_{BRG1\to COM} \times F_{Inertial}\right)_{x,y} \frac{F_{Inertial\,y,x}}{l^2} a(l-a)^2$$
$$M_{F_{Inertial_{BRG1_{x,y}}}} = sign(r_{BRG2\to COM} \times F_{Inertial})_{x,y} \frac{F_{Inertial\,y,x}}{l^2} a^2(l-a) \tag{83}$$

$$F_{M_{Inertial_{BRG1_x}}} = -\frac{M_{Inertial_y}}{l^3} 6a(l-a)$$
$$F_{M_{Inertial_{BRG1_y}}} = \frac{M_{Inertial_x}}{l^3} 6a(l-a) \tag{84}$$
$$F_{M_{Inertial_{BRG2_{x,y}}}} = -F_{M_{Inertial_{BRG1_{x,y}}}}$$

$$M_{M_{Inertial_{BRG1_{x,y}}}} = \frac{M_{Inertial_{x,y}}}{l^2}\left(l^2 - 4al + 3a^2\right)$$
$$M_{M_{Inertial_{BRG2_{x,y}}}} = \frac{M_{Inertial_{x,y}}}{l^2}\left(3a^2 - 2al\right) \tag{85}$$

C. CMGS

In order to simplify the analysis of a real CMG, such as the one shown in Figure 13, a model was constructed with a rotor shaft mounted directly onto a gimbal shaft (Figure 14). The only other assumption made in this simplification involved the end conditions of both shafts. All other characteristics such as length, center of mass location, mass and moment of inertia were left as variable. Neither the actual rotor nor gimbal frames need be in their respective principal frames. Instead, those body frames

are defined with respect to the geometry of the system. If the body frame and principal frame are not aligned for the rotor, the system is assumed to be static.

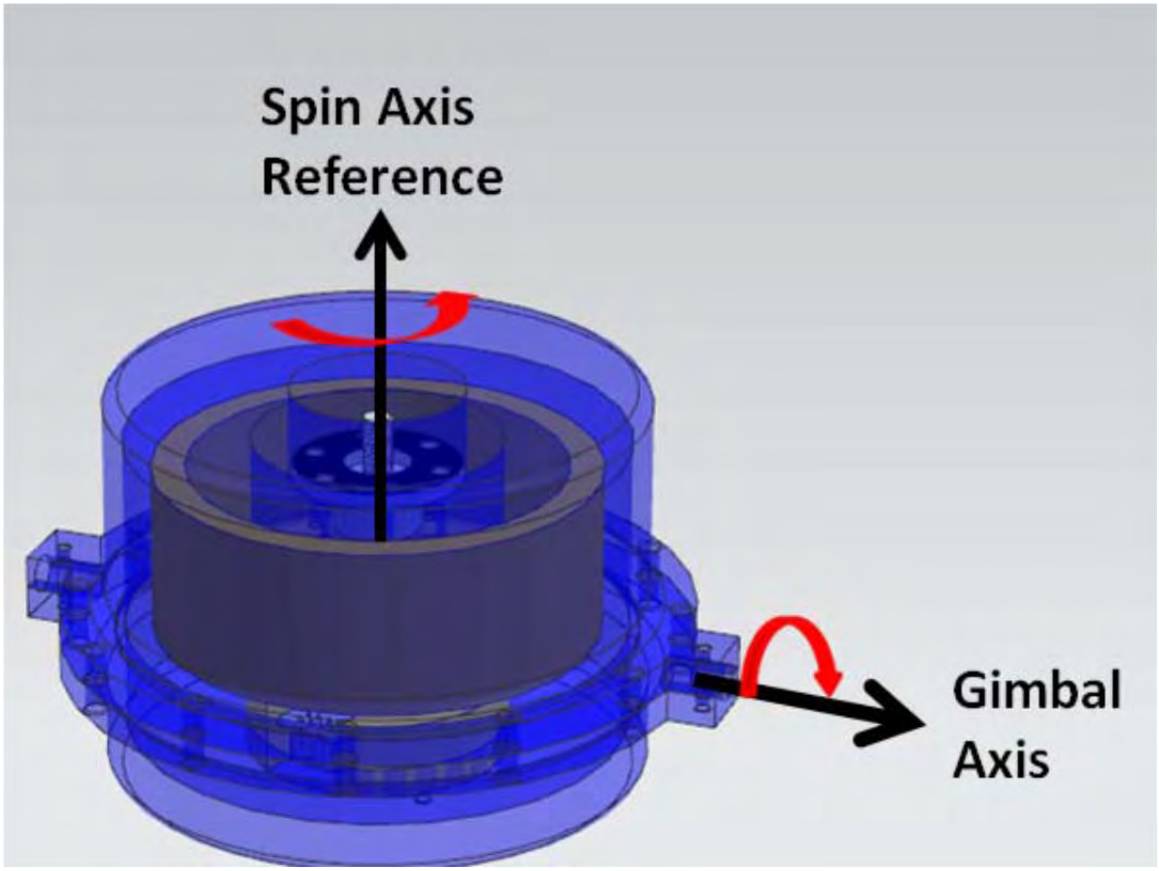

Figure 13. Typical CMG Construction, from [14]

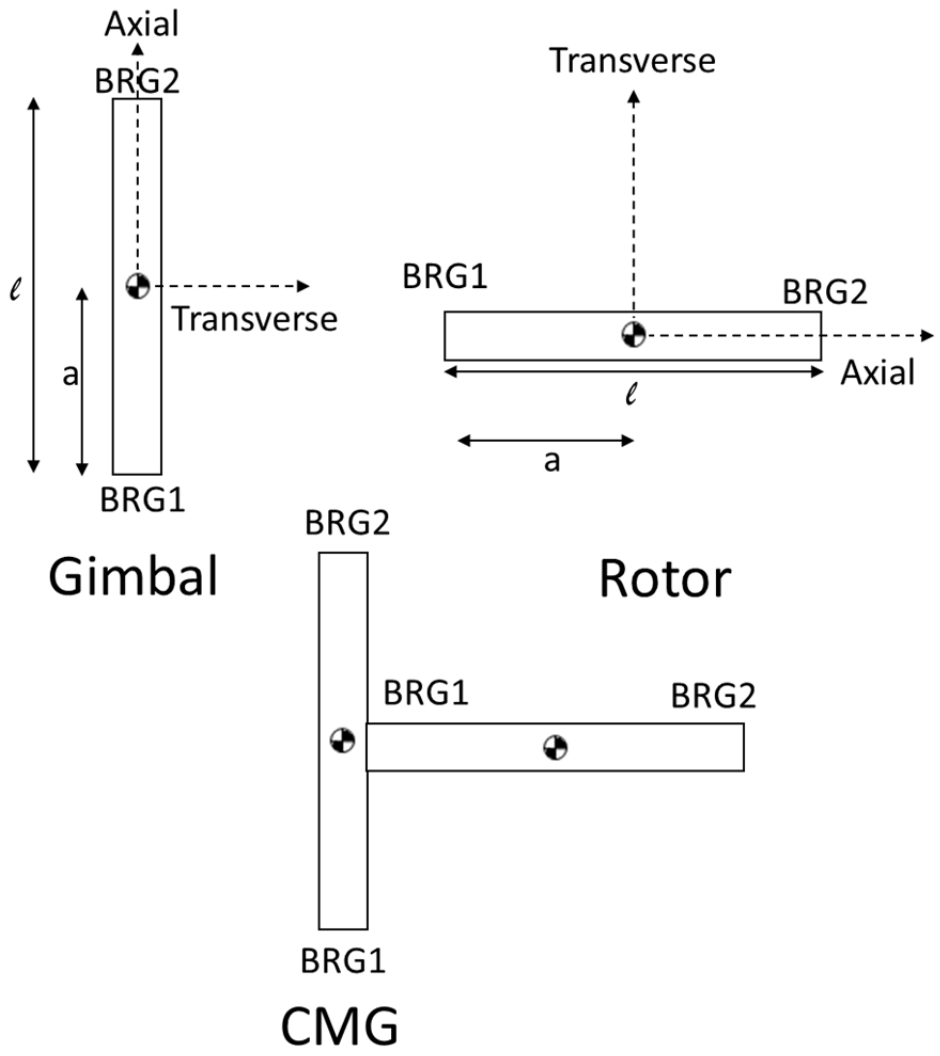

Figure 14. Simplified CMG model

The CMG analysis is broken up into two parts: analysis of the rotor and analysis of the gimbal. The analysis for the rotor matches the previous RW analysis very closely. The gimbal, however, adds additional complexity due to the mounting of the rotor on the gimbal shaft in this model.

Both the rotor and gimbal are independently analyzed as a cantilever and as a fixed-fixed system, giving four possible configurations for the CMG as a whole.

1. Rotor

a. Cantilever

Equations (71) and (72) both apply to the cantilever CMG rotor (shown in Figure 15), with the inertial acceleration already determined by Equation (69). Equation (86) gives those rewritten equations.

$$\begin{aligned} F_R &= m_r a_r \\ M_{R_A} + r \times \left(F_{Inertial} \right) &= I_R \dot{\omega}^{r/N} + \omega^{r/N} \times I_r \, \omega^{r/N} \\ F_{Inertial} &= m_r a_r \\ M_{Inertial} &= \left(I_r \, \dot{\omega}^{r/N} + \omega^{r/N} \times I_r \, \omega^{r/N} \right) \end{aligned} \tag{86}$$

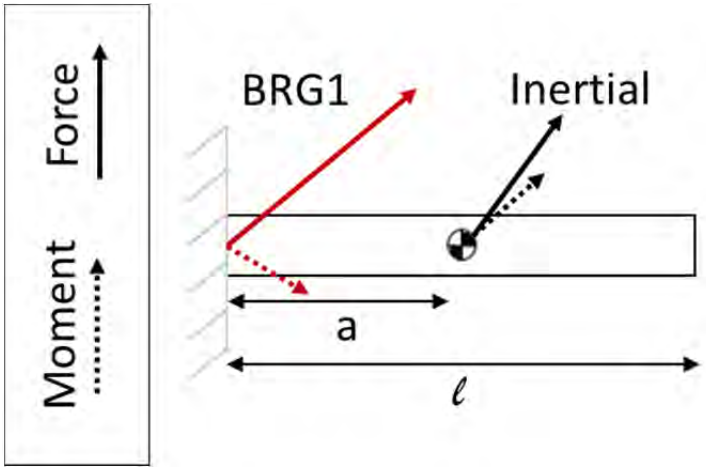

Figure 15. Schematic of CMG rotor cantilever arrangement

All that remains, then, is to derive the derivative of the inertial angular momentum vector to create the inertial moment. The angular momentum vector

itself has already been discussed and is given in Equation (87).

$$h_r = I_r \omega^{r/N} \tag{87}$$

Expanding the angular rate term and writing the vector in the inertial frame yields Equation (88).

$$\begin{aligned} {}^{N}h_r = {}^{N}_{b}R\,{}^{b}_{g}R\,{}^{g}_{r}R\,I_r\,{}^{r}_{g}R\,{}^{g}_{b}R\,\omega^{b/N} + {}^{N}_{b}R\,{}^{b}_{g}R\,{}^{g}_{r}R\,I_r\,{}^{r}_{g}R\,\omega^{g/b} \\ + {}^{N}_{b}R\,{}^{b}_{g}R\,{}^{g}_{r}R\,I_r\,\omega^{r/g} \end{aligned} \tag{88}$$

Further simplifications occur on the realization that ${}^{g}_{r}R = {}^{r}_{g}R = I_{3x3}$ and result in Equation (89).

$${}^{N}h_r = {}^{N}_{b}R\,{}^{b}_{g}R\,I_r\,{}^{g}_{b}R\,\omega^{b/N} + {}^{N}_{b}R\,{}^{b}_{g}R\,I_r\,\omega^{g/b} + {}^{N}_{b}R\,{}^{b}_{g}R\,I_r\,\omega^{r/g} \tag{89}$$

Differentiating as above and converting back to the rotor frame gives Equation (90).

$$\begin{aligned} {}^{r}\dot{h}_r = {}^{g}_{b}R\left[\tilde{\omega}^{b/N}\right]{}^{b}_{g}R\,I_r\left({}^{g}_{b}R\,\omega^{b/N} + \omega^{g/b} + \omega^{r/g}\right) \\ + \left[\tilde{\omega}^{g/b}\right] I_r\left({}^{g}_{b}R\,\omega^{b/N} + \omega^{g/b} + \omega^{r/g}\right) \\ + I_r\,{}^{g}_{b}R\left(\left[\tilde{\omega}^{b/g}\right]\omega^{b/N} + \dot{\omega}^{b/N}\right) \\ + I_r\left(\dot{\omega}^{g/b} + \dot{\omega}^{r/g}\right) \\ {}^{b}\omega^{b/g} = -\,{}^{b}_{g}R\,\omega^{g/b} \end{aligned} \tag{90}$$

b. Fixed-Fixed

The same force and moment balance equations used by the fixed-fixed RW (Equations (80)-(85)) also apply to the rotor in Figure 16. , however the transverse directions are now the y-z plane and the rotation axis is now the x-axis, so only a slight modification of the subscripts is required, which are shown in Equations (91)-(95).

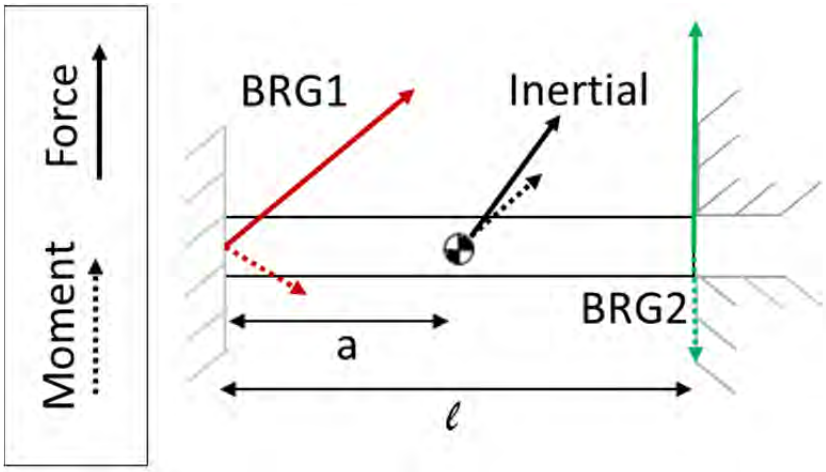

Figure 16. Schematic of CMG rotor fixed-fixed arrangement

$$F_{R_{BRG1x}} = F_{Inertial_x}; \qquad M_{R_{BRG1x}} = M_{Inertial_x}$$
$$F_{R_{BRG2x}} = 0; \qquad M_{R_{BRG2x}} = 0 \tag{91}$$

$$F_{F_{Inertial_{BRG1_{y,z}}}} = \frac{F_{Inertial_{y,z}}}{l^3}(l-a)^2(l+2a)$$
$$F_{F_{Inertial_{BRG2_{y,z}}}} = \frac{F_{Inertial_{y,z}}}{l^3}a^2(3l-2a) \tag{92}$$

$$M_{F_{Inertial_{BRG1_{y,z}}}} = sign\left(r_{BRG1\to COM} \times F_{Inertial}\right)_{y,z} \frac{F_{Inertial\,z,y}}{l^2} a(l-a)^2$$
$$M_{F_{Inertial_{BRG1_{y,z}}}} = sign(r_{BRG2\to COM} \times F_{Inertial})_{y,z} \frac{F_{Inertial\,z,y}}{l^2} a^2(l-a) \tag{93}$$

$$F_{M_{Inertial_{BRG1_y}}} = -\frac{M_{Inertial_z}}{l^3} 6a(l-a)$$
$$F_{M_{Inertial_{BRG1_z}}} = \frac{M_{Inertial_y}}{l^3} 6a(l-a) \tag{94}$$
$$F_{M_{Inertial_{BRG2_{y,z}}}} = -F_{M_{Inertial_{BRG1_{y,z}}}}$$

$$M_{M_{Inertial_{BRG1_{y,z}}}} = \frac{M_{Inertial_{y,z}}}{l^2}\left(l^2 - 4al + 3a^2\right)$$
$$M_{M_{Inertial_{BRG2_{y,z}}}} = \frac{M_{Inertial_{y,z}}}{l^2}\left(3a^2 - 2al\right) \tag{95}$$

2. Gimbal

a. Cantilever

For the gimbal, Figure 17, an additional force and moment must be considered: the reaction of the rotor on the gimbal. As these quantities are known from the rotor calculations, they simply add additional terms when solving for the cantilever reactions, given in Equation (95).

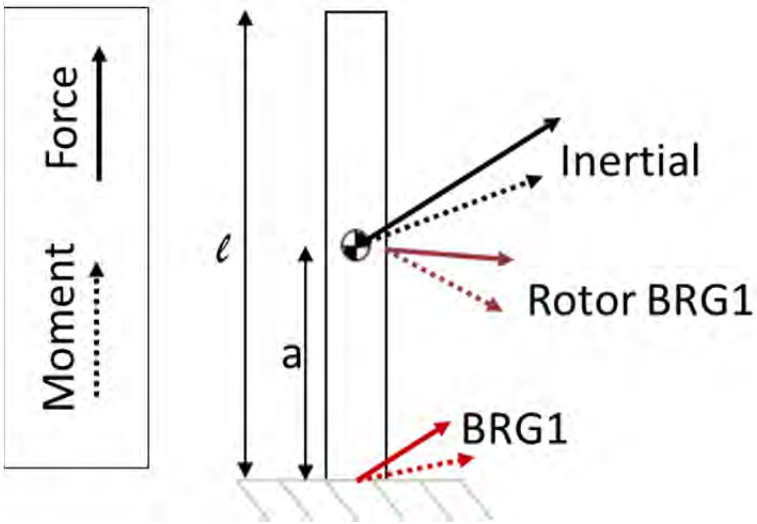

Figure 17. Schematic of CMG gimbal cantilever arrangement

$$
\begin{aligned}
&F_G + \left(-F_{Rotor_{G1}}\right) = m_G a_G \\
&M_{G_A} + \left(-M_{Rotor_{G1}}\right) + \left(r_{COMtoRotor} \times \left(-F_{Rotor_{G1}}\right)\right) + a \times \left(F_{Inertial}\right) = I_G \dot{\omega}^{G/N} + \omega^{G/N} \times I_G \omega^{G/N} \\
&F_{Inertial} = m_G a_G \\
&M_{Inertial} = \left(I_G \dot{\omega}^{G/N} + \omega^{G/N} \times I_G \omega^{G/N}\right)
\end{aligned}
\tag{95}
$$

b. Fixed-Fixed

To compute the gimbal reactions for the fixed-fixed case (Figure 18), the rotor force and moment must be shifted to the gimbal's center of mass, Equation (96), in

order to satisfy the condition that only a single force and moment are applied to the beam.

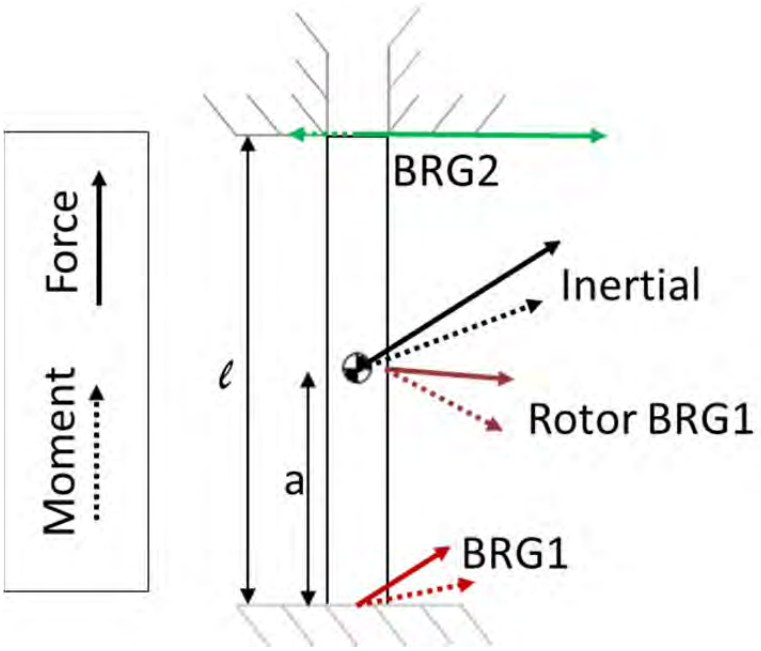

Figure 18. CMG Gimbal Fixed-Fixed Case

$$F^*_{Inertial} = F_{Inertial} + \left(-F_{Rotor_{Gimbal1}}\right)$$
$$M^*_{Inertial} = M_{Inertial} - \left(-M_{Rotor_{Gimbal1}}\right) - r \times F_{Inertial} - r_{COMtoRotor} \times \left(-F_{Rotor_{Gimbal1}}\right) \quad (96)$$

Using the idea of the combined force and moment, the final solutions are nearly identical to those presented in the fixed-fixed RW case and are given in Equations (97)-(101).

$$F_{R_{BRG1z}} = F^*_{Inertial_z}; \qquad M_{R_{BRG1z}} = M^*_{Inertial_z}$$
$$F_{R_{BRG2z}} = 0; \qquad M_{R_{BRG2z}} = 0 \quad (97)$$

$$F_{F_{Inertial_{BRG1_{x,y}}}} = \frac{F^*_{Inertial_{x,y}}}{l^3}(l-a)^2(l+2a)$$
$$F_{F_{Inertial_{BRG2_{x,y}}}} = \frac{F^*_{Inertial_{x,y}}}{l^3}a^2(3l-2a) \quad (98)$$

$$M_{F_{Inertial_{BRG1_{x,y}}}} = sign\left(r_{BRG1\rightarrow COM} \times F^{*}_{Inertial}\right)_{x,y} \frac{F^{*}_{Inertial\,y,x}}{l^2} a\left(l-a\right)^2$$
$$M_{F_{Inertial_{BRG1_{x,y}}}} = sign(r_{BRG2\rightarrow COM} \times F^{*}_{Inertial})_{x,y} \frac{F^{*}_{Inertial\,y,x}}{l^2} a^2\left(l-a\right) \quad (99)$$

$$F_{M_{Inertial_{BRG1_x}}} = -\frac{M^{*}_{Inertial_y}}{l^3} 6a\left(l-a\right)$$
$$F_{M_{Inertial_{BRG1_y}}} = \frac{M^{*}_{Inertial_x}}{l^3} 6a\left(l-a\right) \quad (100)$$
$$F_{M_{Inertial_{BRG2_{x,y}}}} = -F_{M_{Inertial_{BRG1_{x,y}}}}$$

$$M_{M_{Inertial_{BRG1_{x,y}}}} = \frac{M^{*}_{Inertial_{x,y}}}{l^2}\left(l^2-4al+3a^2\right)$$
$$M_{M_{Inertial_{BRG2_{x,y}}}} = \frac{M^{*}_{Inertial_{x,y}}}{l^2}\left(3a^2-2al\right) \quad (101)$$

D. SUMMARY

This chapter developed the equations of motion and applied forces and moments necessary to analyze the reaction forces of MEDs of various endpoint configurations over the course of a spacecraft maneuver. The derivation of these equations focused on requiring only the telemetry, geometry and operating characteristics that would be readily available from either an actual satellite or simulation.

The validation of the developed equations will occur in Chapter VI, Section C. This validation will show that the developed equations behave properly under various assumed condition. Following validation, simulated spacecraft maneuvers will be analyzed, with the focus on showing the impact that different control laws can have on the reaction forces during similar maneuvers.

THIS PAGE INTENTIONALLY LEFT BLANK

VI. CASE STUDIES

In this chapter, a number of case studies are used to show the results of analyzing standard sets of both RW and CMG arrays using the algorithms developed in the previous chapters. Additionally, the performance of non-standard analyses such as sensitivity analyses on RW balancing with respect to the array momentum envelope are included to show the flexibility of the algorithms.

A. MOMENTUM ENVELOPE

1. Reaction Wheels

For the following RW analysis, the wheel characteristics are based off of the Bradford Engineering W18 RW [15]. The important characteristics of the RW are as follows:

$$\omega_{RW_{max}} = +/- \ 4000\,RPM = 419 \ rad/\sec$$
$$\dot{\omega}_{RW_{max}} = +/- \ 55 \ rad/\sec^2$$
$$m = 5kg$$
$$I_{RW} = \begin{bmatrix} .0022 & 0 & 0 \\ 0 & .0022 & 0 \\ 0 & 0 & .0045 \end{bmatrix} kg \cdot m^2$$
$$\tau_{RW_{max}} = \pm 55(.0045) = .2475 \ N \cdot m$$

.

a. Nominal Momentum Space

When an RW array is composed of a single RW, the available momentum space forms a line that lies along the spin axis, as shown by Figure 19.

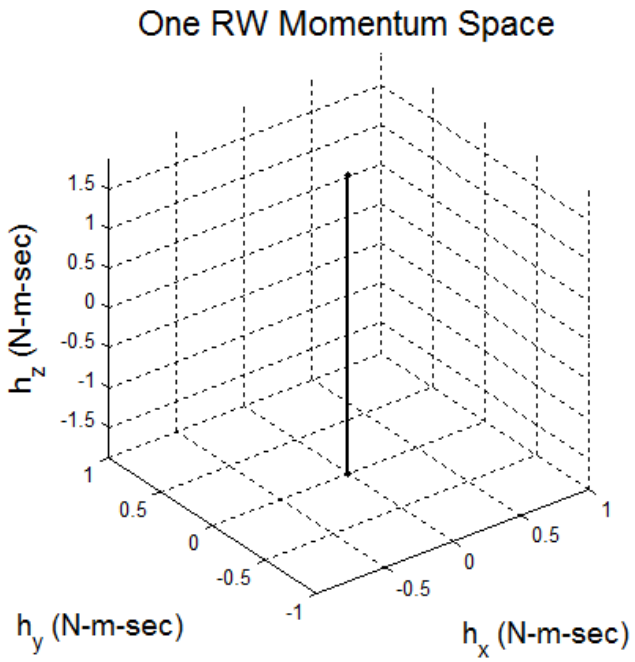

Figure 19. Momentum space for a single RW

For three RWs in an orthogonal configuration, the momentum space forms a box where each of the eight vertices is obtained by operating, in one of eight combinations, each RW at its fastest speed in either the forward or reverse direction. Figure 20 shows an example of this shape.

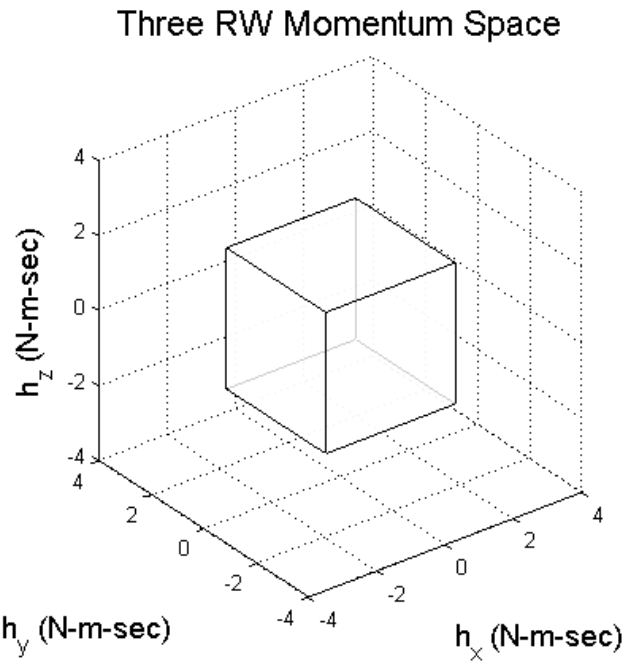

Figure 20. Momentum space for an array of three RWs in an orthogonal configuration

Adding a fourth RW and orienting all four RWs in the standard 54.73° pyramidal orientation [6], with γ and β angles given by Table 1, creates a more complex shape: a dodecahedron.

RW	γ (deg)	β (deg)
1	0	54.73
2	90	54.73
3	180	54.73
4	270	54.73

Table 1. Parameters for a four RW 54.73° pyramidal configuration

As before, the vertices represent different combinations of wheels operating at their maximum speed in either the forward or reverse direction. The dodecahedron is shown in Figure 21.

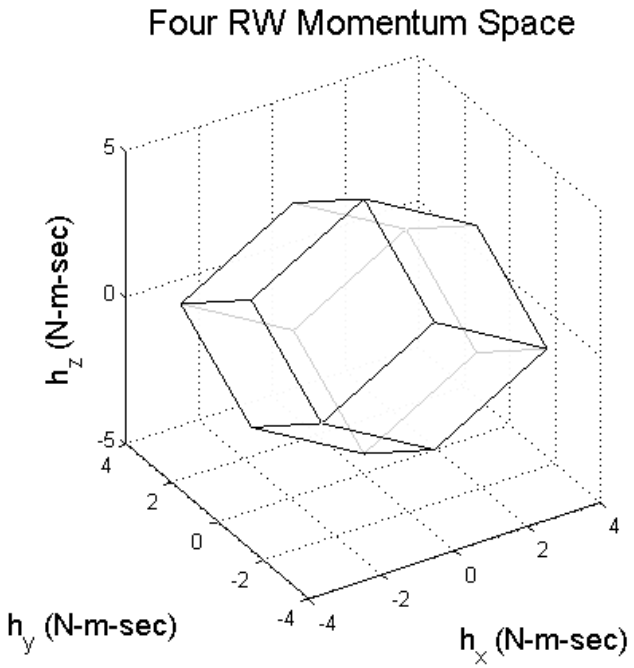

Figure 21. Momentum space for an array of four RWs in a 54.73° pyramidal configuration

Although there is more than one configuration of RW arrays, the characteristic of a given array will ultimately dictate its suitability for a given application. For the three RW box array, each dimension is driven by a single RW, so the size of each side is equal to twice the momentum capability of each wheel. For the four RW pyramidal array, the skewed RWs allow additional RWs to affect the array momentum, even if the desired direction is along the rotation axis of one of the RWs. Ultimately, this means the largest sphere that can fit inside the momentum volume for the pyramidal array is larger than that

for the box array. The theoretical maximum performing array according to the maximum sphere metric would be one that has a perfectly spherical momentum space. This would, however, be impractical to build as it would require a large number of devices.

b. Skewed Momentum Space

One benefit to calculating the momentum space using Equation (28) instead of Equation (22) is that wheel imbalances can now be taken into account.

Assuming that the same RW as analyzed above now contains a large imbalance such that the body z-axis of the wheel is offset from the principal z-axis by 10°, the single RW momentum space line becomes skewed as shown by Figure 22 when frozen at a particular instant in time. As the wheel rotates, the momentum vector will create a cone, an effect commonly called nutation [5, pg.53]. This makes the momentum vector time dependent and complicates the analysis.

One possible skewed inertia matrix is

$$\begin{bmatrix} 2.235x10^{-3} & -3.468x10^{-5} & 2.781x10^{-4} \\ -3.468x10^{-5} & 2.235x10^{-3} & -2.781x10^{-4} \\ 2.781x10^{-4} & -2.781x10^{-4} & 4.431x10^{-3} \end{bmatrix} kg-m^2 \ .$$

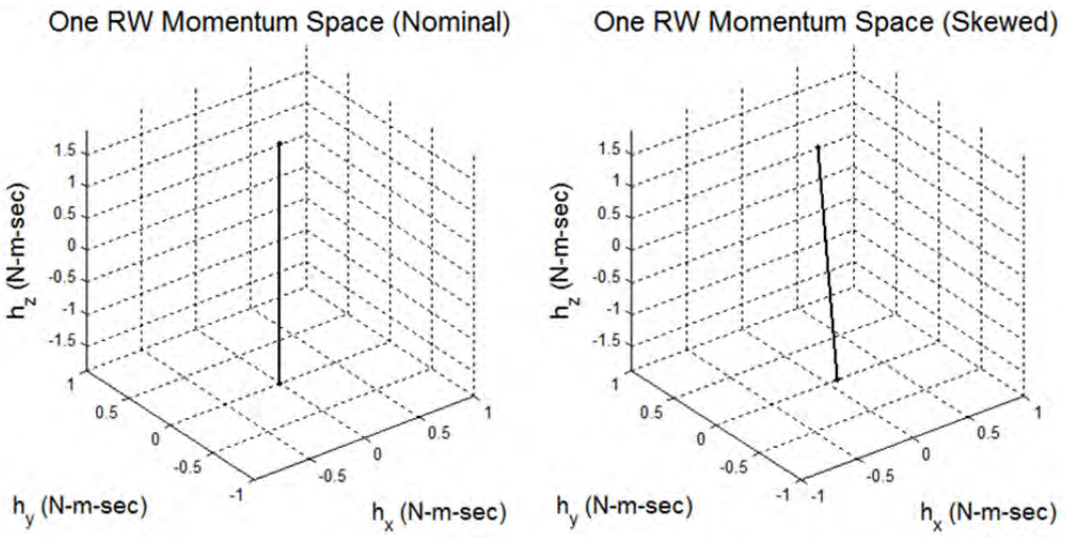

Figure 22. Balanced (left) and unbalanced (right) RW comparison

When applied to a three or four wheel array, these unbalanced wheels skew the entire momentum envelope. This is clearly shown in Figure 23. These shapes only apply when the noted requirement for the applicability of Equation (28) is met: that the shape is valid only for a particular instant in time. If examined over time, the shape would "breath" as each vertex moved with the momentum cone for each RW causing the faces to change size, shape and orientation.

Although the 10° offset makes the differences in the envelopes clear, the offset represents an imbalance that would result in a shortened component lifetime. More realistically, the offset would likely be much less than 1°.

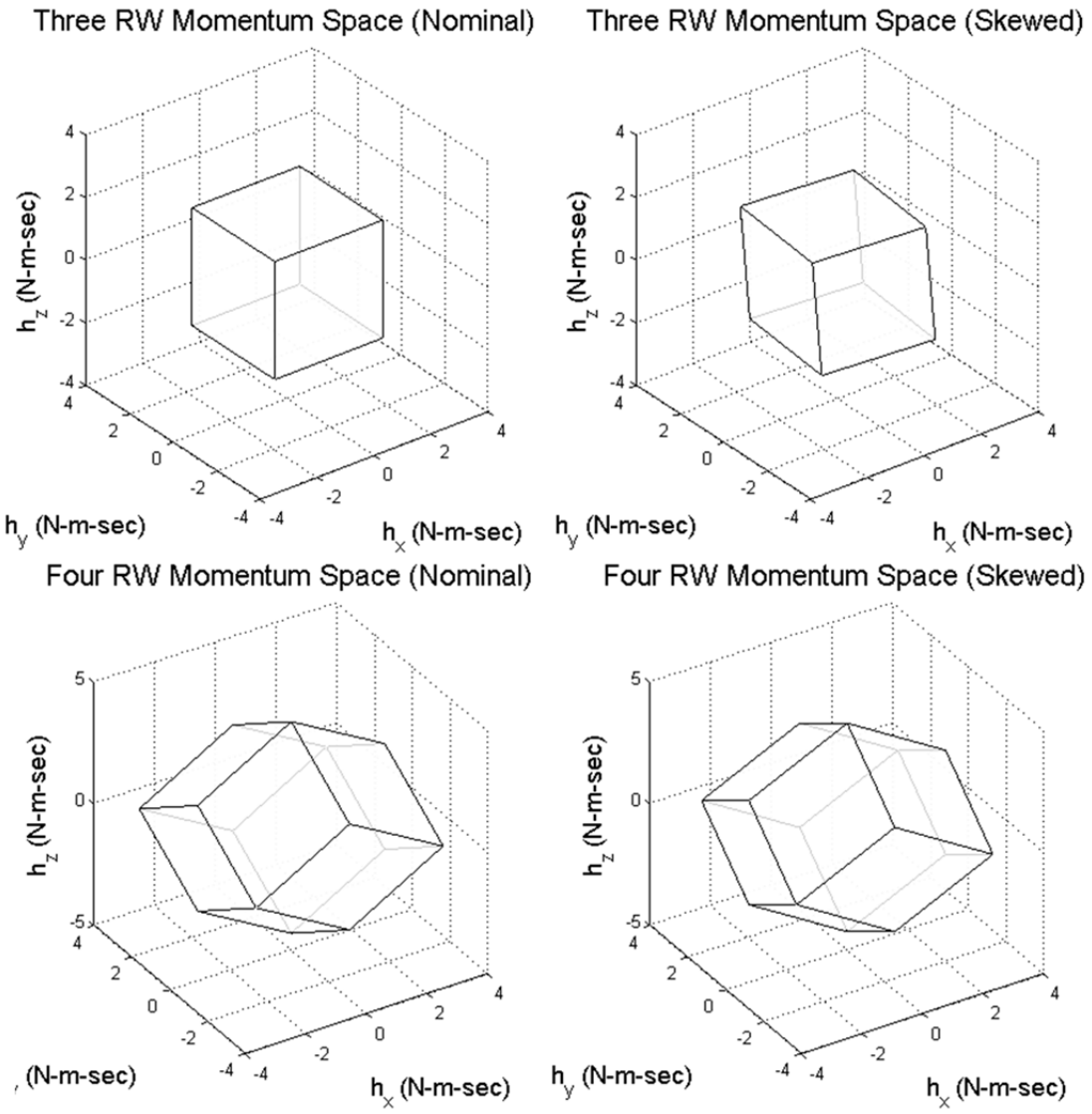

Figure 23. Balanced (left) and unbalanced (right) multi-RW array comparison

One question that arises from this study is what effect this skewed shape has on the total enclosed volume. A smaller enclosed volume represents a performance loss, so determining the degree of this loss in the range of expected imbalance represents a useful exercise. By iterating the offset angle and calculating the resulting momentum envelope volume, a relationship can be established, as shown in Figure 24 and Figure 25.

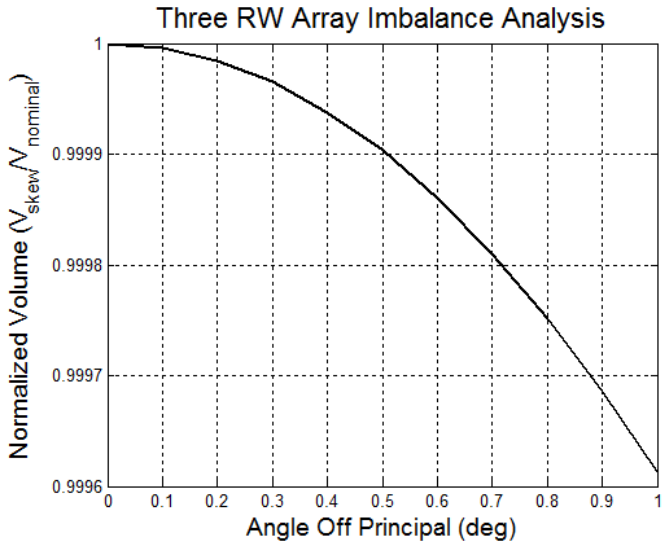

Figure 24. Three RW array imbalance sensitivity analysis

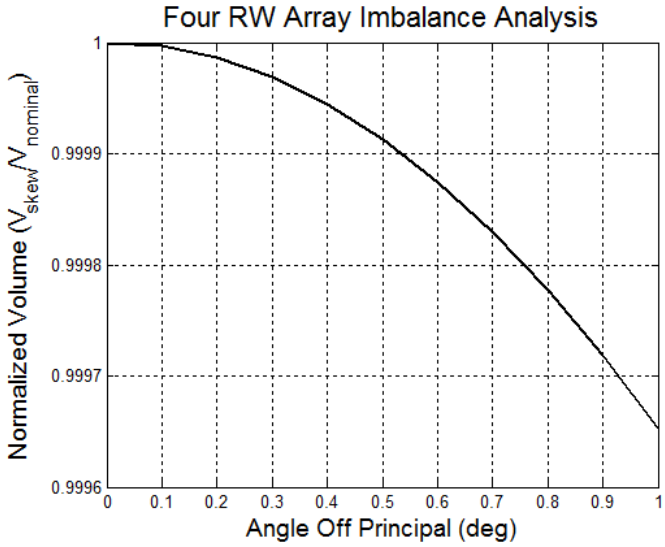

Figure 25. Four RW array imbalance sensitivity analysis

The results show less than a .04% performance drop at 1° skew. The small reduction in performance for what is still a large imbalance indicates that assuming the RW rotates about a principal axis will have a negligible impact on preliminary ACS design.

2. CMG Momentum Space

Consider the RW analyzed in the previous section now mounted on a gimbal. Further, assume that the wheel only rotates at its maximum speed in the forward direction and that the axis of rotation is the rotor x-axis, to be consistent with the system developed earlier. The available momentum space for a single CMG is a circle, as shown in Figure 27.

Figure 28 shows the angle residuals between the desired momentum vector and the momentum vector that the CMG can produce via the MIA process described in Chapter III, Section III.B.2. The desired direction vector is determined from the azimuth and elevation angles around the unit sphere. Figure 26 provides the convention to determine the direction of $\hat{d}$ using the ϕ (elevation) and θ (azimuth) angles. It is clear that this single CMG array can only match the desired vector when it lies in the plane of rotation. In other words, as the elevation component of $\hat{d}$ deviates from 0°, the residual from the MIA produced momentum vector will be equal to that deviation.

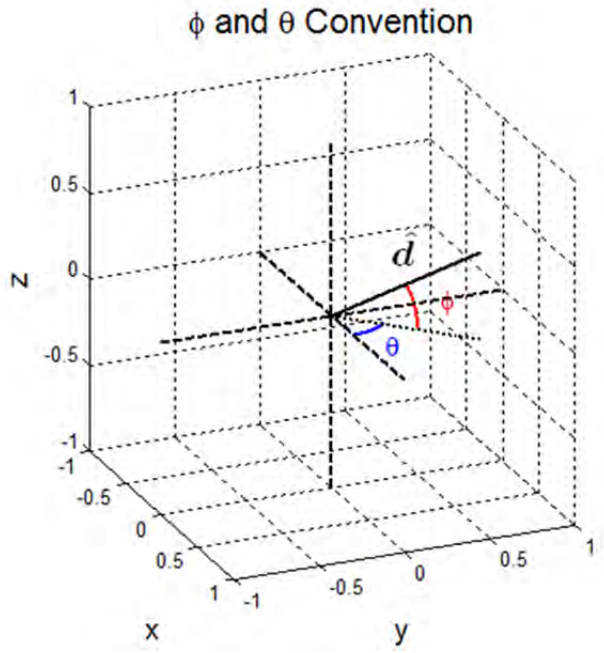

Figure 26. Convention for using ϕ and θ to describe $\hat{d}$

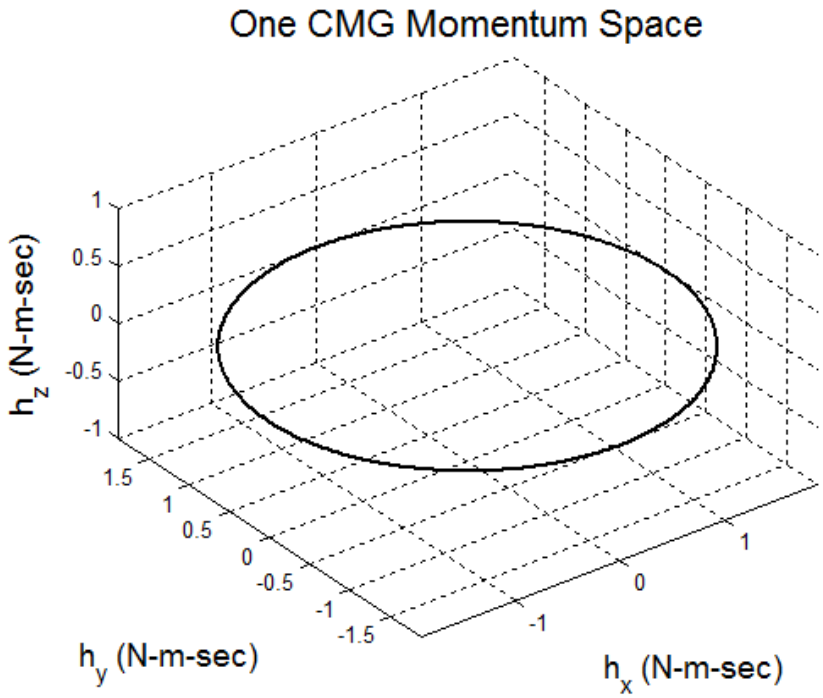

Figure 27. Momentum space for an array of one CMG

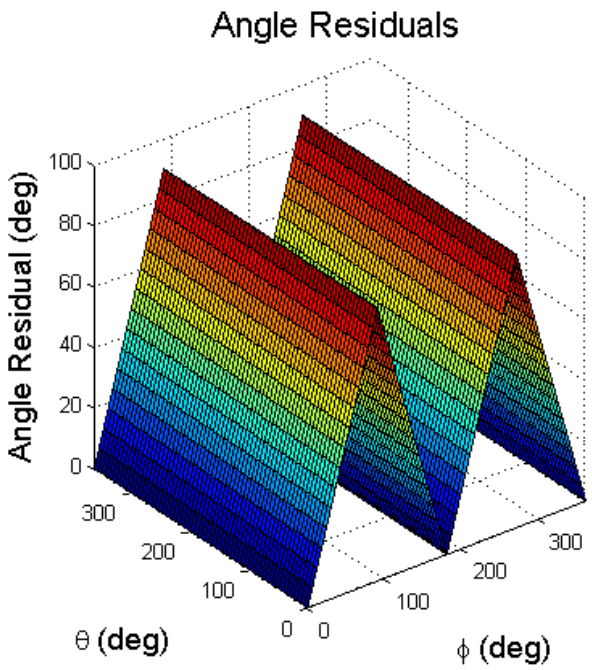

Figure 28. Angle residuals between the desired momentum vector and the actual momentum vector

Placing three CMGs in an orthogonal configuration gives a much more interesting shape, seen in Figure 29. Note that this figure represents the maximum momentum theoretically achievable in a given direction, however due to the presence of internal singularities it may not be physically possible to reach the surface in a given maneuver.

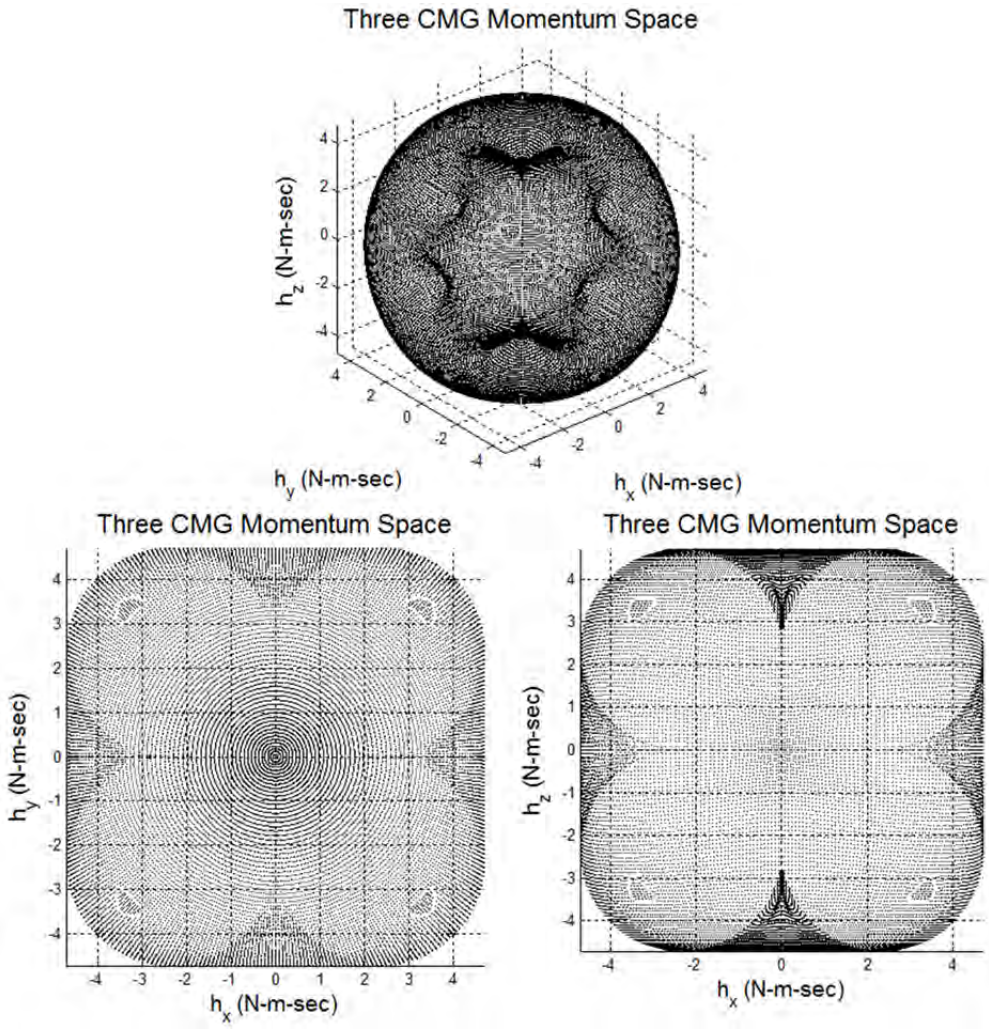

Figure 29. Three CMG array maximum momentum space.

Although a rigorous singularity analysis was not performed, it is likely that the conical shapes match the shape of a singularity surface [4] due to the relatively large angle residual shown in the vicinity of each by Figure 30.

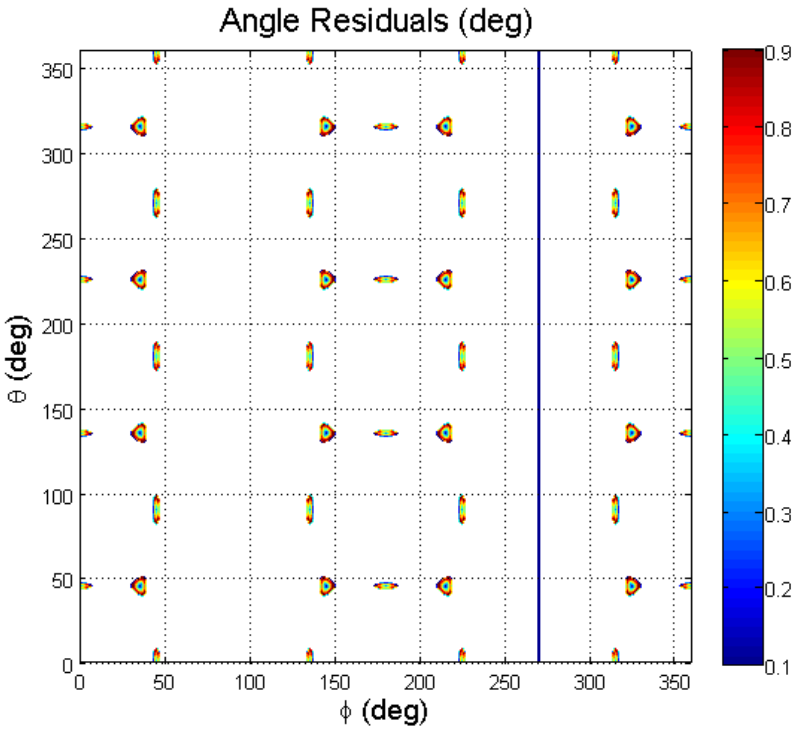

Figure 30. Three CMG array angle residual plot

For the 54.73° CMG pyramid, the standard shape appears in Figure 31. The large vertical stripes present at $\phi = 90°$ and $\phi = 270°$ in Figure 32 are likely due to a singularity present when $\hat{d} \approx \begin{bmatrix} \pm 1 \\ 0 \\ 0 \end{bmatrix}$. In these directions, changing θ has no effect on the direction of $\hat{d}$. This means that as the MIA algorithm sweeps through the azimuth values, the same residual will be seen. Further analysis is required to determine why the vertical stripe is not preset at $\phi = 90°$ for Figure 30.

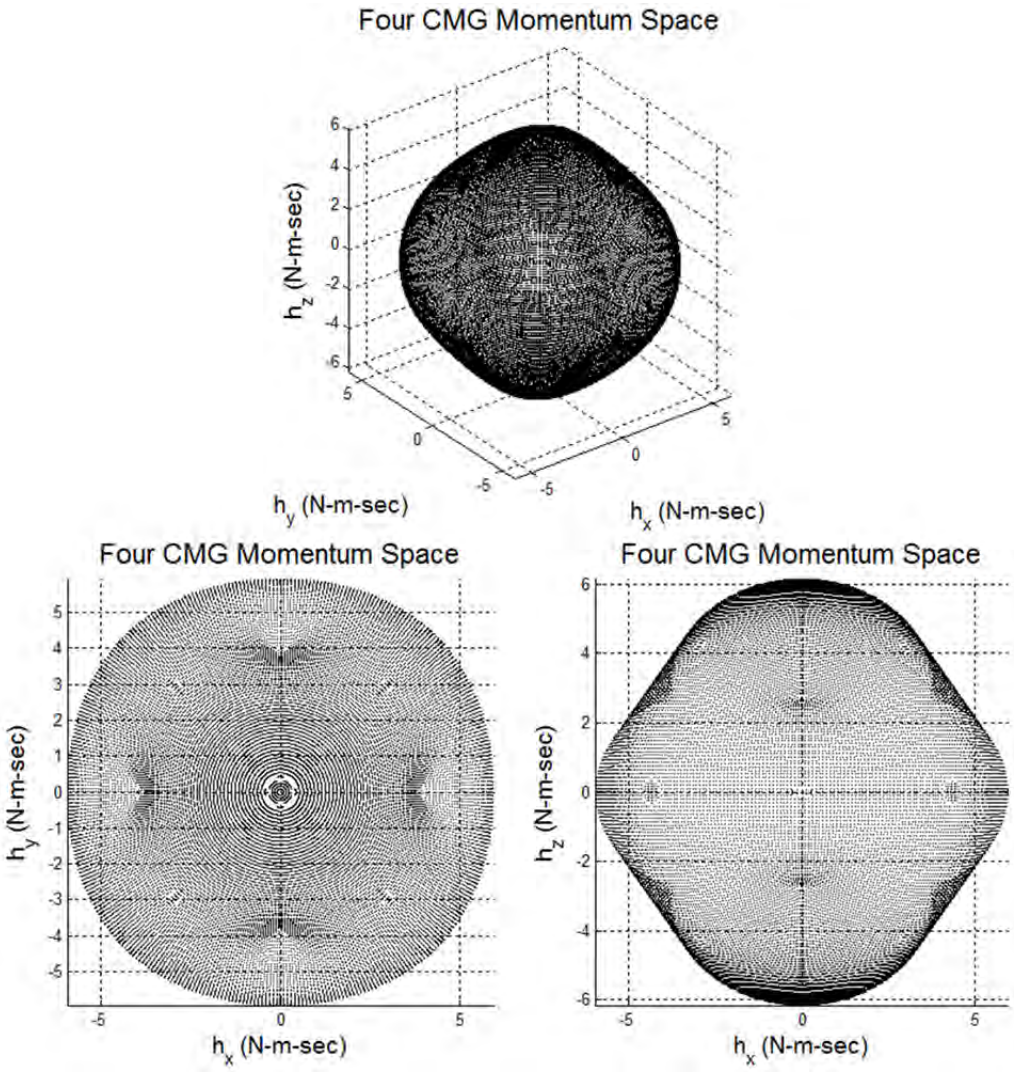

Figure 31. Four CMG array momentum space

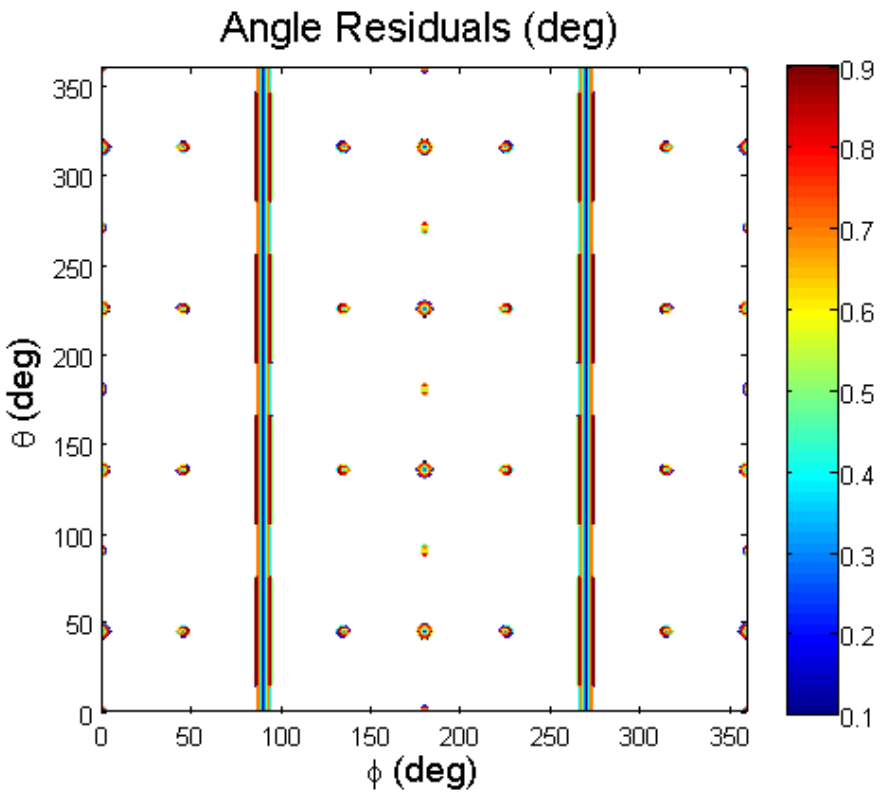

Figure 32. Four CMG array angle residuals

3. Hybrid RW/CMG Array

By maintaining all momentum data in point clouds, it becomes possible to analyze the maximum momentum surface of a composite array with both RWs and CMGs. To the best of the author's knowledge, such an analysis has not been reported in the literature. Figure 33 shows such an array, with three CMGs and three RWs oriented in two sets of orthogonal box arrays, similar to the three device cases analyzed previously.. There is some distortion of the CMG shape (beyond the increased size from adding the volumes). Internally, the CMG singularity surfaces get pushed to the border of the original RW surface, as that provides a singularity free volume.

This singularity free space implies that it may be possible to include a separate RW array on a spacecraft for the purpose of elliptic singularity avoidance. The RWs would allow a torque-generating CMG motion to bypass the singularity threshold, potentially allowing for an expanded utilization of the CMG performance envelope, or the ability to use a simplified steering law.

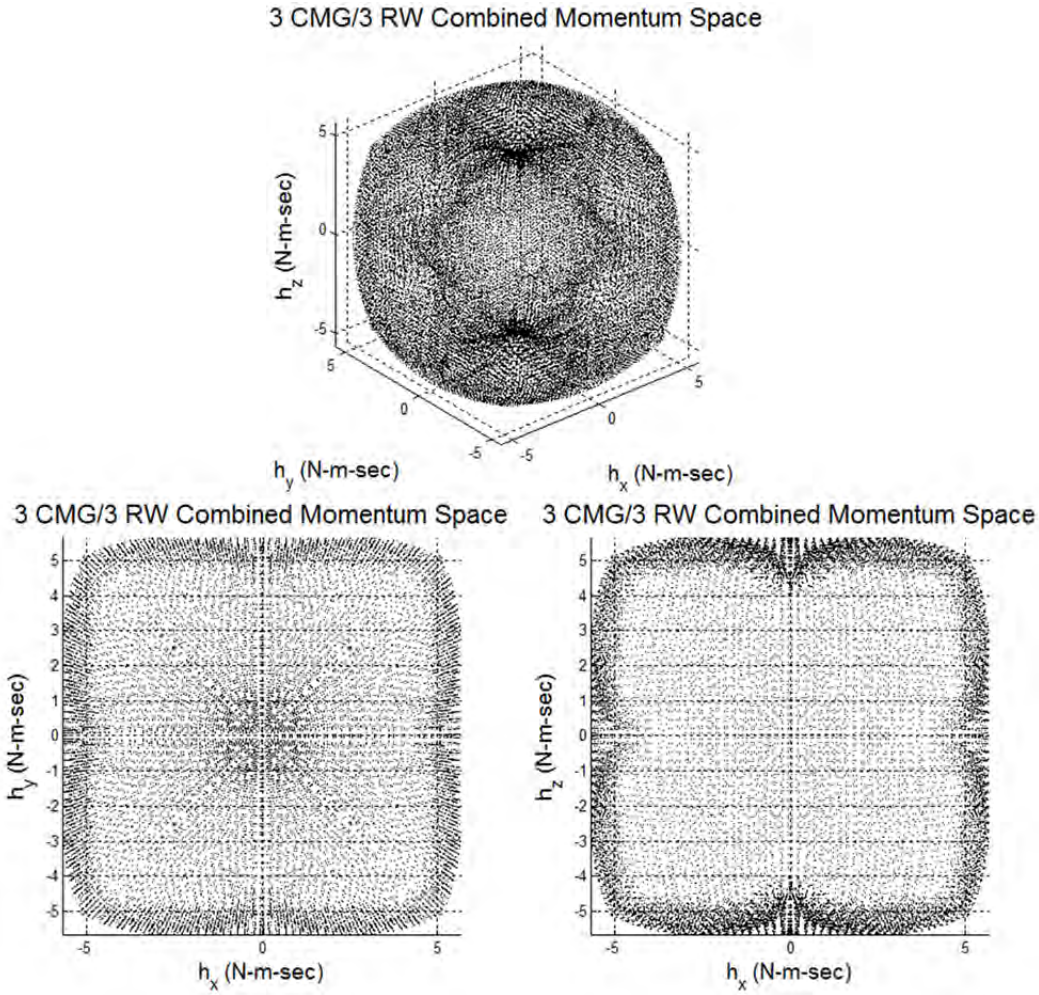

Figure 33. Composite array momentum volume for a three RW/three CMG hybrid MED system

B. TORQUE ENVELOPES

1. Reaction Wheels

With the momentum vector for the RW being essentially fixed along the rotation axis (assuming a perfectly balanced wheel), the torque space assumes the same shape as the momentum space, as seen in the torque space for the four RW pyramidal array in Figure 34. The other configurations are similar to the example shown in the previous section.

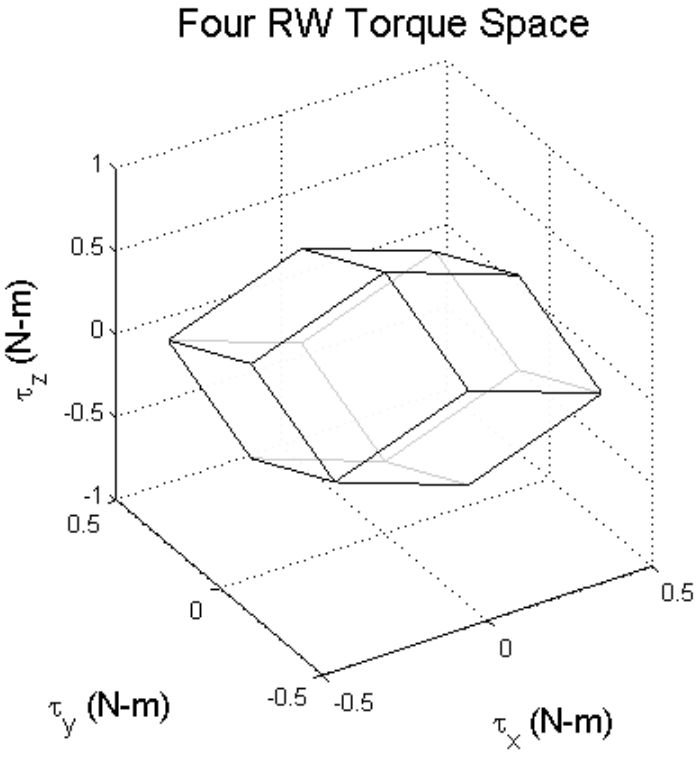

Figure 34. Four RW pyramid array maximum torque space

2. CMG Torque Space Analysis

a. Reduced Dimensional State Space $\mathbb{R}^3$ Analysis

When dealing with state space representations of a CMG array, as discussed in Chapter III Section C, it is

very important to maintain the contiguous or semi-contiguous condition when reducing dimensionality.

There are several possible metrics that can be calculated for the state space analysis. One typical analysis is based on testing the singularity condition (SC) of a particular state as defined by Equation (102) [8, pg. 467].

$$SC = \det(AA^T) \tag{102}$$

Where A can be defined as in Equation (103).

$$\dot{h}_{array} = A\begin{bmatrix} \dot{\delta}_1 \\ \vdots \\ \dot{\delta}_n \end{bmatrix} \tag{103}$$

For the case $n > 3$, a non-zero SC implies that the pseudoinverse control allocation, $A^+ = A^T\left(AA^T\right)^{-1}$, exists because AA^T is invertible. Thus, a vector of gimbal rates can be found that will satisfy Equation (103). Therefore, developing a state space map based on the SC of each state allows a region of gimbal angles for each CMG to be created that is singularity free.

Figure 35 shows a map of the SC based on state index value, with Figure 36 showing the gimbal angles based on state index number with zero representing the bottom left corner of the singularity free box and increasing to the right and up for state index one and two, respectively. The state indexes themselves were created by taking pairs of CMGs (one and two for the first state index, three and four for the second) and allowing the gimbal angle of one CMG in each pair to cycle through an entire circle before

incrementing the other CMG in the pair. This continued until the second CMG gimbal angle had gone through $360°$. Figure 37 describes the process in pseudo code.

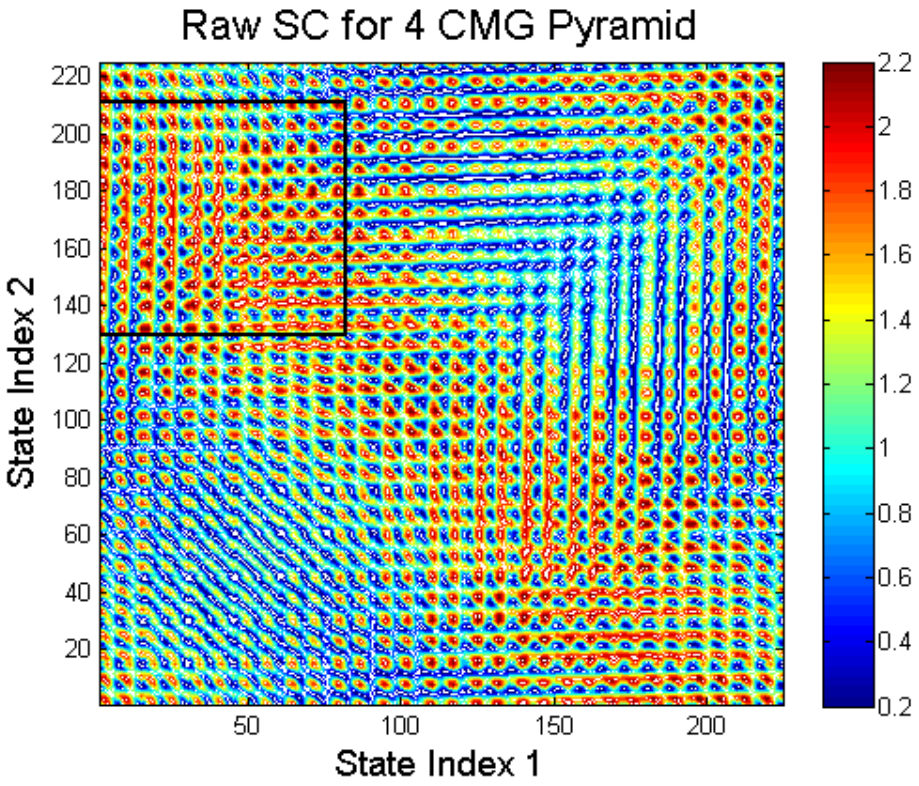

Figure 35. Four CMG pyramid reduced dimensional state space analysis showing raw SC data

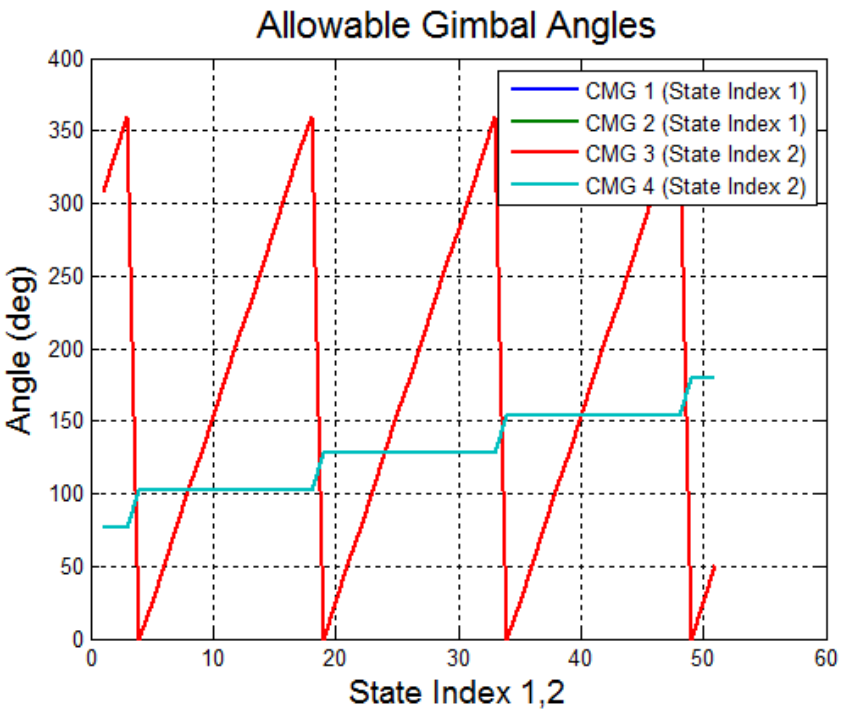

Figure 36. Four CMG pyramid reduced dimensional state analysis gimbal angle constraints

```
for gimbal2 = 1 to 360
   for gimbal1 = 1 to 360
      stateindex1(kk) = [gimbal1,gimbal2]
      gimbal1 = gimbal1 + increment
      kk = kk + 1
   end
   gimbal2 = gimbal2 + increment
end
```

Figure 37. Pseudo code representation of the creation of the state indices

Figure 38 shows the state conditions that meet the inequality $SC > 0$. The black box present in Figure 36 and Figure 38 indicate the identified singularity free

region, based on a simple search algorithm that finds the largest square area that meets the required condition.

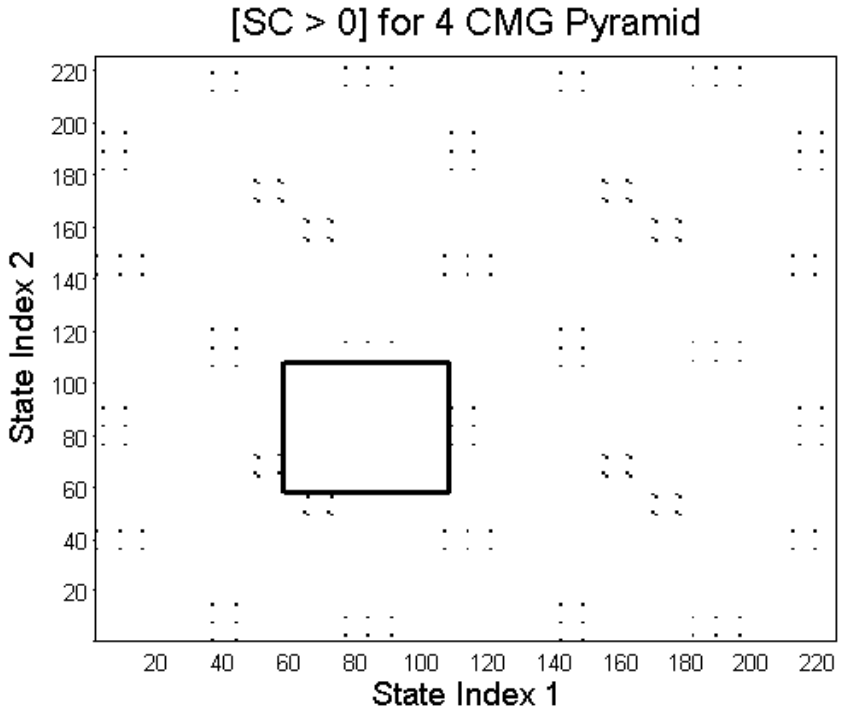

Figure 38. Four CMG pyramid reduced dimensional state analysis showing analyzed SC data

Although the gimbal limits can be pulled off of Figure 37, understanding that the steps seen in CMG four represent the resolution of gimbal angles analyzed underscores the fact that this representation is not very accurate. The purpose of using such large steps initially is to reduce the analyzed state space since each gimbal has to be varied through the entire 360°. By using the resulting gimbal limits in a subsequent iteration and maintaining the number of steps for each angle range, the results can be refined at the same speed as the initial examination. This can be continued until the desired accuracy is developed. Figure 39 shows the results for the

second and third iteration while Table 2 gives the gimbal angle limits for each iteration.

Iteration		CMG 1 (deg)	CMG 2 (deg)	CMG 3 (deg)	CMG 4 (deg)
1	Low	0.00	77.14	0.00	77.14
	High	360.00	180.00	360.00	180.00
2	Low	0.00	57.30	0.00	155.52
	High	360.00	118.68	360.00	229.18
3	Low	0.00	65.48	0.00	139.15
	High	360.00	122.78	360.00	196.44

Table 2. Gimbal limits per iteration for four CMG pyramid reduced dimensional state space analysis based on SC

The point-cloud momentum space resulting from the calculated gimbal angle limits is given in Figure 40. For these gimbal angles, there is a much larger proportion of volume in the positive x-y-z octant. So although the momentum space volume may be sufficient, the location of this volume with respect to the origin may not. For comparison purposes, Figure 41 shows the limited momentum space plotted within the unlimited momentum space.

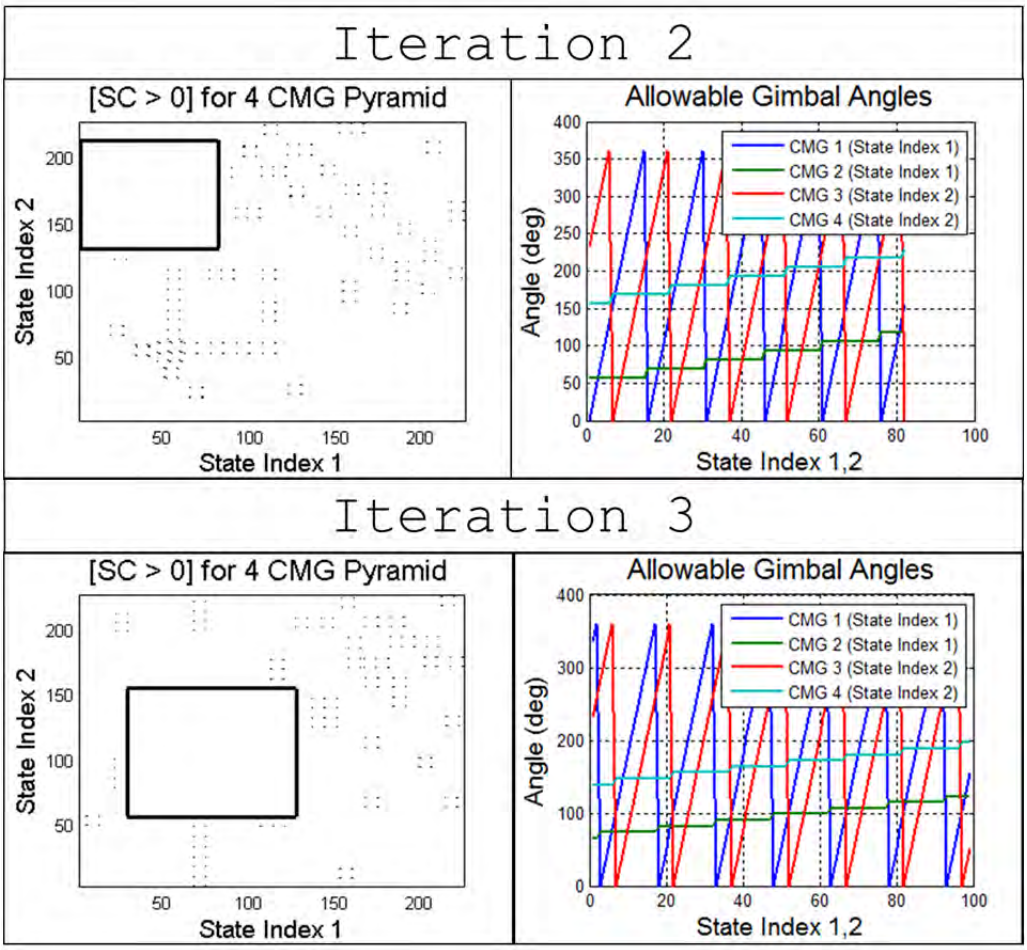

Figure 39. Results of iteration two and three for the four CMG pyramid reduced dimensional state space analysis based on SC

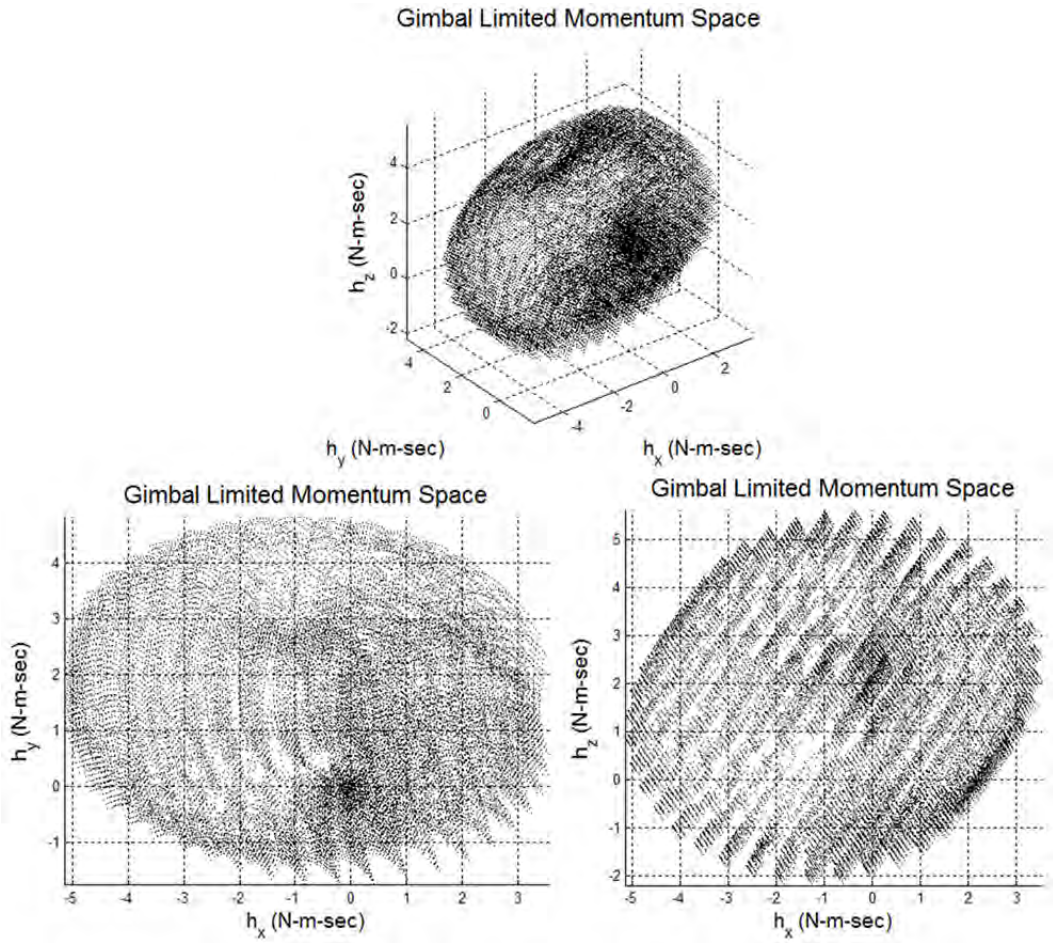

Figure 40. Momentum space for gimbal angle limited four CMG pyramid reduced dimensional state space analysis based on SC

A useful, though not exhaustive, test to determine if the volume is singularity free is to pick two points within the volume and use a simple pseudoinverse controller to drive the four CMG array from one momentum state to another. Under normal circumstances, the pseudoinverse control law tends to drive the array towards a singularity, but by staying within the declared boundaries singularities can be avoided.

Figure 42 and Figure 43 show the result of this test, using a simple PD controller to drive the momentum error to zero.

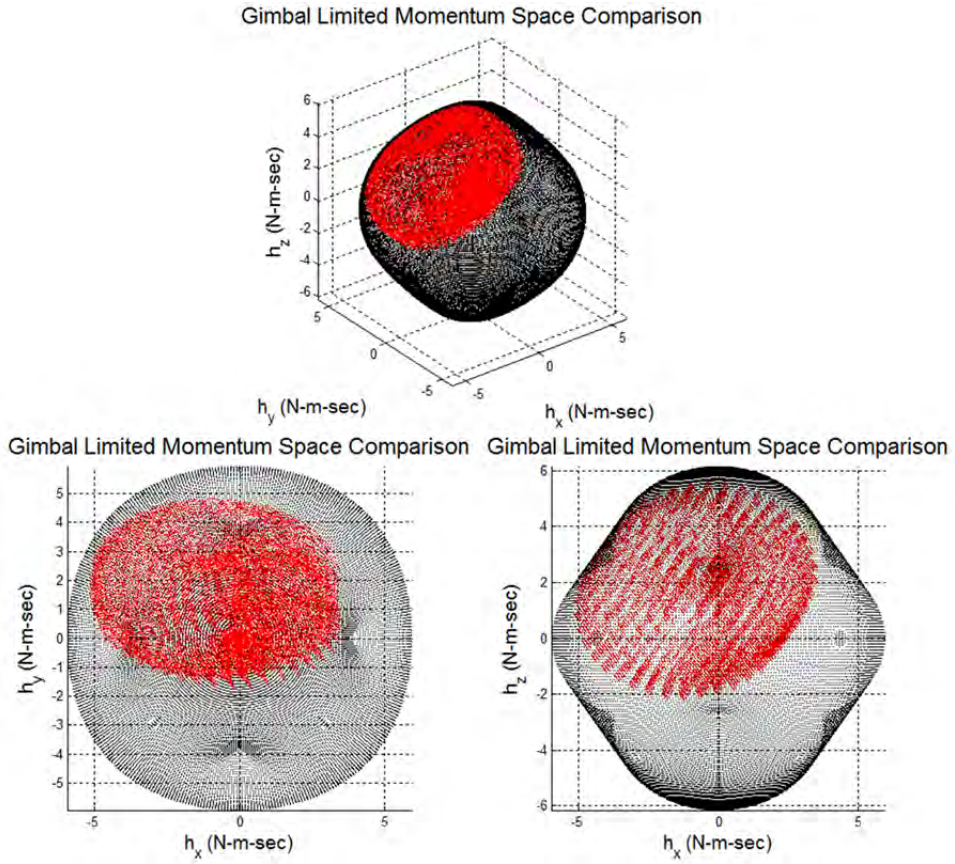

Figure 41. Reduced dimensional limited- and unlimited-gimbal angle four CMG pyramid momentum space comparison

Normal attitude control operations do not calculate actual angular momentum values; they are usually based on current and final quaternions. If doing a standard eigenaxis maneuver using quaternions, the intermediate step of calculating angular momentum and ensuring the trajectory stays within the bounds (difficult due to the irregular shape of the volume) can be neglected

by simply ensuring all CMGs stay within their gimbal angle bounds.

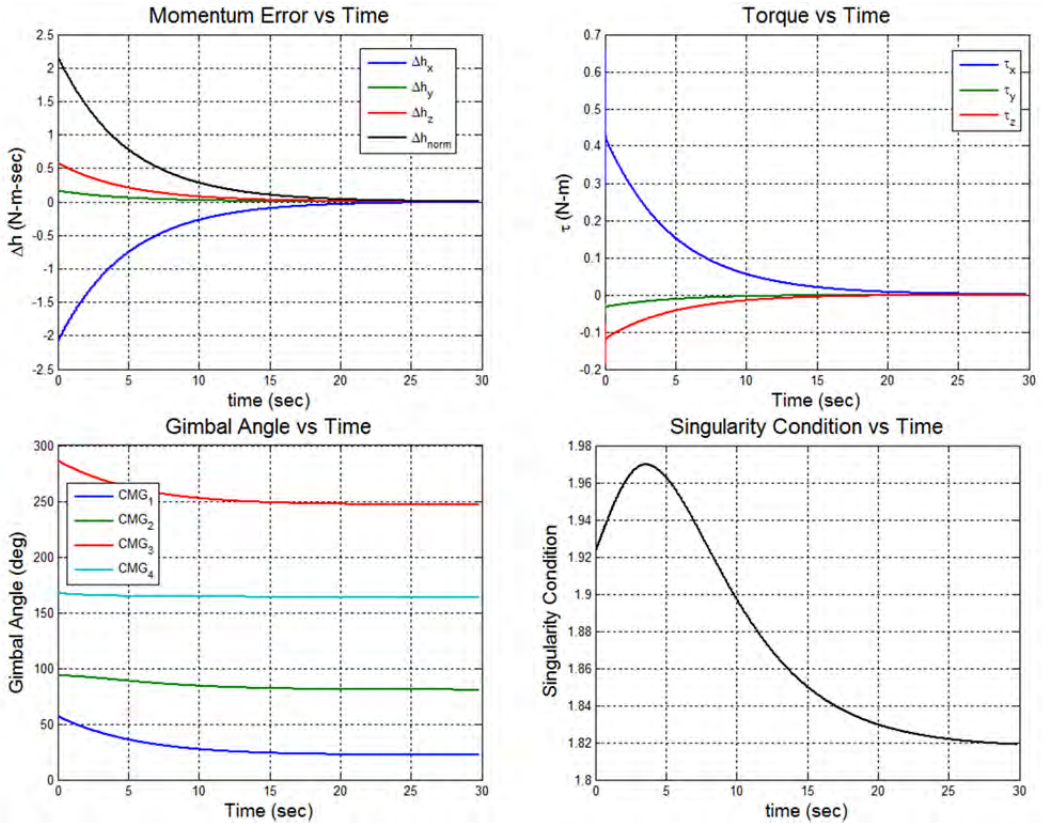

Figure 42. Pseudo-inverse control law operation in singularity free CMG momentum space

When using the pseudo-inverse control law as a basis, there are several difficulties to overcome when designing this new implementation. First of all, controlling gimbal rate behavior near gimbal angle boundaries is very important. It would be very undesirable to generate a high gimbal rate in an adverse direction, forcing the CMG across the operational boundary. To minimize rate changes, one can simply convert to a delta form of the control law as given in Equation (104).

$$\dot{\delta} = \Delta\dot{\delta} + \dot{\delta}_0$$
$$\dot{h} = A\left(\Delta\dot{\delta} + \dot{\delta}_0\right) \qquad (104)$$
$$\Delta\dot{\delta} = A^{+}\left(\dot{h} - A\dot{\delta}_0\right)$$

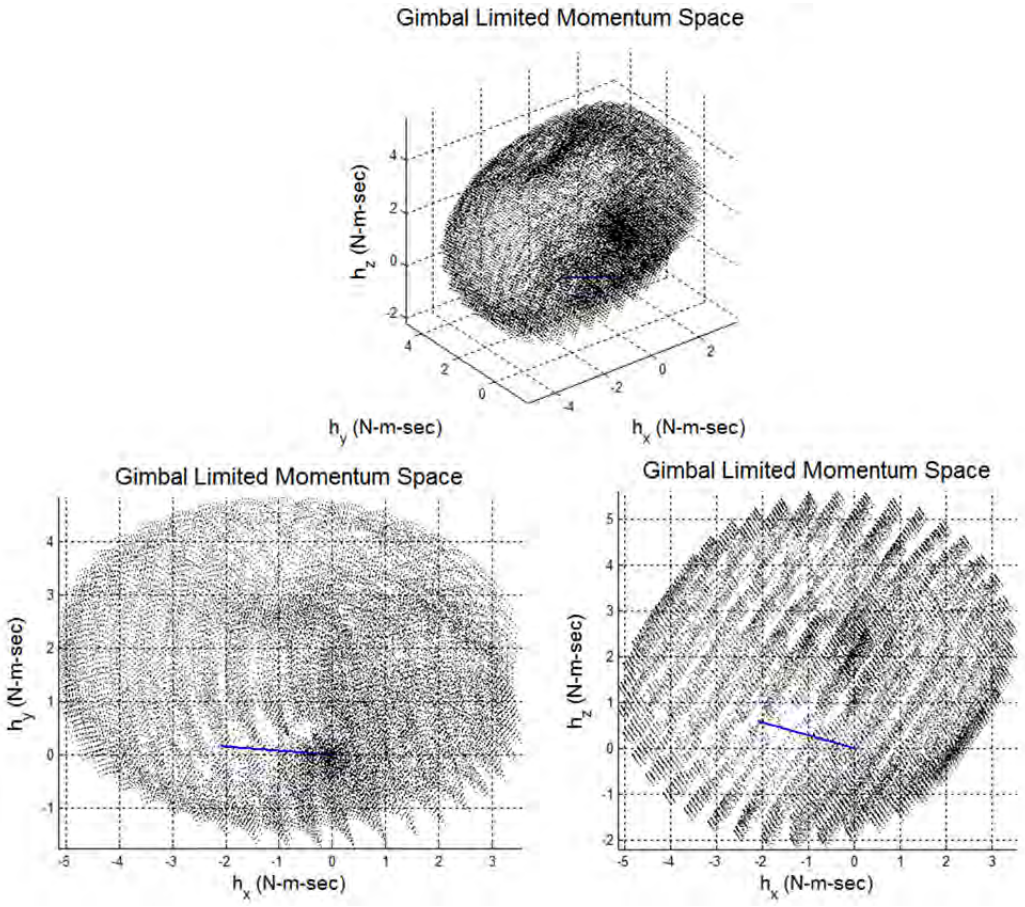

Figure 43. Pseudo-inverse control law momentum trajectory in singularity free CMG momentum space

The properties of the least squares solution will then minimize $\left\|\Delta\dot{\delta}\right\|_2$, thus minimizing gimbal rate changes [16].

It is also necessary to ensure that the gimbal rates tend to avoid the saturation conditions. To make this happen, a weighting factor, w_f, can be added to

Equation (94). This factor will act to drive the solved $\Delta\dot{\delta}$ such that $\Delta\dot{\delta}+\dot{\delta}_0$ will direct the gimbal away from the limit. The full steering control law is given in Equation (105).

$$\begin{aligned}\dot{h} &= A\left(\Delta\dot{\delta}+\dot{\delta}_0+w_f\right)\\ \Delta\dot{\delta} &= A^{+}\left(\dot{h}-A\dot{\delta}+Aw_f\right)\end{aligned} \tag{105}$$

Although no analysis has been completed to determine create a working example of Equation (105), it is likely that the design of a w_f function to achieve the desired behavior will be the most challenging part.

b. Full Dimensional State Space $\mathbb{R}^{n+1}$ Analysis

One of the primary benefits of reduced dimensional analysis lies with the fact that intermediate results can be represented in a form that is fully representable in $\mathbb{R}^3$. A close inspection of the state index plot in Figure 39 shows that not all permutations of CMG gimbal angle states are analyzed. Though the states that are analyzed are contiguous, there are additional contiguous states that are ignored. This is the heart of why the previous analysis was characterized as semi-contiguous. The unanalyzed states impose unnecessarily restrictive constraints on the CMG array based on the gimbal angle limits.

A fully contiguous analysis representation requires a five dimensional plot for the system being analyzed. This plot cannot be easily displayed for visualization with current technology. Fortunately, the same analytical principles still apply.

By storing the SC values in a four dimensional matrix, a hypercube can be formed within that matrix to determine the gimbal angle limits for singularity free space. With these limits, similar analyses such as the momentum space point cloud can be performed.

Table 3 provides the results for each iteration of the full dimensional state space analysis while Figure 44 and Figure 45 give the momentum space and provide a comparison to the prior methods, respectively.

Iteration		CMG 1 (deg)	CMG 2 (deg)	CMG 3 (deg)	CMG 4 (deg)
1	Low	25.71	102.86	25.71	102.86
	High	180.00	257.14	180.00	257.14
2	Low	0.00	193.40	0.00	193.40
	High	113.65	322.48	113.65	322.48
3	Low	0.00	167.90	21.51	199.92
	High	86.05	295.97	107.57	327.98

Table 3. Iterative results for the full dimensional state space analysis of the four CMG pyramid

The complexities of the gimbal limited shapes make comparison between the two methods difficult. One fairly simple metric to compare the full and reduced dimensional shapes is to compare the radii of the largest sphere centered at the origin that can be inscribed within the volume of the shapes. For the reduced dimensional analysis case, this radius is approximately $0.1241 h_{cmg}$ N-m-s while for the full dimensional analysis case it is approximately $0.0689 h_{cmg}$ N-m-s. The full dimensional momentum space, however, is much more centered than the reduced dimensional analysis momentum space. The spheres

are shown superimposed on the respective shapes in Figure 46 and Figure 47.

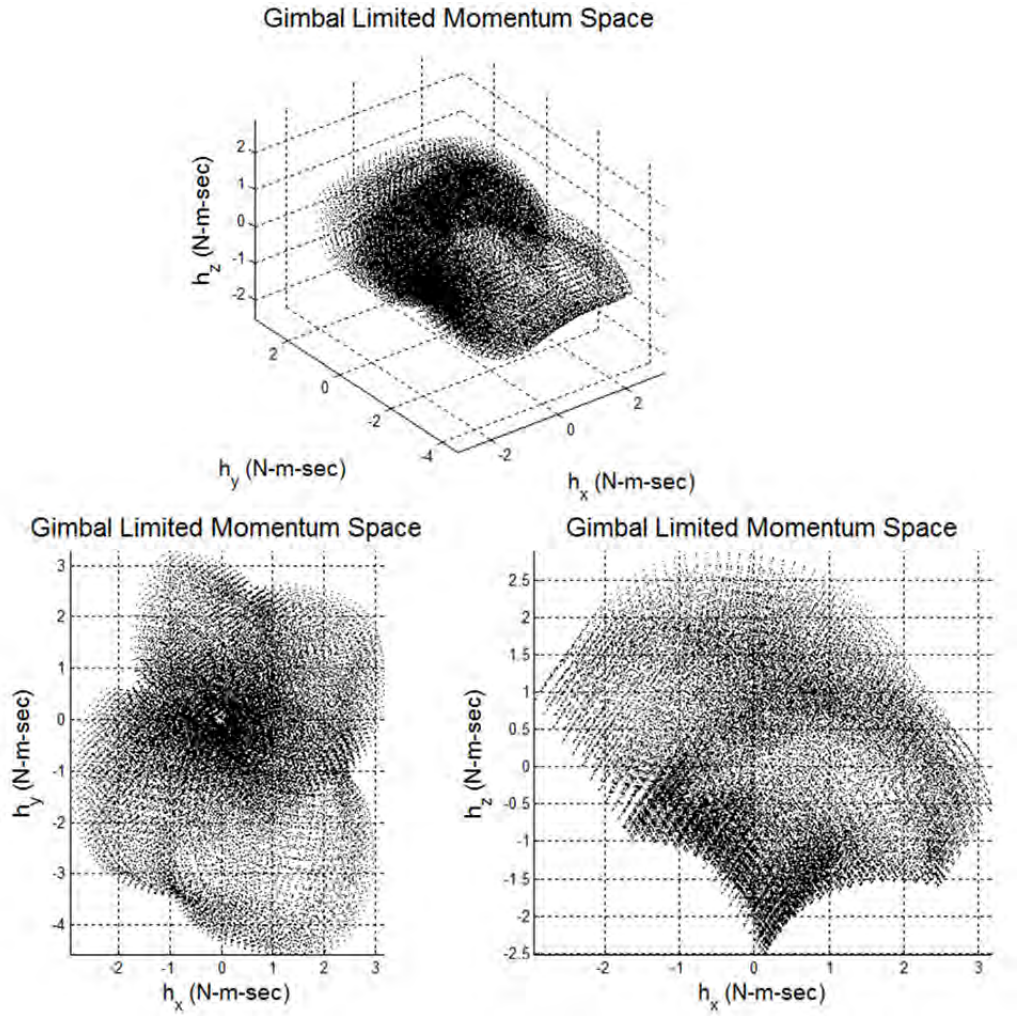

Figure 44. Four CMG pyramid full dimensional state space analysis-based singularity free momentum space

Although Crews ([4]) indicates that the maximum singularity-free sphere has a radius of $1.0069 h_{cmg}$ N-m-s, a number which greatly exceeds the normalized radius of $0.0689 h_{cmg}$ N-m-s for the full dimensional state space analysis and $0.1241 h_{cmg}$ N-m-s for the reduced dimensional state space analysis, the difference is expected. The

1.0069h_{cmg} N-m-s sphere is based only on neglecting elliptic singularities while this state space analysis avoids all singularities. Reanalyzing the gimbal limits by allowing hyperbolic singularities within the operating momentum volume will increase the available performance. Additionally, the gimbal limits are based on finding the largest singularity-free square or hypercube due to the simplicity of implementing the search algorithm as well as the simplicity of analyzing the resulting gimbal limits. This provides an additional performance constraint as it does not include all contiguous states in the maximum area or hypervolume that are singularity free. Finally, a voxel based maximal surface detection algorithm may improve the performance of the state space analysis with respect to the maximum sphere metric.

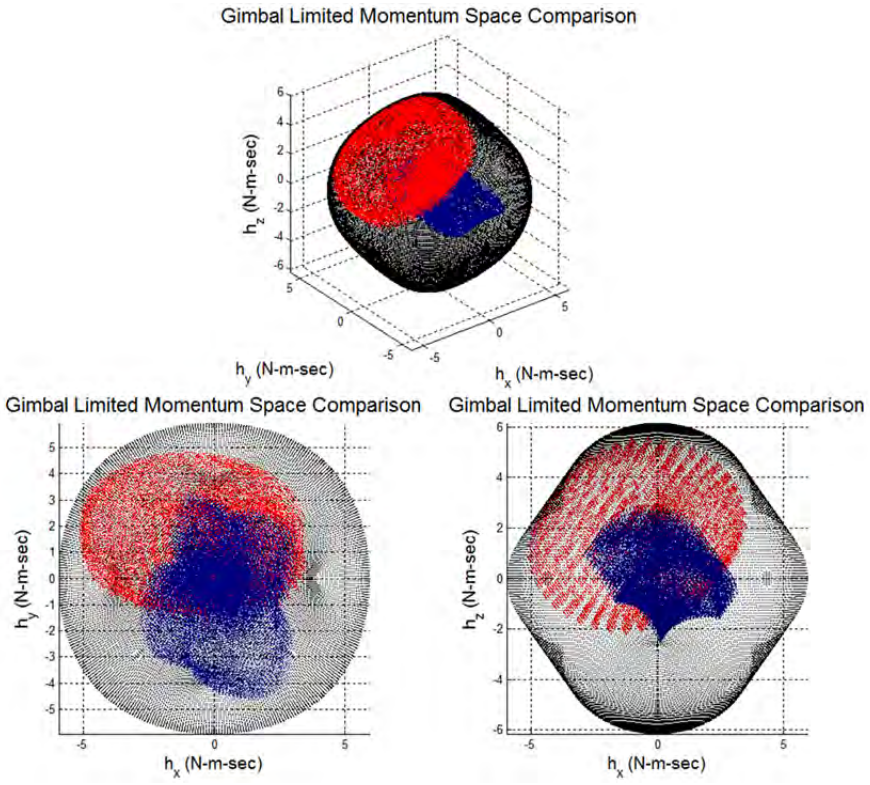

Figure 45. Four CMG singularity free momentum space comparison

Due to the difficulty in visually comparing the complex surfaces of singularities [4,17] and the complex shape of Figure 44, further study is required to verify that the results of the state space analysis matches those found in the literature.

Additional work is required to fully determine whether reduced dimensional state space analysis provides sufficient performance or if a full dimensional state space analysis is required to maximize array performance. Ultimately, the result may depend on the application.

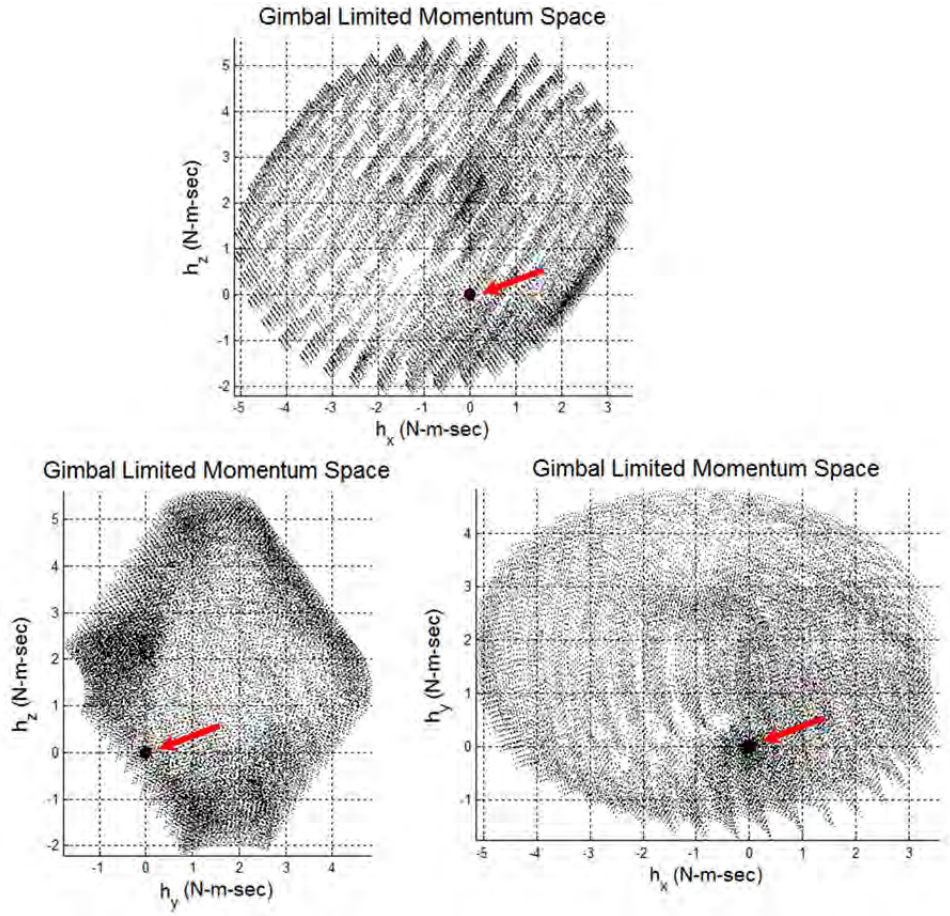

Figure 46. Maximum sphere superimposed on the reduced dimensional state space analysis-based singularity free momentum space

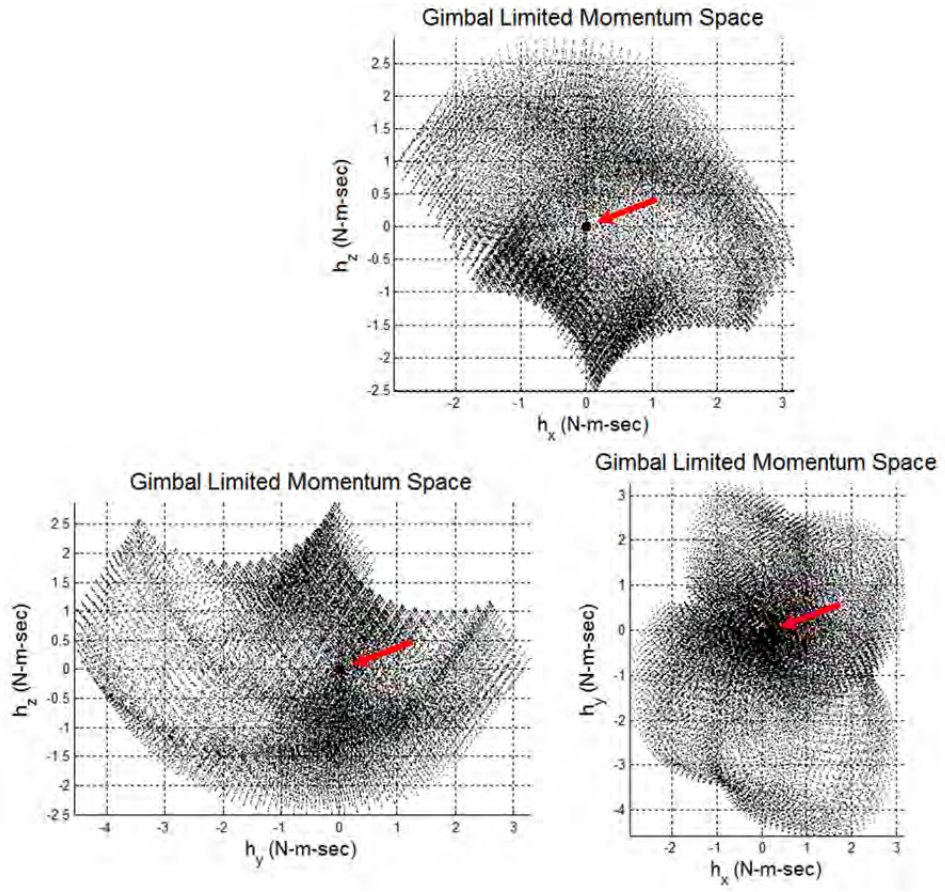

Figure 47. Maximum sphere superimposed on the full dimensional state space analysis-based singularity free momentum space

C. REACTION FORCES

1. Validation and Verification

Due to the lack of material in literature as compared to torque and momentum space studies, rigorous validation and verification of the reaction force equations was required. The general methodology used to conduct the validation and verification involved identifying particular initial conditions that output a simple, intuitive result, preferably involving a single parameter such as axial torque or transverse force.

There are two primary aspects that need to be verified. The first is the inertial motion of the MED. This is the right hand side of the force-balance equation. The inertial motion equation determines the linear and rotational trajectories based on known system geometry and simulated or real-world telemetry. The other aspect is the left hand side of the force-balance equation. It is the summation of all moments and forces and is used to determine the reaction forces and moments. Within those two primary sections are a total of six parts to be verified: forces in the axial and both transverse directions and moments in the axial and both transverse directions.

a. Reaction Wheel Inertial Motion Verification

For the reaction wheel tests, the initial conditions and results are given in Table 4 through Table 9. The RW is assumed to be oriented such that the spin axis is parallel with the z-axis of the spacecraft and has the following physical characteristics:

$$I_{rw} = \begin{bmatrix} 1 & 0 & 0 \\ 0 & 1 & 0 \\ 0 & 0 & 1 \end{bmatrix} kg - m^2$$

$$m = 1\ kg$$

The first test examines rotations in the axial direction and is broken up into four parts. The first two parts have the RW centered in the spacecraft body and have the RW accelerate at a constant rate and the spacecraft accelerate at a constant rate, respectively. The results for these tests give the expected inertial moment in the axial direction. The third part involves the RW

accelerating at a constant rate in one direction and the spacecraft accelerating at the same rate in the opposite direction. These two motions cancel each other out, resulting in no inertial moments or forces applied to the RW. The final part has the RW displaced from the center of the spacecraft and has the spacecraft rotating at a constant rate. The result shows an inertial force oriented towards the center of the spacecraft.

					Applied Ang. Accel. (rad/sec^2)				Initial Ang. Rates (rad/sec)			
		RW Location (m)			S/C			RW	S/C			RW
		$X_{S/C}$	$Y_{S/C}$	$Z_{S/C}$	x	y	z	z	x	y	z	z
Test 1	a	0	0	0	0	0	0	0.1	0	0	0	0
	b	0	0	0	0	0	0.1	0	0	0	0	0
	c	0	0	0	0	0	-0.1	0.1	0	0	0	0
	d	0.1	0	0	0	0	0	0	0	0	1	0

Table 4. RW V&V test one initial conditions

		RW Inertial Force (N)			RW Inertial Moment (N-m)		
		x	y	z	x	y	z
Test 1	a	0	0	0	0	0	0.1
	b	0	0	0	0	0	0.1
	c	0	0	0	0	0	0
	d	-0.1	0	0	0	0	0

Table 5. RW V&V test one results

					Applied Ang. Accel. (rad/sec^2)				Initial Ang. Rates (rad/sec)			
		RW COM Location (m)			S/C			RW	S/C			RW
		$X_{S/C}$	$Y_{S/C}$	$Z_{S/C}$	x	y	z	z	x	y	z	z
Test 2	a	0	0	0	0	0.1	0	0	0	0	0	0
	b	0	0	0	0.1	0	0	0	0	0	0	0
	c	0	0	0	0	0.1	0	0	0	0	0	0.2

Table 6. RW V&V test two initial conditions

		RW Inertial Force (N)			RW Inertial Moment (N-m)		
		x	y	z	x	y	z
Test 2	a	0	0	0	0	0.1	0
	b	0	0	0	0.1	0	0
	c	0	0	0	*	0.1	0

Table 7. RW V&V test two results

$$* \Rightarrow \boxed{\tau_x = \frac{0.1}{5} t\left(N - m\right)}$$

The second test is composed of three parts and examines transverse motions. For all parts of this test, the RW is located at the center of the spacecraft. Parts one and two have the spacecraft with a rotational acceleration along a single transverse axis. The results show an inertial moment along the corresponding axis with the appropriate magnitude. The third part repeats the first, however the RW is now rotating at a constant rate along its spin axis. The results show a constant inertial moment along the appropriate transverse axis as well as a linearly increasing inertial moment about the other transverse axis. This increasing moment matches the expected behavior of a CMG, which is what the initial conditions for the third part simulated.

					Applied Linear Accel. (m/sec^2)		
		RW COM Location (m)			S/C		
		$X_{S/C}$	$Y_{S/C}$	$Z_{S/C}$	x	y	z
Test 3	a	0	0	0	0.1	0	0
	b	0	0	0	0	0.1	0
	c	0	0	0	0	0	0.1

Table 8. RW V&V test three initial conditions

		RW Inertial Force (N)			RW Inertial Moment (N-m)		
		x	y	z	x	y	z
Test 3	a	0.1	0	0	0	0	0
	b	0	0.1	0	0	0	0
	c	0	0	0.1	0	0	0

Table 9. RW V&V test three results

The final test involved linear acceleration along all three RW axes. The results all showed an inertial force with the appropriate magnitude in the appropriate direction.

b. RW Transverse Reaction Verification

The reaction verification is broken up into two parts: analyzing an applied inertial transverse force and an applied inertial transverse moment. Both the moment and force are applied to act on the center of mass (COM). Each part is then subdivided into four sections. The first section analyzes the effect of moving the COM from one bearing to the other, along the length of the shaft. The second section analyzes the effect of shaft length. Both sections are performed for both the cantilever and fixed-fixed end condition cases. The RW is assumed to have the same physical properties as described in the inertial motion verification. Additionally, the nominal shaft length is one meter and the nominal COM location is at the midpoint of the shaft. The applied force has a magnitude of 1 N and the applied moment has a magnitude of 1 N-m. These values were chosen to generate plots whose relationships could be scaled to fit the scale of the MED array being analyzed.

Figure 49 through Figure 52 give the transverse force case with Figure 48 giving the direction of the applied force. In accordance with the convention described in Chapter V Section B, bearing one is at the bottom of the RW and bearing two is at the top.

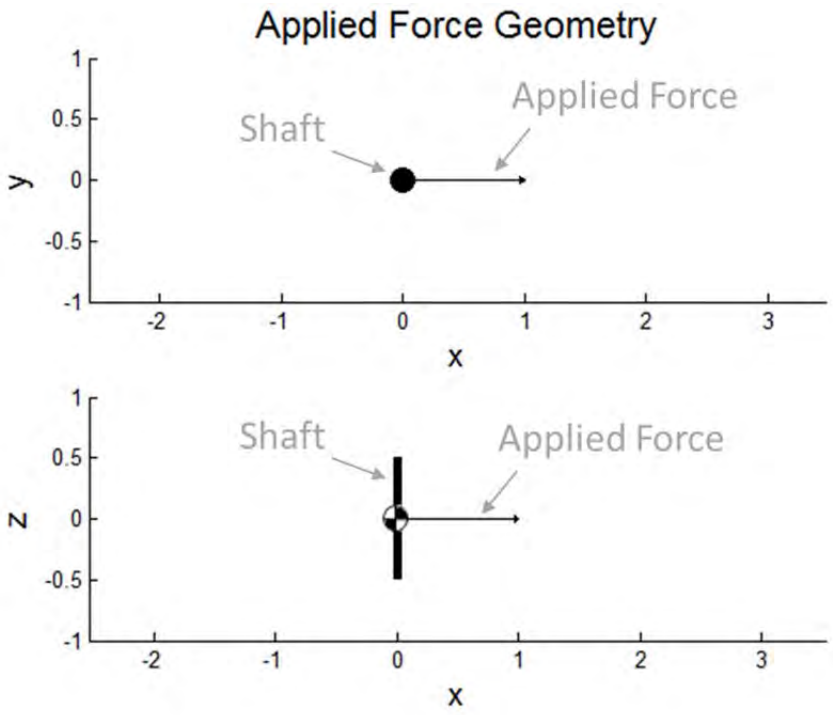

Figure 48. Applied inertial force geometry for RW reaction validation

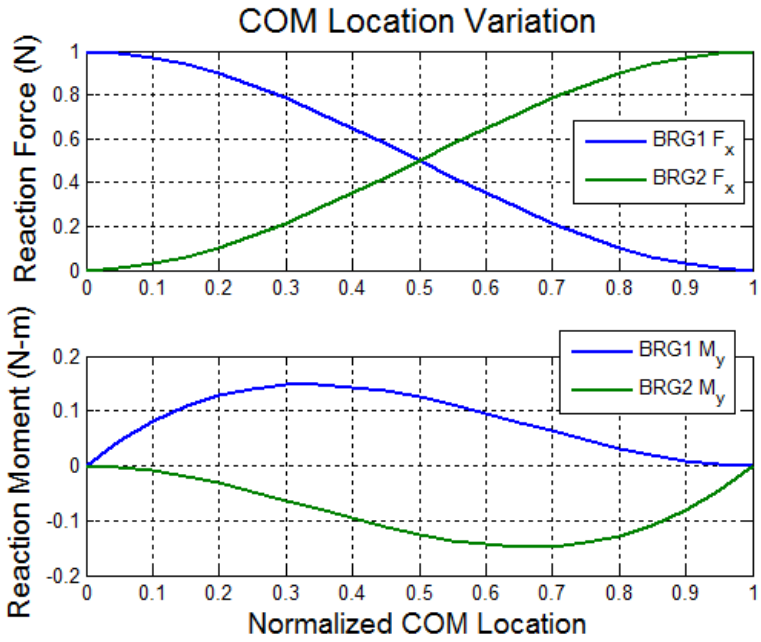

Figure 49. Fixed-fixed RW COM variation reaction validation for an applied inertial force at the center of the shaft

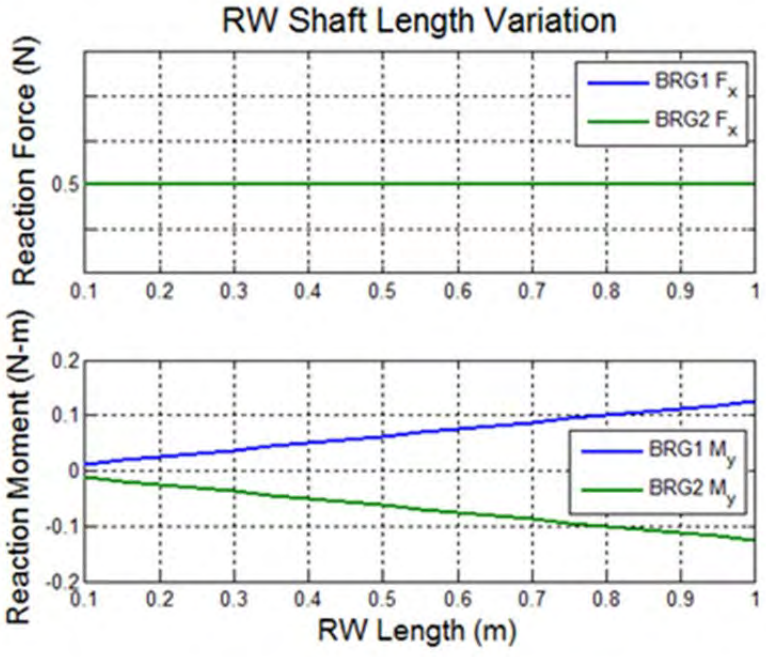

Figure 50. Fixed-fixed RW shaft length variation reaction validation for an applied inertial force at the center of the shaft

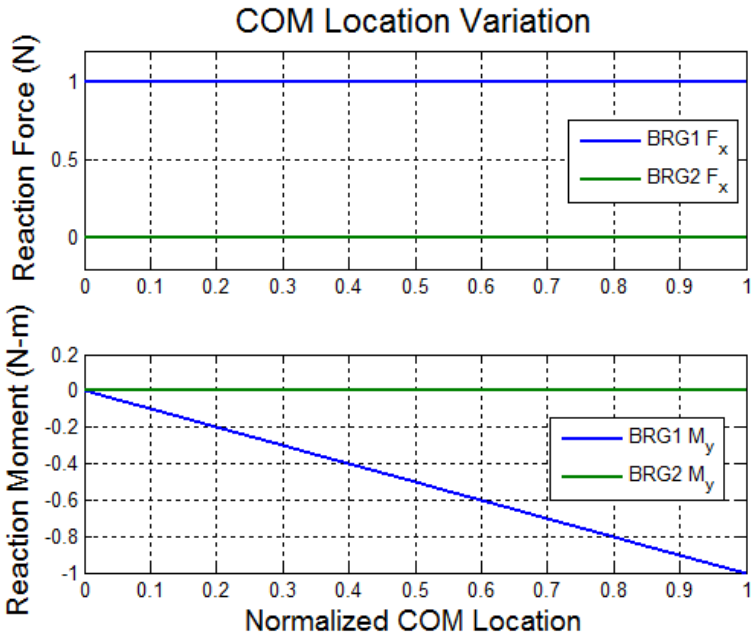

Figure 51. Cantilever RW COM variation reaction validation for an applied inertial force at the center of the shaft

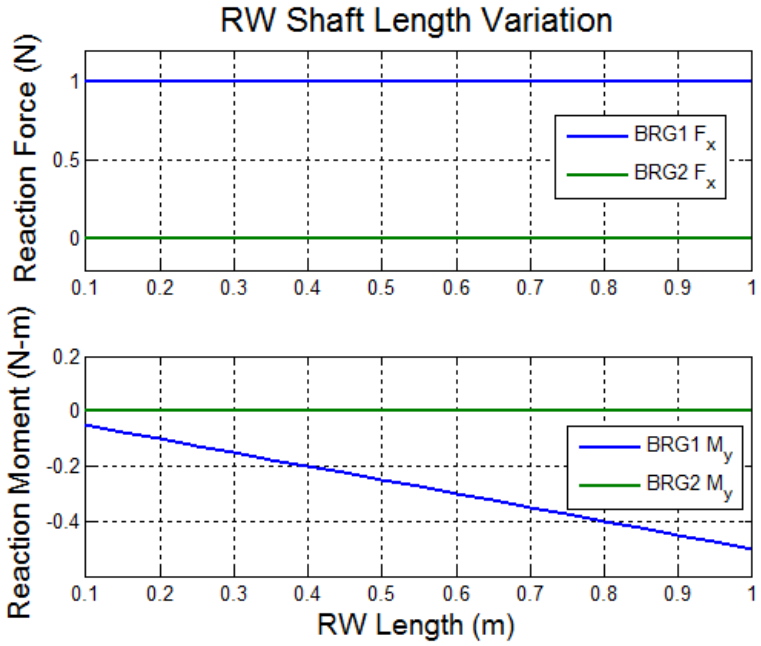

Figure 52. Cantilever RW shaft length variation reaction validation for an applied inertial force at the center of the shaft

For both the fixed-fixed and cantilever cases, the reaction forces and moments behave as expected with respect to the geometrical variations.

Figure 53 shows the geometry for the applied moment section, with Figure 54 to Figure 57 giving the results.

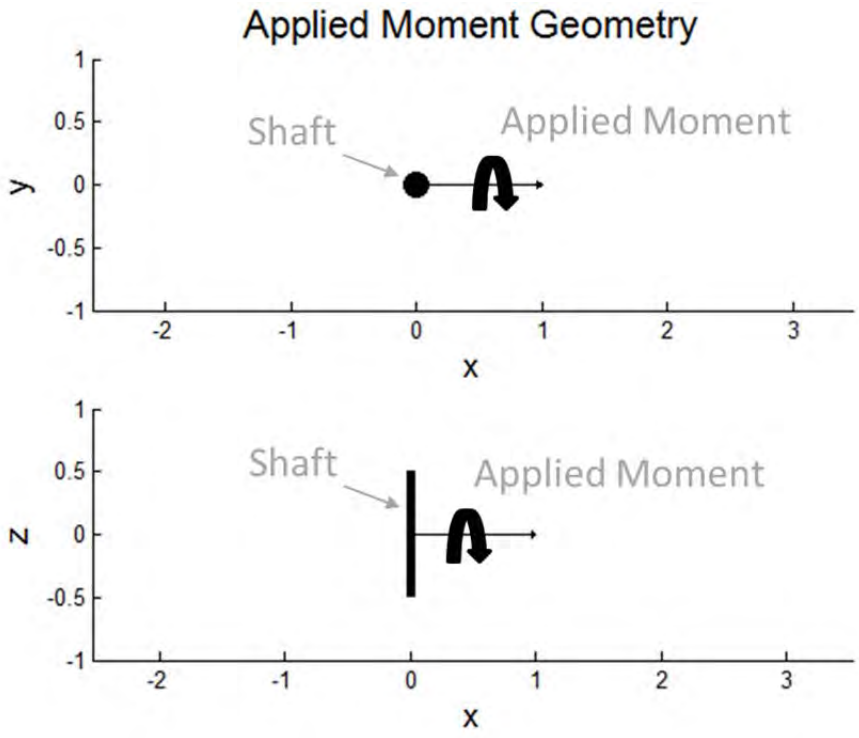

Figure 53. Applied inertial moment geometry for RW reaction validation

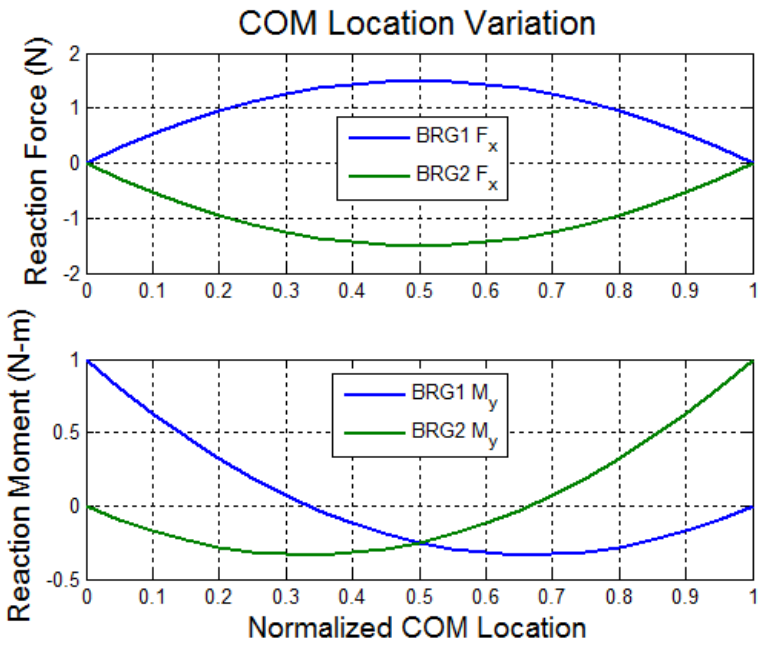

Figure 54. Fixed-fixed RW COM variation reaction validation for an applied inertial moment at the midpoint of the shaft

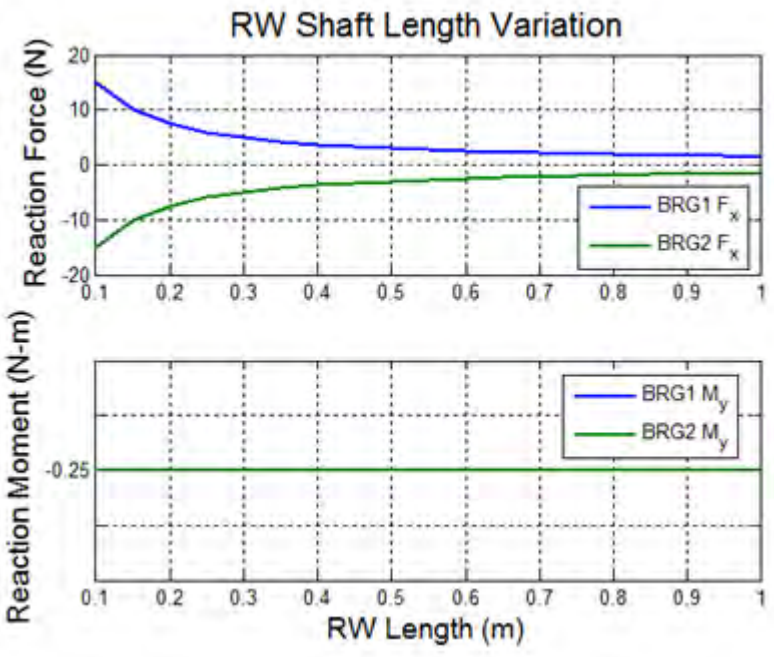

Figure 55. Fixed-fixed RW shaft length variation reaction validation for an applied inertial moment at the midpoint of the shaft

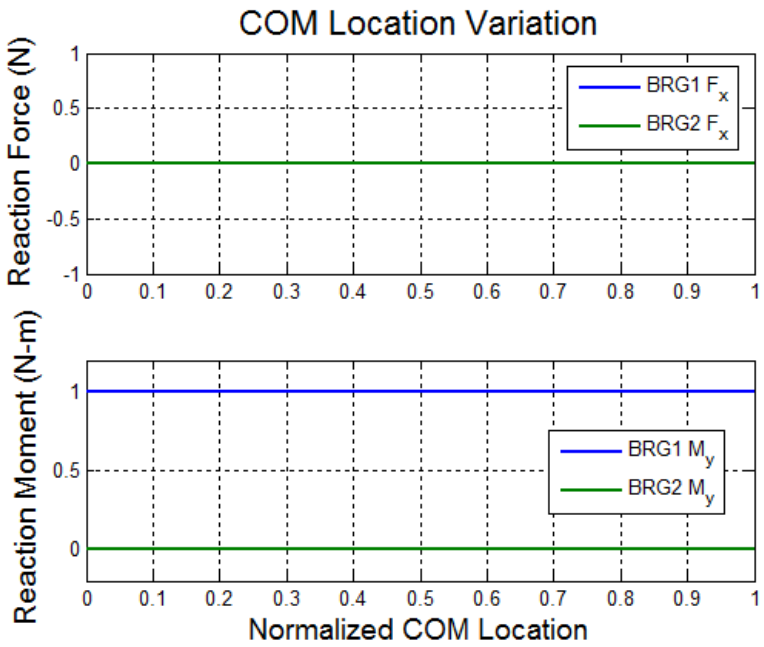

Figure 56. Cantilever RW COM variation reaction validation for an applied inertial moment at the midpoint of the shaft

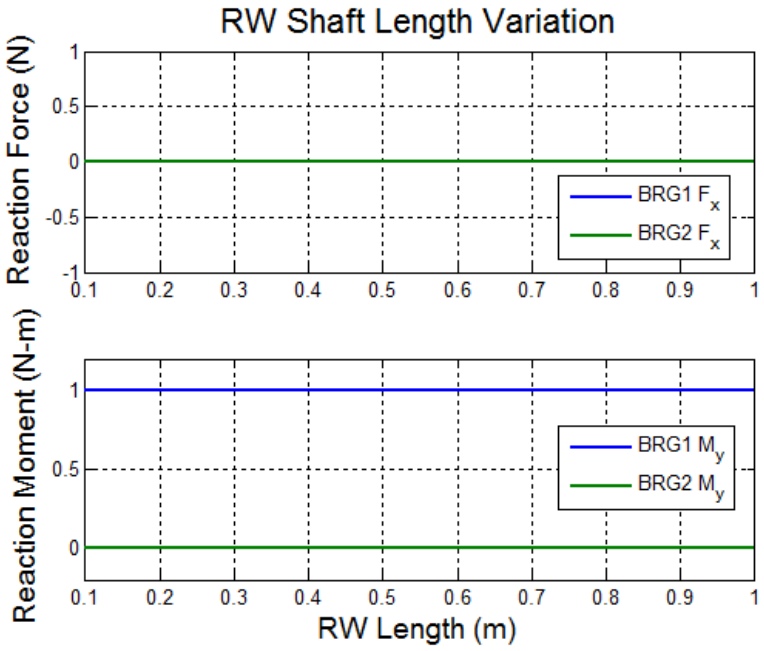

Figure 57. Cantilever RW shaft length variation reaction validation for an applied inertial moment at the midpoint of the shaft

All reaction forces and moments acted as expected through this analysis, which validate the application of the beam tables.

c. Reaction Wheel Axial Reaction Verification

Due to the assumed construction of the fixed-fixed system, bearing one supports all axial force and moment loads. This matches the reaction of the cantilever system. Since Equations (71) and (81) explicitly enforce this property, additional analysis is not required.

d. CMG Inertial Motion Verification

As the inertial motion of the gimbal frame follows the same kinematics as the RW frame, the prior analysis sufficiently proves the equations used. The rotor frame, however, has the added complexity of gimbal motion and so must be analyzed.

Due to the complexity of the resulting inertial forces and moments on the rotor from combined gimbal and spacecraft rotations, the utility of performing as exhaustive an analysis as was performed on the RW equations is limited. Therefore, two specific rotor cases will be examined: motion by the gimbal only and motion by the gimbal with counter-motion by the spacecraft (similar to test 1.c for the RW). The mechanical properties of the rotor will match those of the RW, the origin of the gimbal frame will be coincident with the origin of the spacecraft body frame, and the gimbal rotation axis will be parallel to the Z-axis of the spacecraft body. All bodies will start at rest. Table 10 gives the specific conditions of the test.

				Applied Ang. Accel. (rad/sec^2)			
	Rotor COM Location (m)			S/C			Gimbal
	X_G	Y_G	Z_G	x	y	z	$\ddot{\delta}$
Test 1	0	0	0	0	0	0	0.1
Test 2	0	0	0	0	0	-0.1	0.1

Table 10. CMG V&V initial conditions

Figure 58 and Figure 59 give the results of the tests. The small constant positive inertial force in the y direction in test one is caused by the angular acceleration of the gimbal. The decreasing force in the negative x direction represents the centrifugal force caused by the actual rotation of the gimbal. As the gimbal rate increases, the magnitude of the force increases as seen in Equation (106).

$$
\begin{aligned}
{}^{N}a_r &= {}^{N}\not{a}_g + {}^{N}_{b}R\left(\left[\underset{\sim}{\not{\alpha}}^{b/N}\right]+\left[\underset{\sim}{\not{\omega}}^{b/N}\right]\left[\underset{\sim}{\not{\omega}}^{b/N}\right]\right){}^{b}_{g}R\,{}^{g}r_r \\
&\quad +2\,{}^{N}_{b}R\left[\underset{\sim}{\not{\omega}}^{b/N}\right]{}^{b}_{g}R\left[\underset{\sim}{\omega}^{g/b}\right]{}^{g}r_r + {}^{N}_{b}R\,{}^{b}_{g}R\left(\left[\underset{\sim}{\alpha}^{g/b}\right]+\left[\underset{\sim}{\omega}^{g/b}\right]\left[\underset{\sim}{\omega}^{g/b}\right]\right){}^{g}r_r \qquad (106) \\
{}^{N}a_r &= {}^{N}_{b}R\,{}^{b}_{g}R\left(\left[\underset{\sim}{\alpha}^{g/b}\right]+\left[\underset{\sim}{\omega}^{g/b}\right]\left[\underset{\sim}{\omega}^{g/b}\right]\right){}^{g}r_r
\end{aligned}
$$

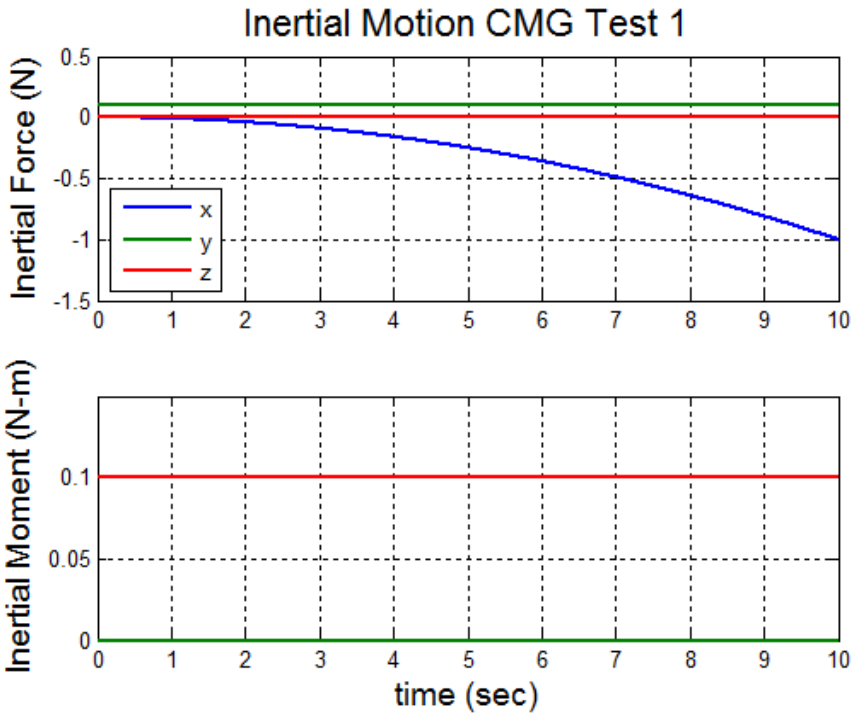

Figure 58. Results of the first CMG V&V test

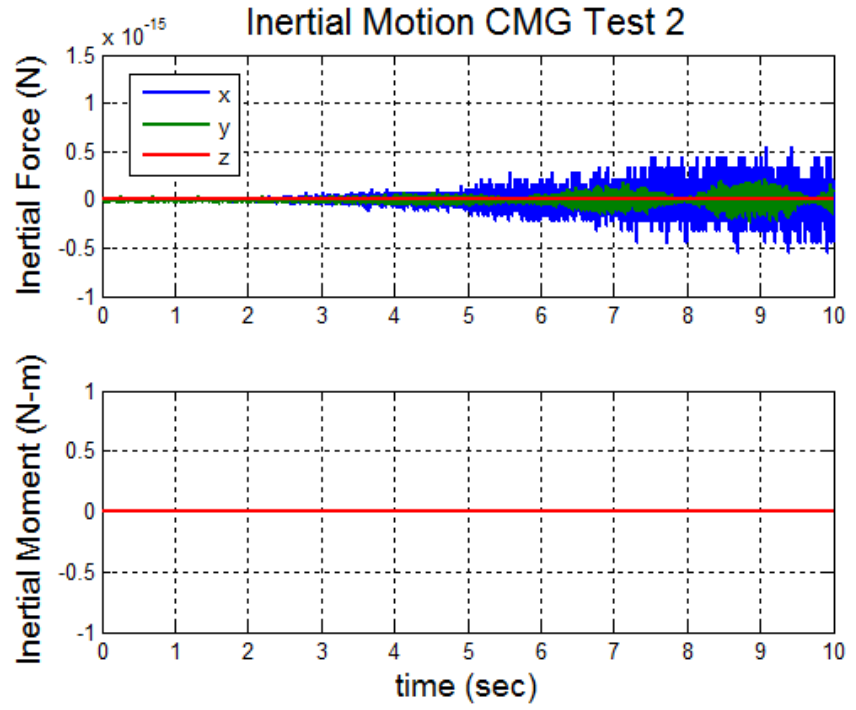

Figure 59. Results of the second CMG V&V test

For the second test, the prominent feature is the noise in the inertial force plot. Though of a negligible magnitude, it likely appears due to several adverse factors including the rudimentary simulation method and relatively rapidly rotating bodies. The important feature is the fact that the counter-spinning bodies remove the inertial moment from the rotor as it now appears to stand still in the inertial frame.

2. Reaction Wheel Maneuvers

The spacecraft geometry for the RW analysis is given in Figure 60 and tabulated in Table 11. The maneuver is an arbitrary rest to rest slew from one orientation to another. The analyzed telemetry data includes only the spacecraft quaternions and body rates, the RW angular acceleration and an array of the time steps.

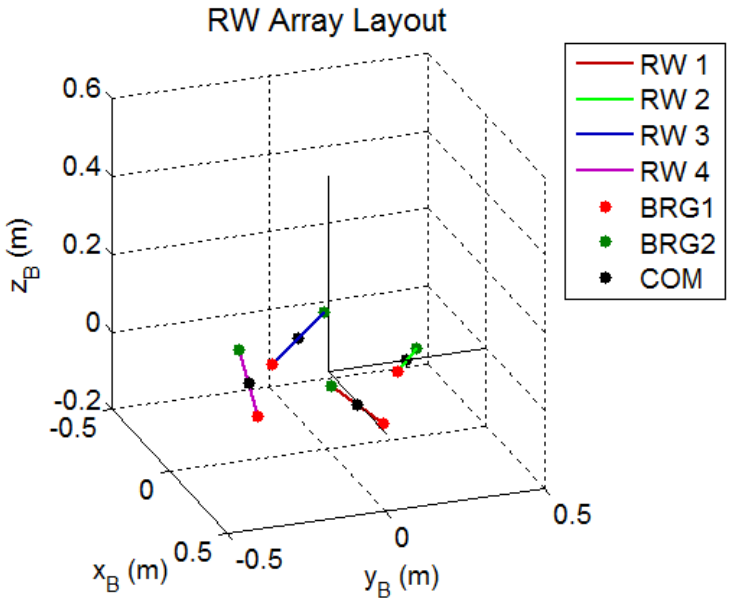

Figure 60. Geometry detail for the RW maneuver force and moment analysis

RW	γ (deg)	β (deg)	COM ($X_b/Y_b/Z_b$) (m)		
1	0	54.73	0.25	0	0
2	90	54.73	0	0.25	0
3	180	54.73	-0.25	0	0
4	270	54.73	0	-0.25	0

Table 11. Tabulated values for RW array layout for maneuver analysis

The RWs used in the analysis have the same properties as those used in the momentum space case study. Telemetry was derived from the model developed in [4].

a. Eigenaxis Maneuver

The first maneuver is based on an eigenaxis controller where the eigenaxis between the initial and final state is calculated and a torque command is developed to rotate the spacecraft about this axis. Figure 61 describes the basic telemetry for the maneuver.

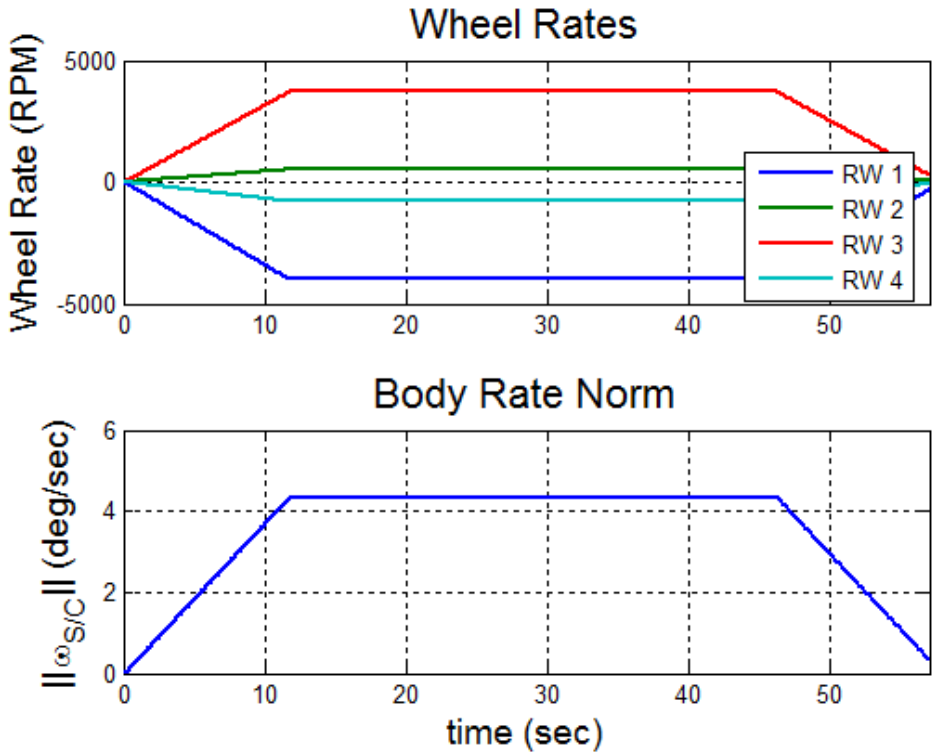

Figure 61. Eigenaxis slew maneuver for RW array force and moment analysis

During the maneuver, the first and third RW saturate at +/- 4000 RPM to achieve a constant spacecraft body rate magnitude of slightly above 4 deg/sec about the eigenaxis. The calculated inertial force and moment magnitudes are given in Figure 62 and Figure 63.

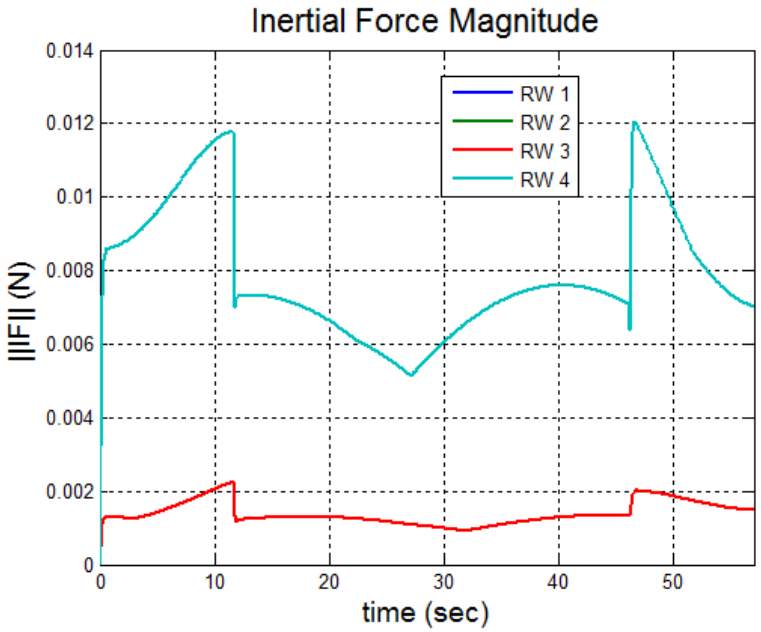

Figure 62. Inertial force magnitudes during an eigenaxis slew maneuver

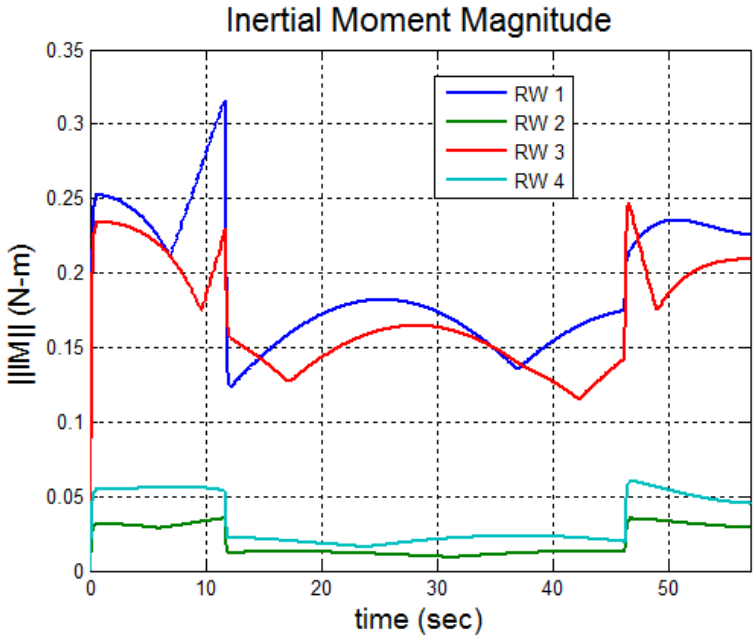

Figure 63. Inertial moment magnitudes during an eigenaxis slew maneuver

During this maneuver, the magnitudes of the inertial forces are equal for opposite pairs of RWs (one

and three, two and four). This matches expectations as the RWs lie equidistant along a common axis from the spacecraft body origin which is the point about which the spacecraft rotates. Thus, one would expect the centrifugal force on the RWs to be equal in magnitude and opposite in direction. The difference in magnitude between the two pairs indicates that RWs two and four are moving faster through inertial space, indicating that the projection of the eigenaxis along the line connecting RW two and RW four is larger than the projection on the line connecting the other set. This assumption is borne out by the magnitude of the inertial moments. Since the spacecraft is spinning about an axis that is closer to the rotation axis of RW one and three, they will have a larger inertial moment induced on them.

The steps seen at about 12 seconds and 46 seconds indicate the times when the RW angular acceleration goes from non-zero to zero (and vice-versa).

The reaction force plots for the fixed-fixed configuration given in Figure 64 and Figure 65 show an interesting property. The inertial moments are between one and two orders of magnitude larger than the forces. From Figure 54, a one meter shaft results in reaction forces about 1.5 times larger than the applied moment. Furthermore, Figure 55 shows that a 0.2 m shaft, the assumption used for this analysis, results in reaction forces eight times larger than the applied moment. The inertial moment, therefore, contributes most to the reaction force at the bearings.

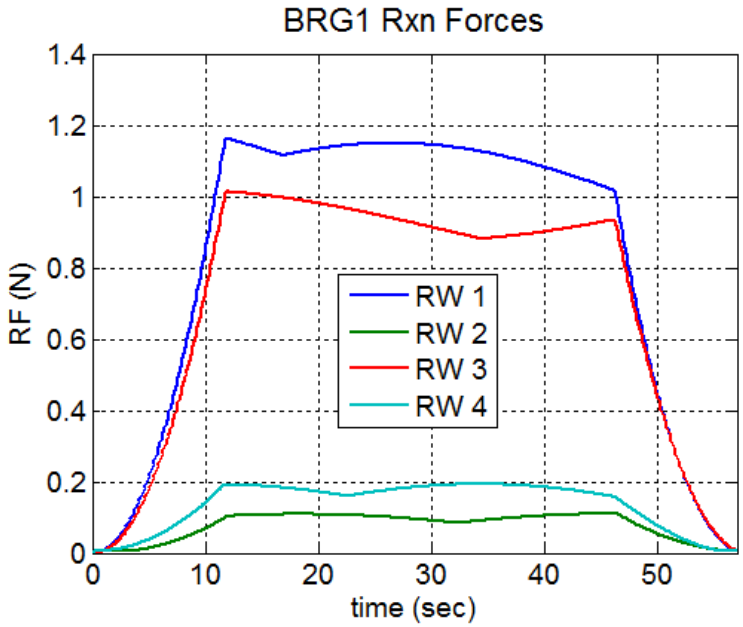

Figure 64. Bearing one reaction force magnitudes for the eigenaxis slew, fixed-fixed configuration

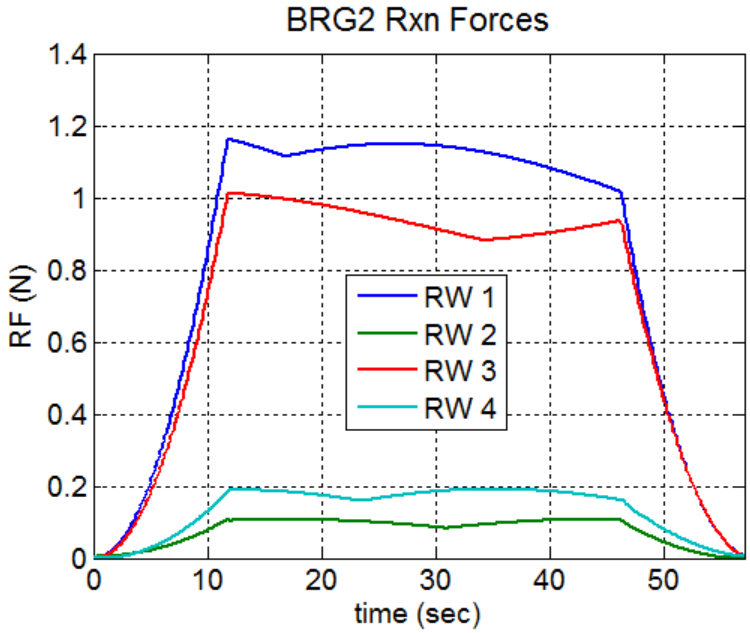

Figure 65. Bearing two reaction force magnitudes for the eigenaxis slew, fixed-fixed configuration

That fact explains why both bearings have approximately the same force magnitude, despite the fact

that bearing two does not support a force in the axial direction. When examining the reaction moments, Figure 66 and Figure 67, bearing one shows a significant larger moment than bearing two during wheel operation. This is attributed to the fact that only bearing one resists an axial moment due to the motor being co-located with bearing one. The larger reaction moment magnitude for RWs one and three stems from the fact that they are accelerating at a higher rate.

When the RWs are not accelerating, the reaction moment magnitudes on both bearings roughly match each other.

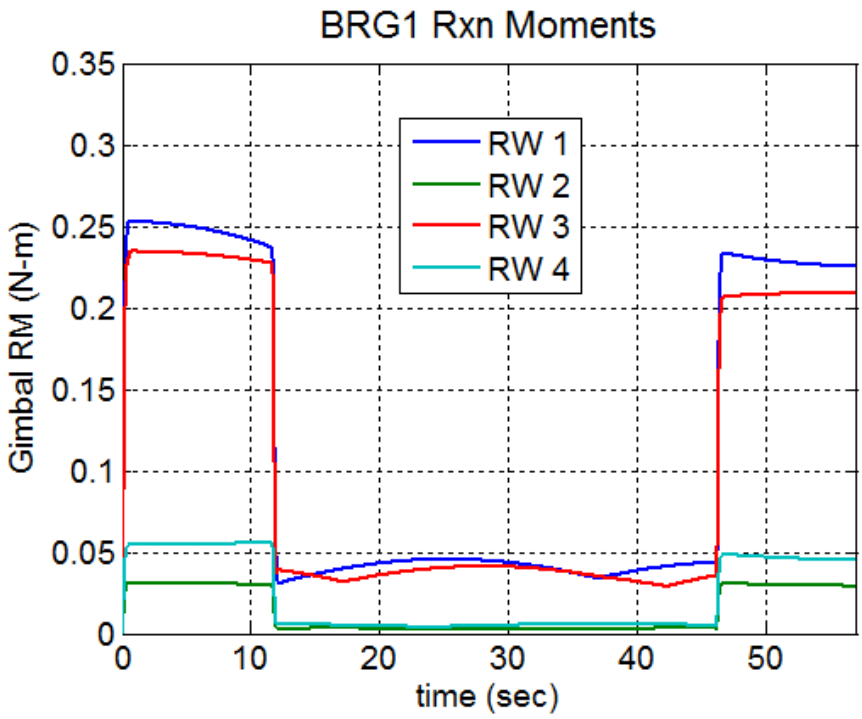

Figure 66. Bearing one reaction moment magnitudes for the eigenaxis slew, fixed-fixed configuration

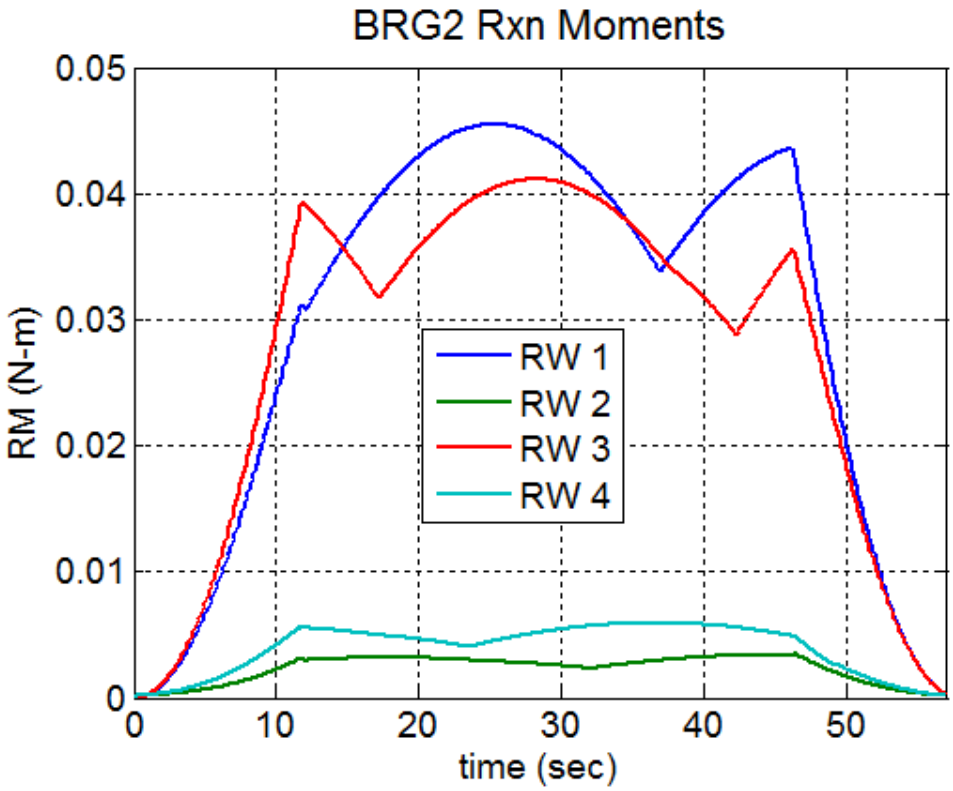

Figure 67. Bearing two reaction moment magnitudes for the eigenaxis slew, fixed-fixed configuration

With the cantilever case, the bearing one reaction forces and moments act as expected, shown in Figure 68 and Figure 69. The small inertial force magnitude and short lever arm prevent the creation of a noticeable reaction moment at the bearing, thus the reaction moment and inertial moment plots appear to match.

The magnitude of the reaction force on bearing one in the cantilever case is much less than for the fixed-fixed case because, according to the standard beam tables [13, pp. 208-223], the inertial moment does not result in a reaction force on the bearings.

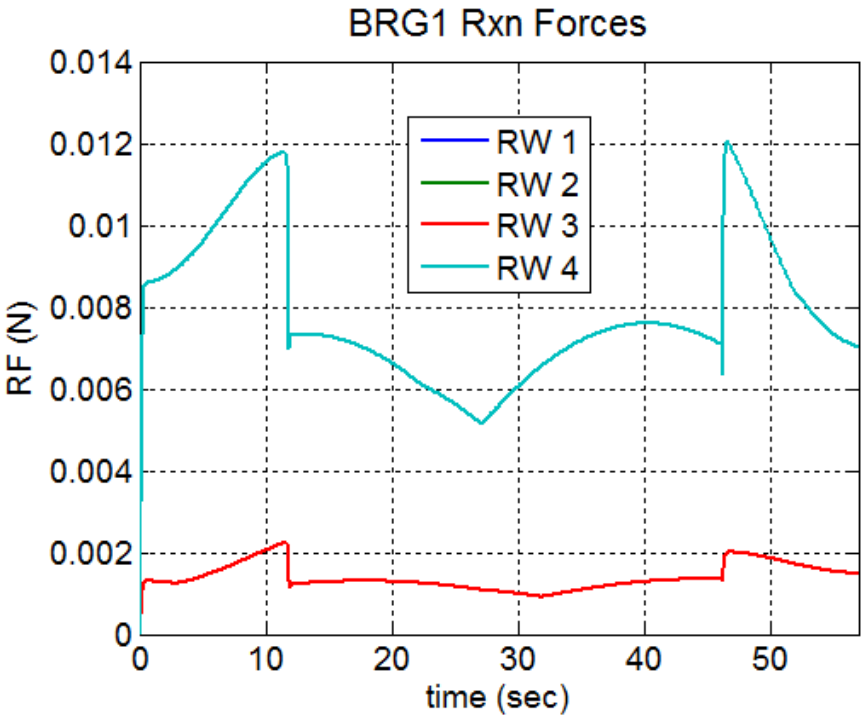

Figure 68. Bearing one reaction force magnitudes for the eigenaxis slew, cantilever configuration

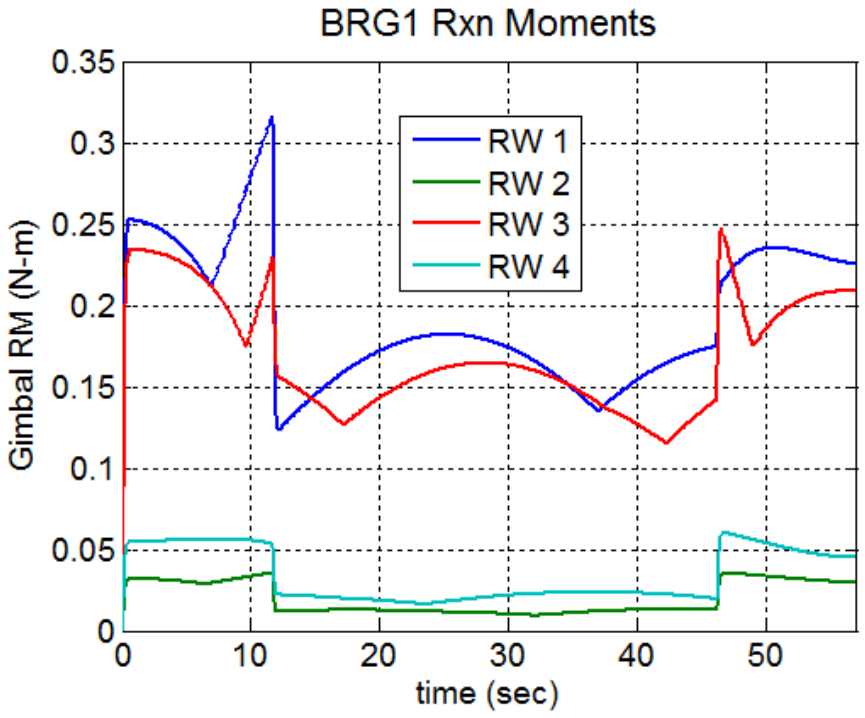

Figure 69. Bearing one reaction moment magnitudes for the eigenaxis slew, cantilever configuration

b. Optimal Maneuver

The second maneuver analyzed is an optimal maneuver where the cost function, J, represents a quantity that the controller minimizes. This cost function can include such quantities as elapsed time or wheel power. The same RW configuration is used and the telemetry is derived from the same source. The maneuver is conducted with the same initial and final conditions as before. Figure 70 shows the maneuver.

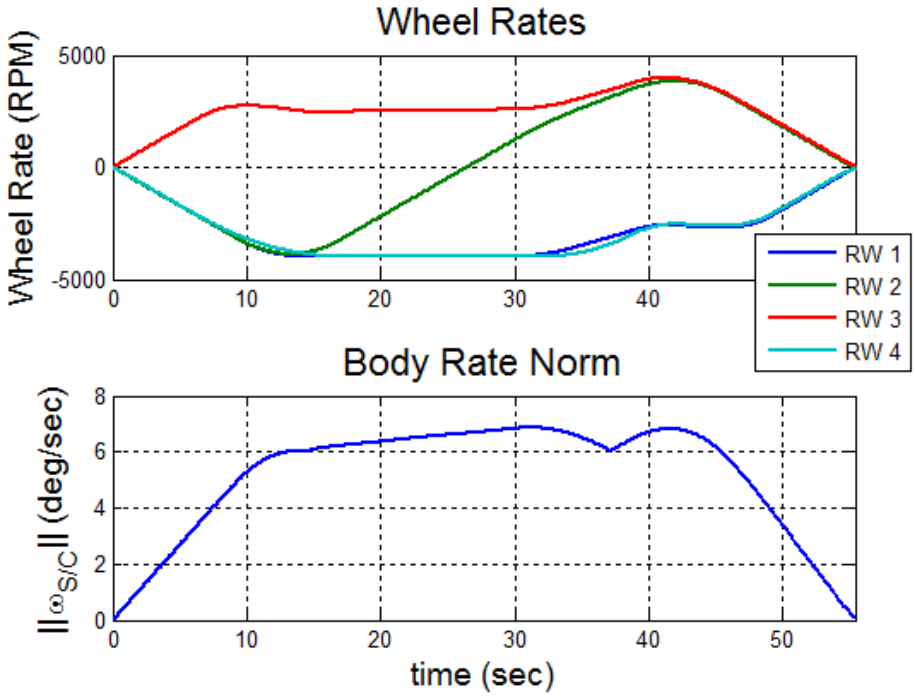

Figure 70. Optimal slew maneuver for RW array force and moment analysis

For this maneuver, the wheel rates of all wheels are now closer to or at saturation for a longer period of time. The body rate magnitude is somewhat higher throughout the maneuver, and the final state is reached slightly sooner

than the eigenaxis maneuver. This additional exercising of the RWs is typical of an optimal maneuver as the algorithm seeks to use the excess performance that is present but that the eigenaxis slew ignores.

Since there is no single axis of rotation for the maneuver and the RWs tend to continuously accelerate or decelerate, the inertial force and moment magnitudes induced on the RWs tend to be more complicated, as shown in Figure 71 and Figure 72.

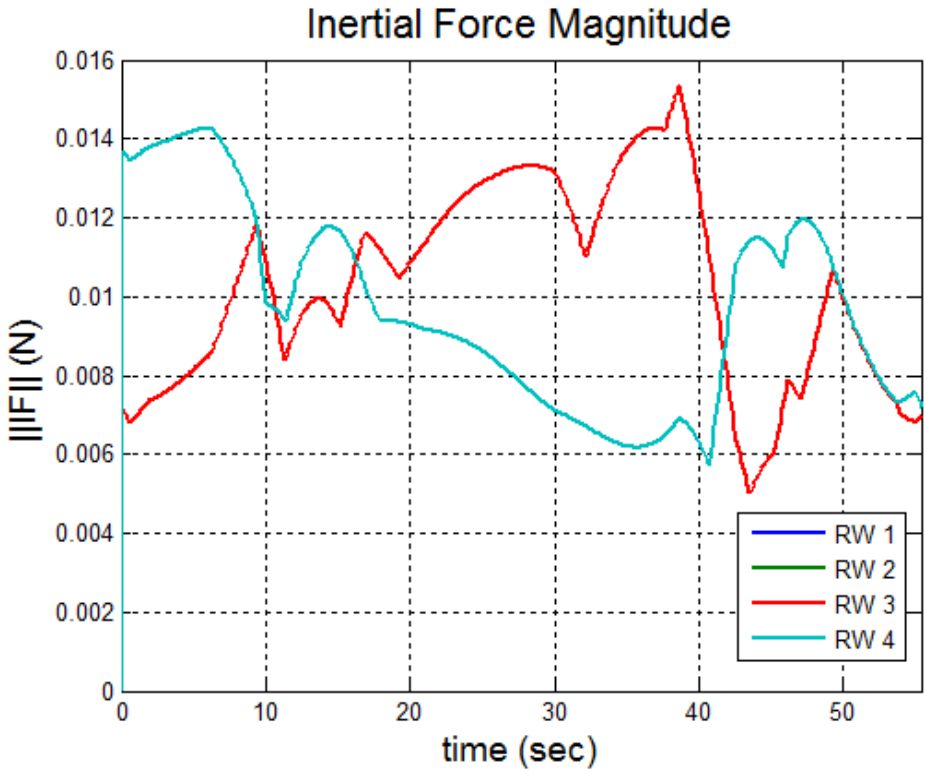

Figure 71. Inertial force magnitudes during an optimal slew maneuver

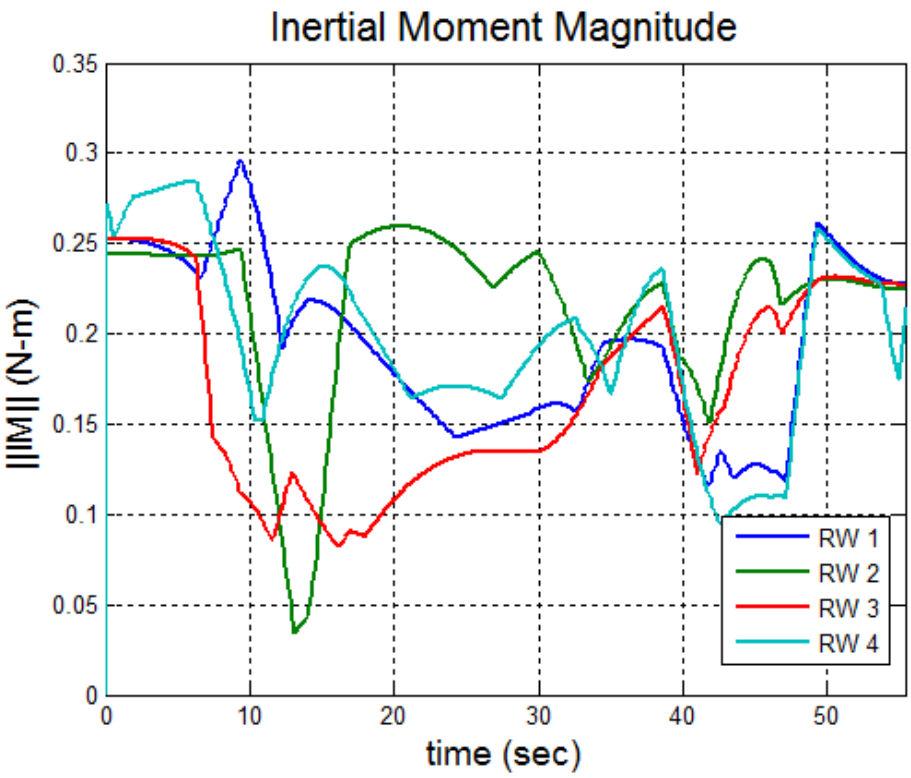

Figure 72. Inertial moment magnitudes during an optimal slew maneuver

There are some similarities between the time optimal and eigenaxis slew maneuvers with regards to the inertial forces and moments. As with the eigenaxis slew, the optimal slew produces inertial forces that are equal in magnitude to the same paired RWs: one and three, two and four. This equality is expected due to the positional symmetry in the system. Since all RWs are equidistant from the z-axis, a spacecraft body rotation about this axis produces equal inertial force in all components. RW one and three are positioned along the x-axis equidistant from the origin, so a spacecraft body rotation rate about the y-axis produces equal and opposite inertial forces in that pair, and zero inertial force in the other. The opposite is true for a spacecraft body rotation rate about the x-

axis. The inertial forces tend to be slightly larger for all four components due to the higher body rates; however they are still an order of magnitude below the inertial moments.

When analyzing the behavior of the moments, though, it is possible to determine when changes in wheel acceleration occur as these accelerations cause moments that tend to dominate. This is expected as the wheel can change acceleration much faster than the spacecraft will alter its rotational motion. Removing the torque induced by the wheel itself would produce much smoother plots, as seen during the periods of constant wheel acceleration in Figure 63.

The bearing force and moment reaction magnitudes are given in Figure 73 through Figure 76. As before, the inertial moments dominate the reaction forces, and bearing one supports much larger reaction moments than bearing two due to the actual torque produced by wheel accelerations.

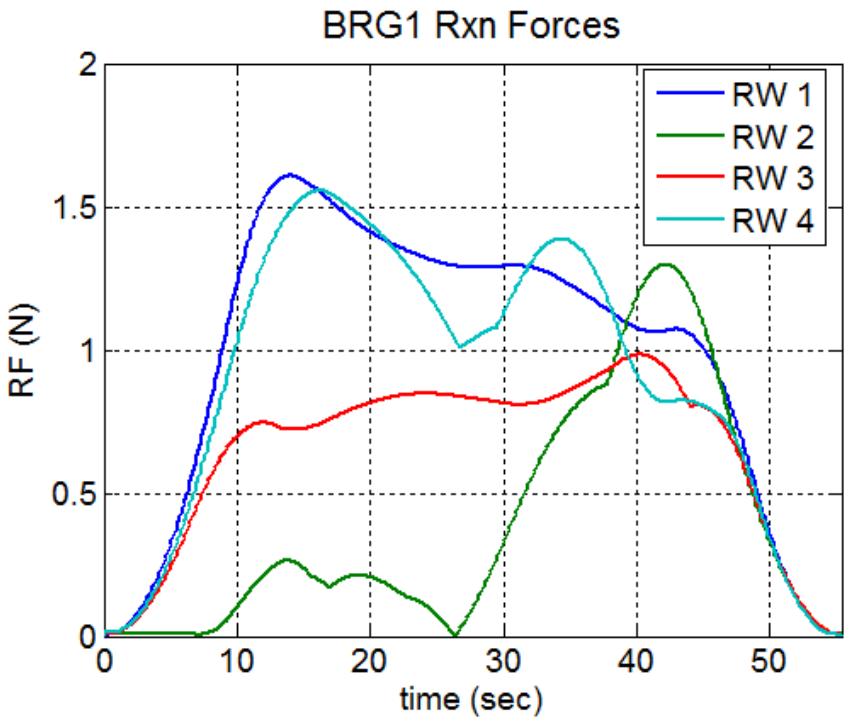

Figure 73. Bearing one reaction force magnitudes for an optimal slew, fixed-fixed configuration

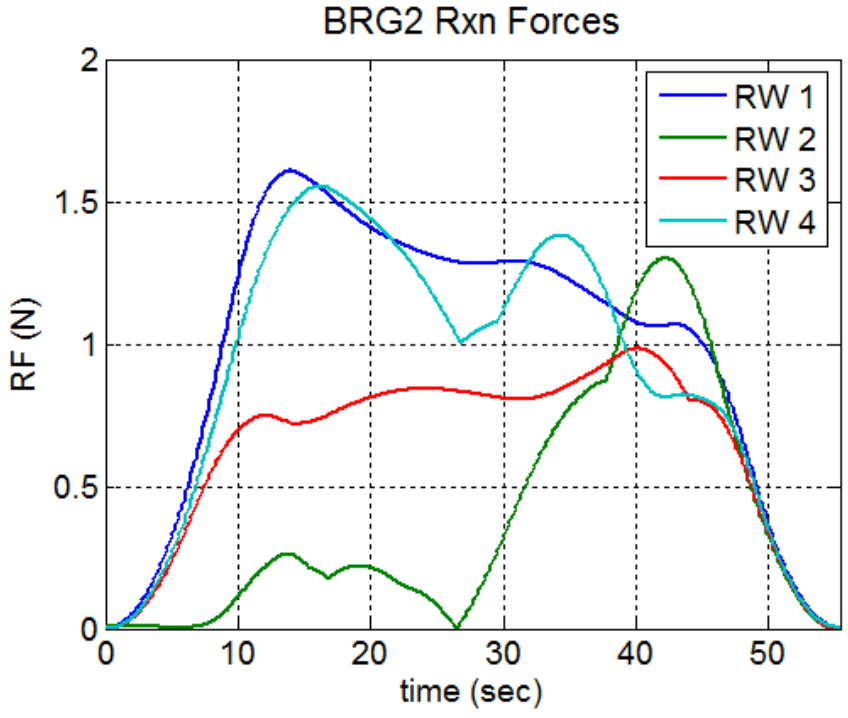

Figure 74. Bearing two reaction force magnitudes for an optimal slew, fixed-fixed configuration

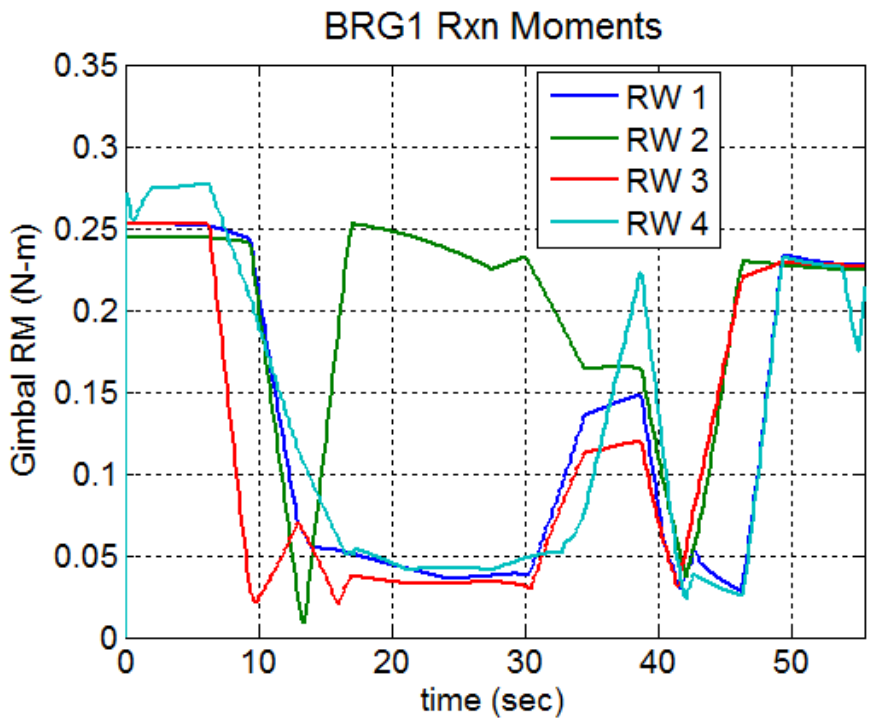

Figure 75. Bearing one reaction moment magnitudes for an optimal slew, fixed-fixed configuration

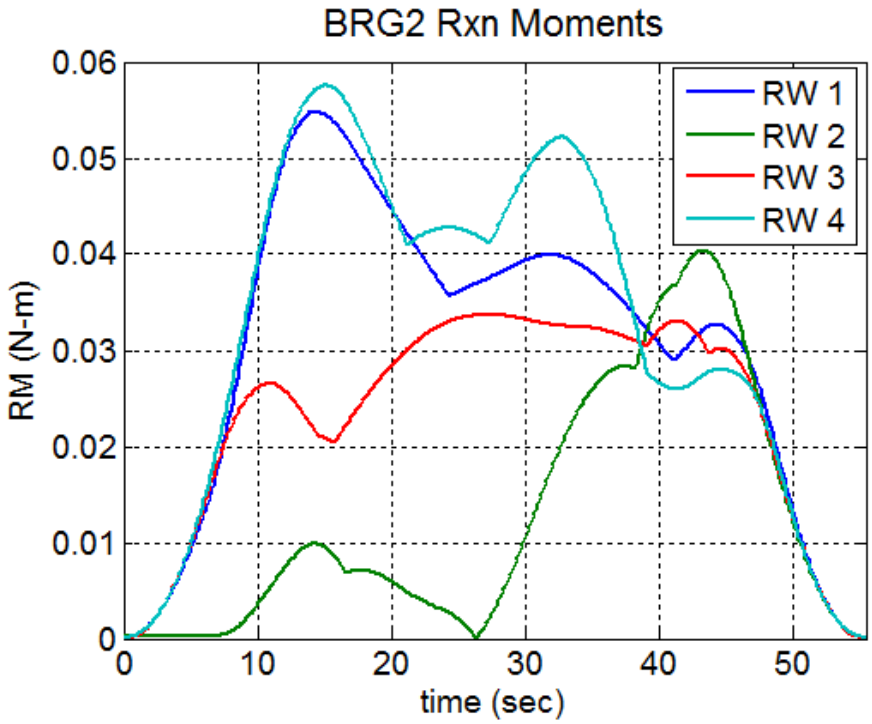

Figure 76. Bearing two reaction moment magnitudes for an optimal slew, fixed-fixed configuration

Figure 77 and Figure 78 give the cantilever results. The reaction forces and moments match the inertial forces and moments, an expected result.

Although the optimal maneuver results in more active RW utilization, the force and moment magnitudes seen by the bearings are of roughly equivalent magnitudes to those seen during the eigenaxis maneuver. Because the wheel accelerations tend to dominate the inertial moment equation (and the inertial moment dominates the inertial force with respect to bearing reactions), the optimal maneuver tends to maintain a higher average loading. This particular eigenaxis maneuver, however, produces very large and rapid changes in force and moment magnitudes due to the bang-off-bang nature of the maneuver. This shock to the system is not present in the optimal maneuver.

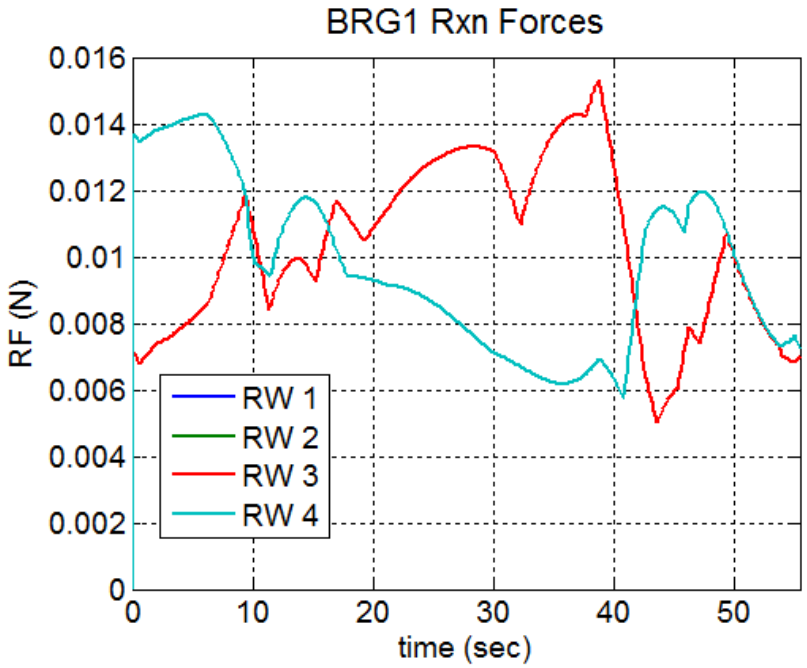

Figure 77. Bearing one reaction force magnitudes for an optimal slew, cantilever configuration

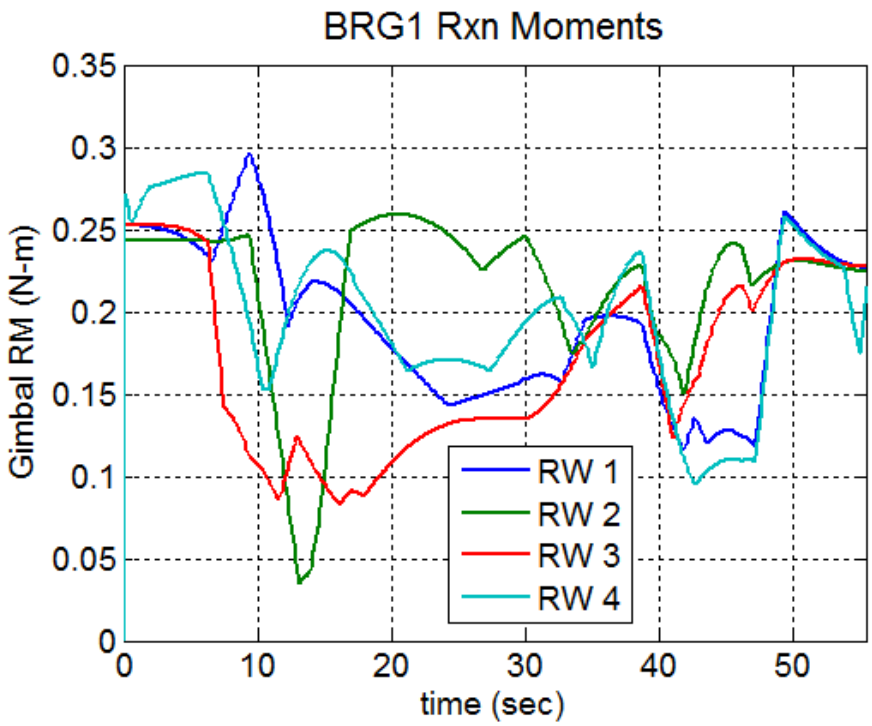

Figure 78. Bearing one reaction moment magnitudes for an optimal slew, cantilever configuration

3. CMG Maneuvers

Using four CMGs arranged in the same geometrical shape shown in Figure 60 and described in Table 11, reaction analyses for an eigenaxis slew and an optimal slew were performed. In this case, the initial and final conditions between the two maneuvers are slightly different because the telemetry data is from a higher fidelity simulation of an imaging spacecraft. The CMG mechanical properties are the same as those for the momentum and torque space analysis in Chapter VI Sections A and B with the addition that the rotor shaft length is assumed to be 0.1 m, the gimbal shaft length is assumed to be 0.5 m and bearing one for the rotor is assumed to be mounted 0.05 m from the gimbal COM in the rotor's axial direction ($x_g = x_r$). The CMG

has an assumed mass of 2 kg. The assumed rotor inertia tensor is:

$$I_{RW} = \begin{bmatrix} .0429 & 0 & 0 \\ 0 & .0429 & 0 \\ 0 & 0 & .0025 \end{bmatrix} kg \cdot m^2 \ .$$

Although there are four possible variations for the gimbal and rotor end point conditions, only the fixed-fixed/fixed-fixed case will be examined as it provides sufficient detail for this analysis. A more rigorous examination would be warranted in other cases such as actual satellite or CMG mechanism design.

a. Eigenaxis Maneuver

The analyzed maneuver is actually the end of one maneuver and the beginning of another. Due to the nature of the data, representing an entire maneuver is impractical due to the length of time involved. Analyzing the impulses between two maneuvers reduces the amount of time to be analyzed while still examining two major control events.

Initially the spacecraft is rotating at a small rate. The CMGs are gimbaled to reduce the body rate for a few seconds. They are then gimbaled again to induce a new spacecraft body rate. Figure 79 through Figure 85 give the maneuver telemetry and results of the force analysis. The large force of 36 N seen at 41 and 45 seconds in the first gimbal bearing is caused by the inertial moment induced on the rotor at those times. Due to the complexity of the system dynamics, this result cannot be easily gleaned from the analysis of the equations of motion as was done in Equation (106).

Due to the short length of the rotor shaft, the reaction forces are many times larger than the inertial moment would imply. The reaction force at the rotor bearing one is then transmitted to the gimbal in the axial direction. Since the second gimbal bearing does not support forces in this direction, the entire load is taken up by the first bearing (or more specifically, the gimbaling motor located at that bearing).

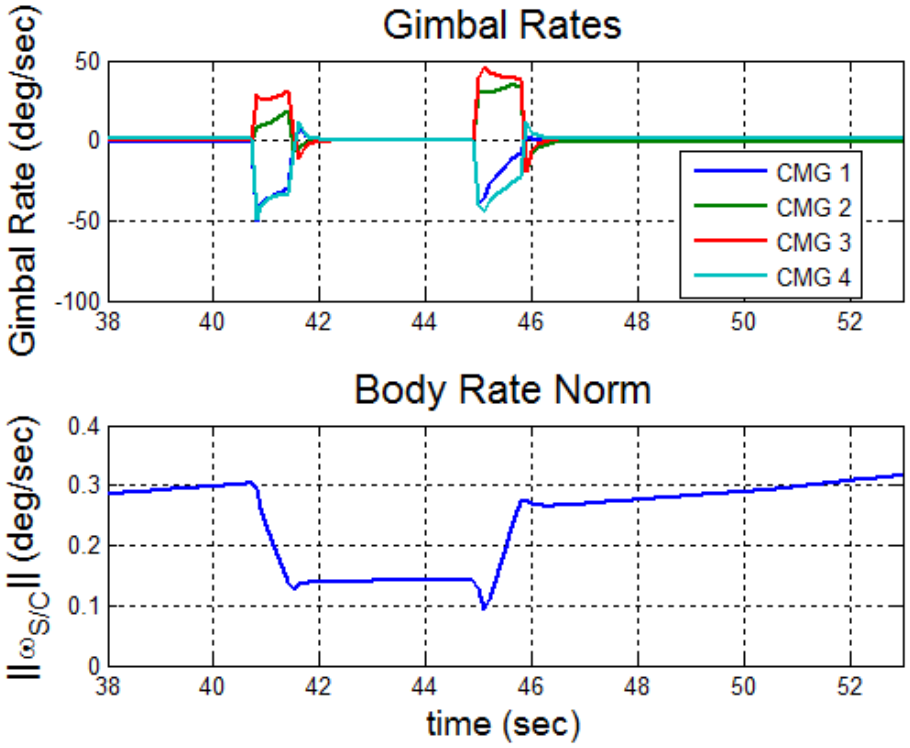

Figure 79. Eigenaxis slew telemetry for CMG force analysis

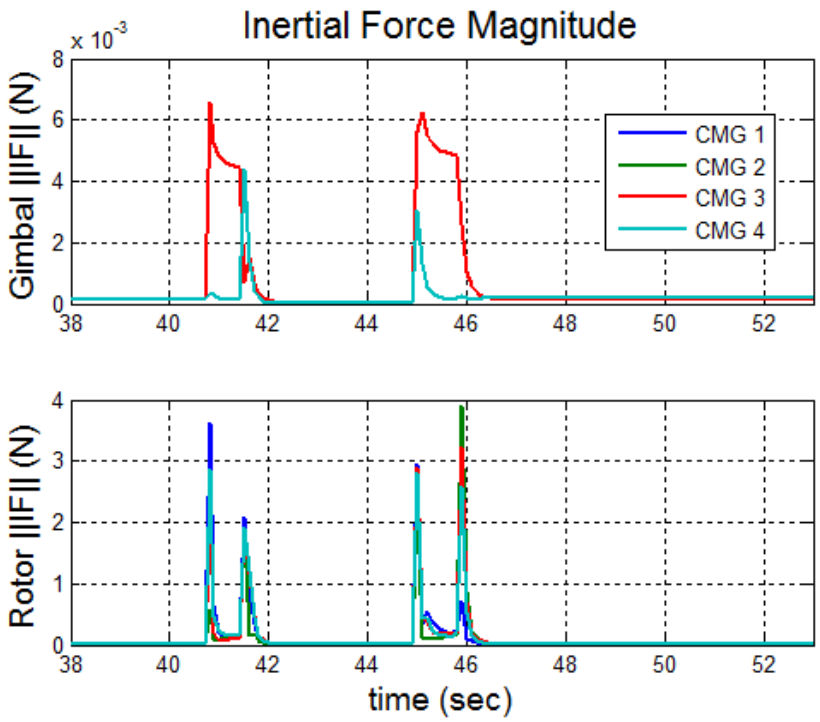

Figure 80. Inertial forces from the CMG force analysis eigenaxis slew

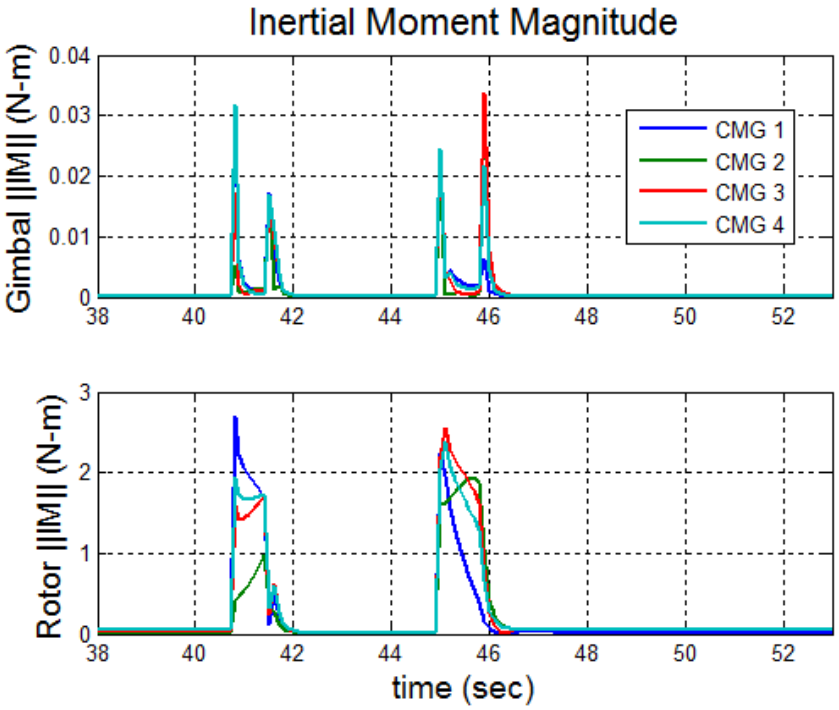

Figure 81. Inertial moments from the CMG force analysis eigenaxis slew

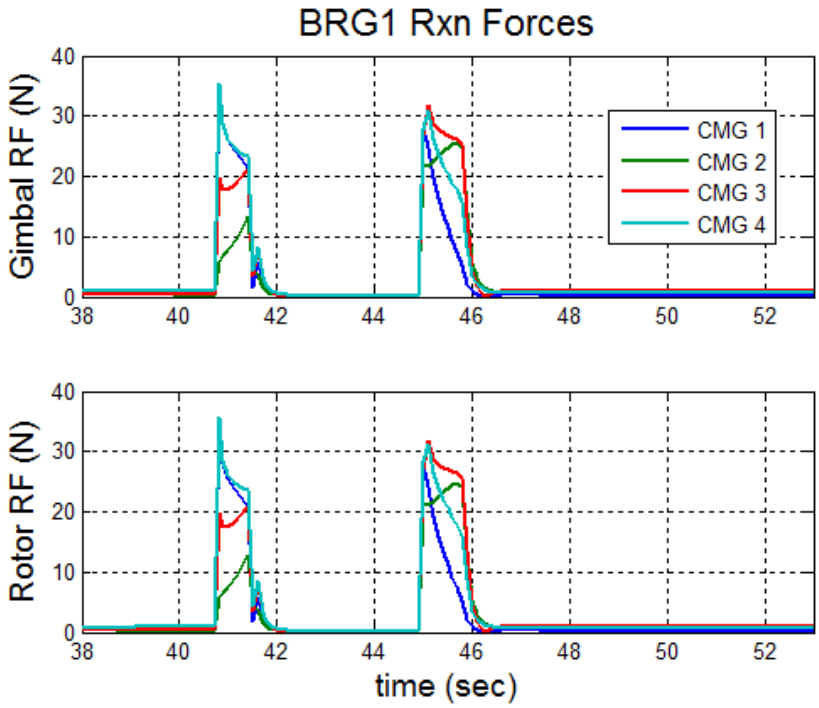

Figure 82. Bearing one reaction force magnitudes from the eigenaxis slew

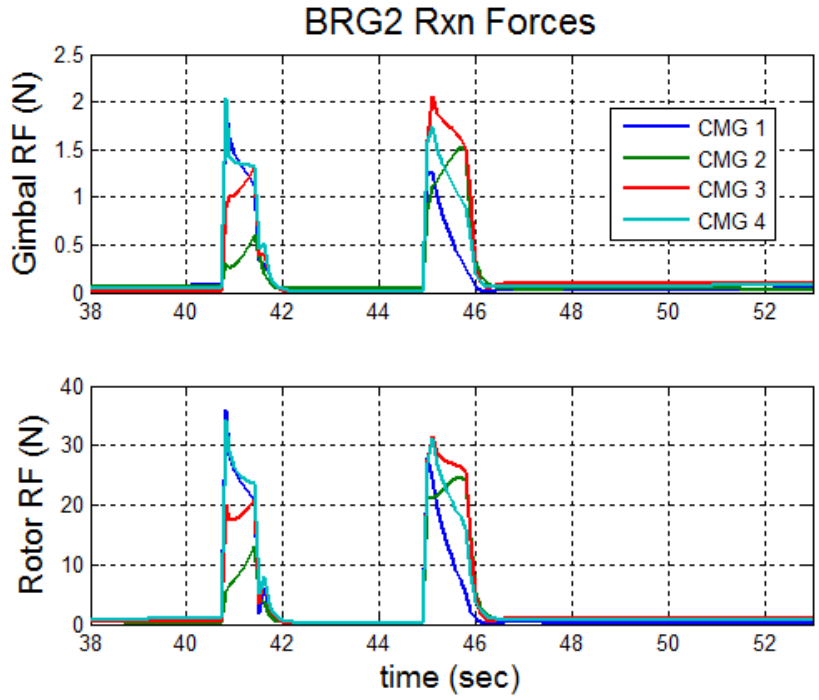

Figure 83. Bearing two reaction force magnitudes from the eigenaxis slew

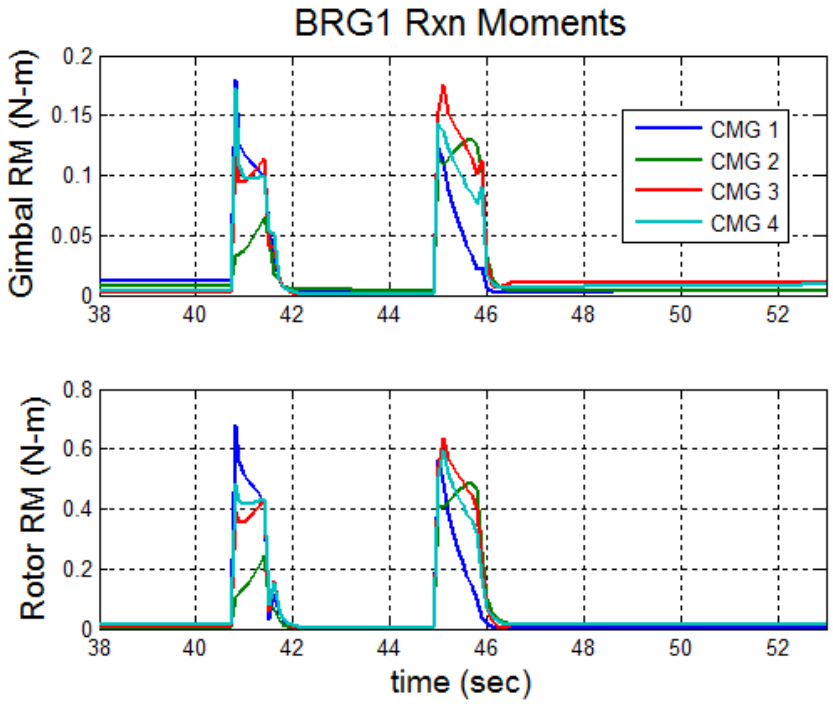

Figure 84. Bearing one reaction moment magnitudes from the eigenaxis slew

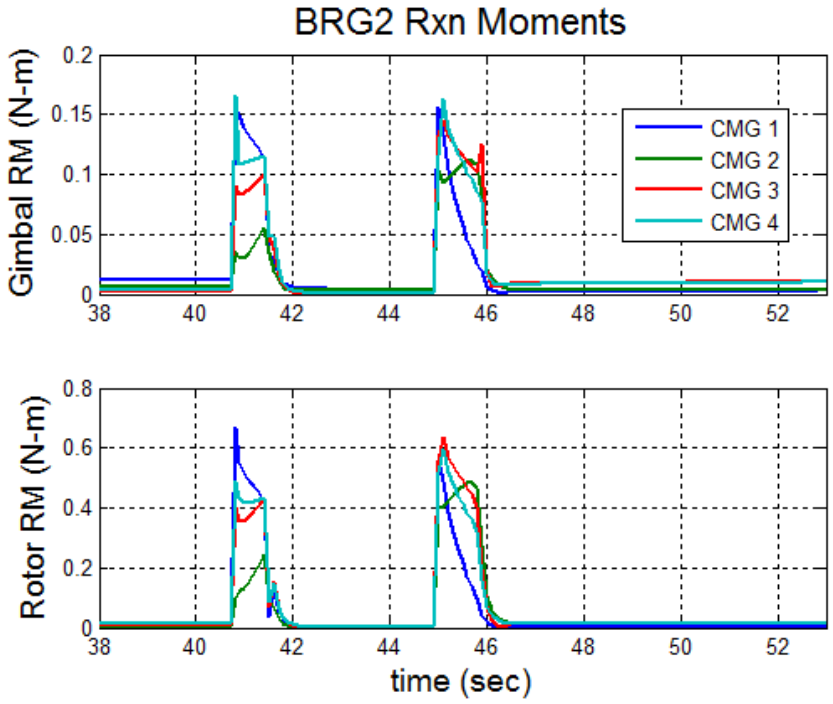

Figure 85. Bearing two reaction moment magnitudes from the eigenaxis slew

Although the maneuvers between the RW and CMG analyses are very different, it appears that a CMG has the potential to induce much larger forces on its bearings compared to a RW. This is also how the CMG provides large torques to the spacecraft. Thus, the bearings for a CMG must be built to withstand larger loads than those for a comparably sized RW.

b. Optimal Maneuver

Similar to the eigenaxis maneuver, the optimal maneuver shows the completion and commencement of two back-to-back slews. The gimbal accelerations are not as excessive in this case which slightly reduces the induced rotor inertial moment. This, in turn, reduces the large reaction force seen at the gimbal/rotor junction and the first gimbal bearing. The results are given in Figure 86 through Figure 92.

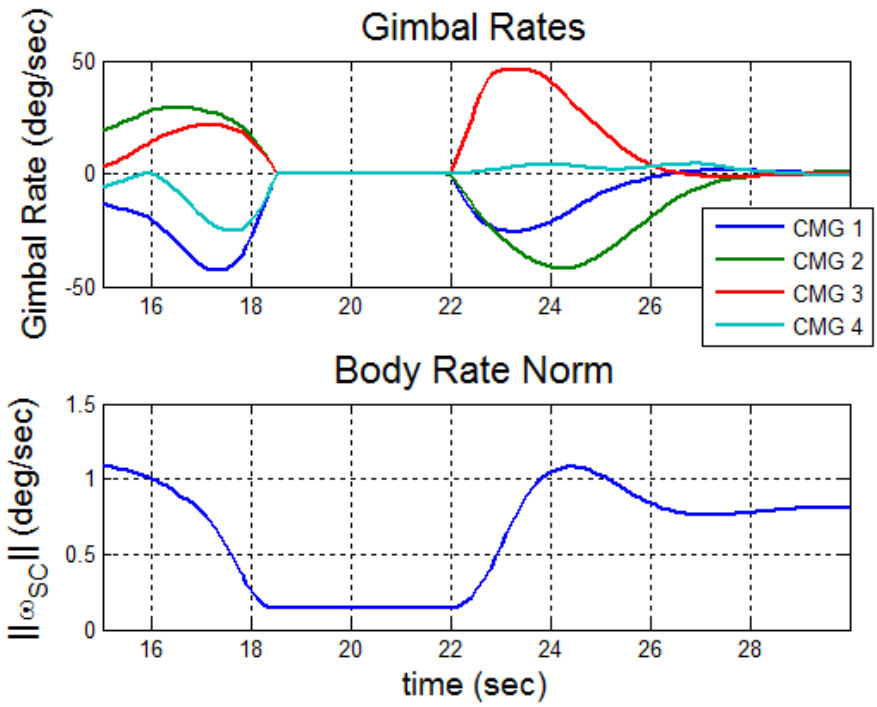

Figure 86. Optimal slew telemetry for CMG force analysis

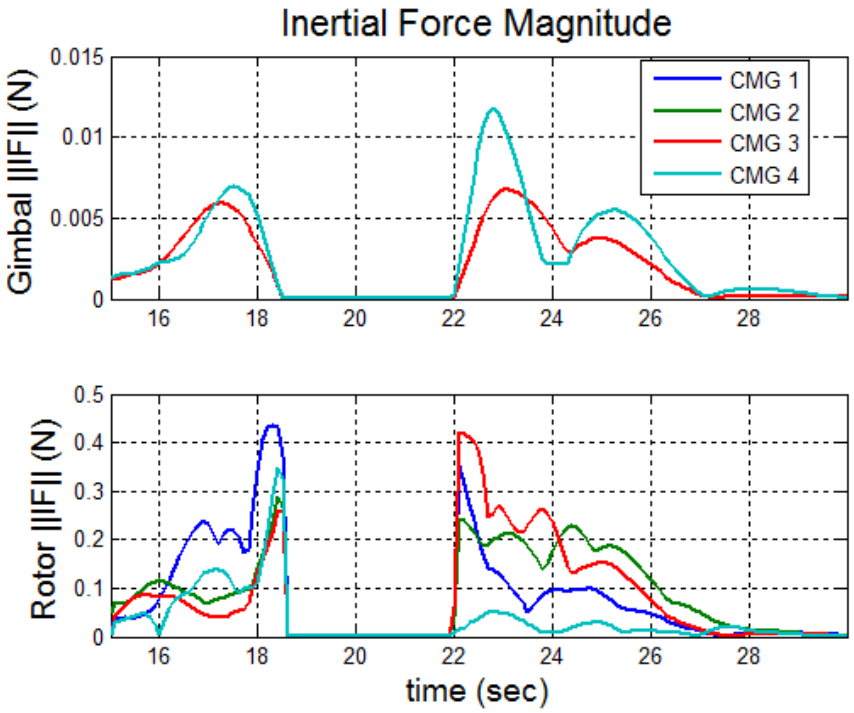

Figure 87. Inertial force magnitudes from the CMG force analysis optimal slew

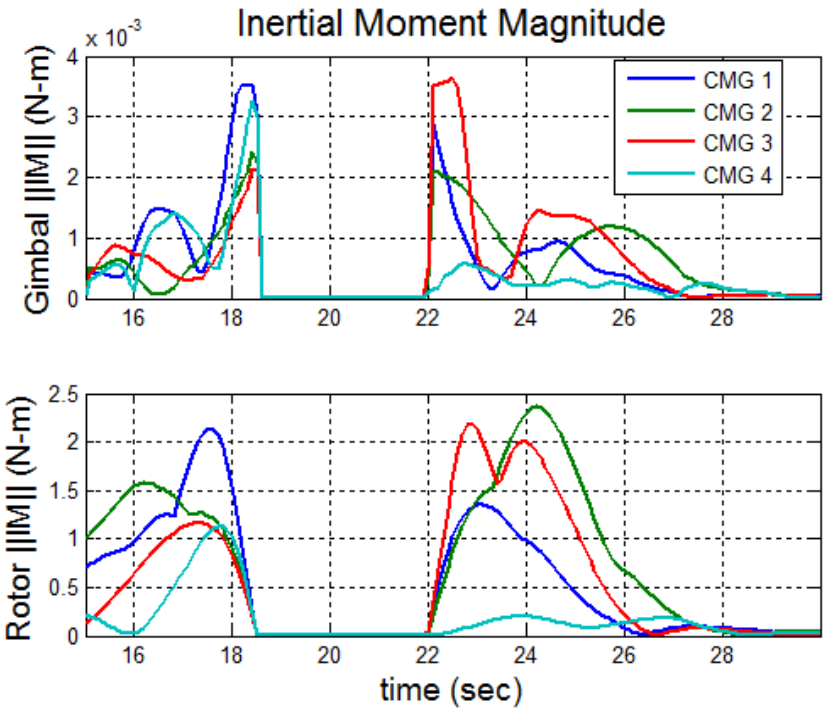

Figure 88. Inertial moment magnitudes from the CMG force analysis optimal slew

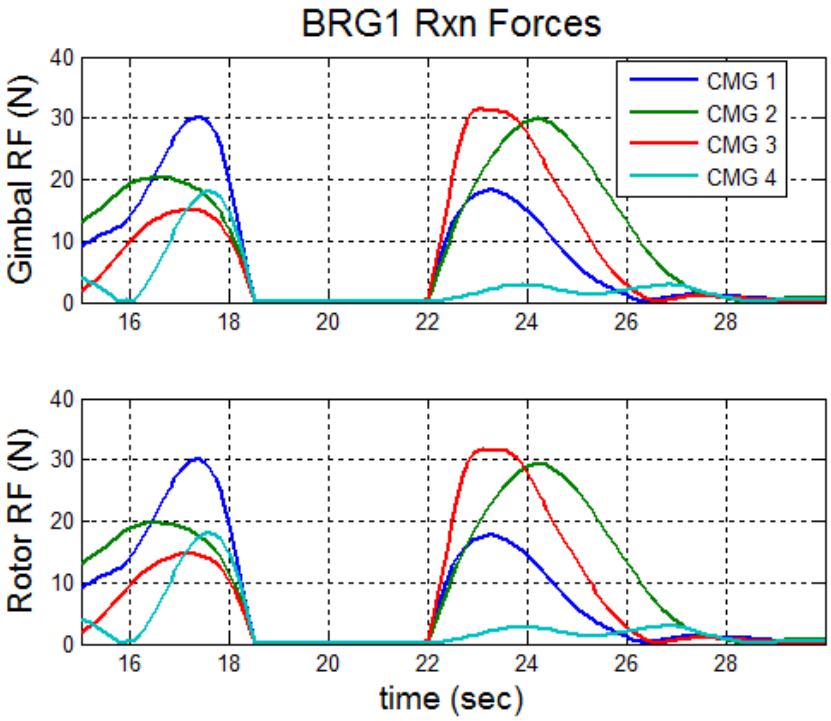

Figure 89. Bearing one reaction force magnitudes for the optimal slew

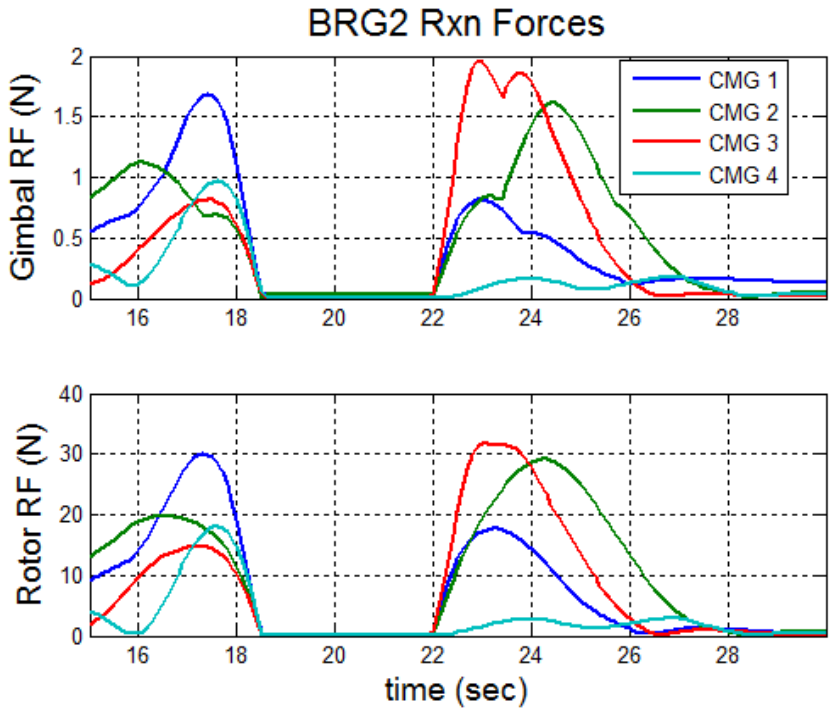

Figure 90. Bearing two reaction force magnitudes for the optimal slew

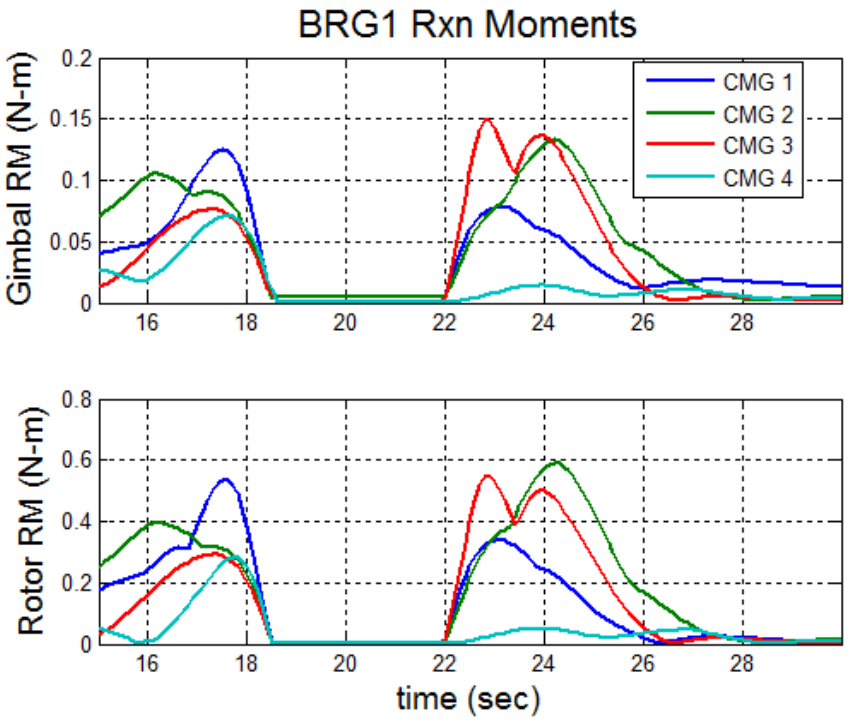

Figure 91. Bearing one reaction moment magnitudes for the optimal slew

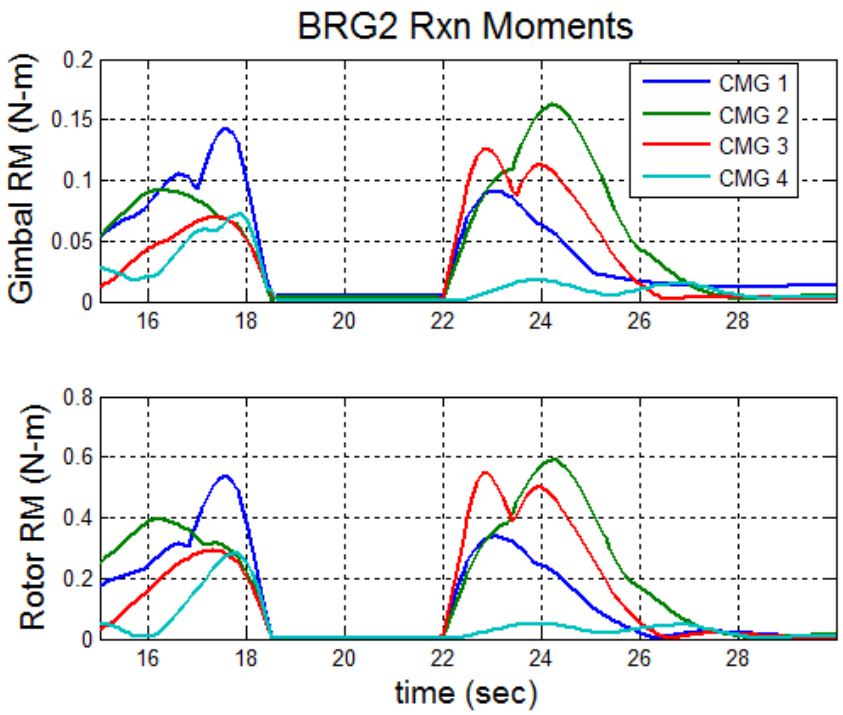

Figure 92. Bearing two reaction moment magnitudes for the optimal slew

Contrary to what was seen for the RWs where the peak measurements between the control cases were roughly equal, the peak reaction forces for the eigenaxis maneuvers are slightly larger than those seen during the optimal maneuvers. The optimal maneuver, however, maintains the reaction force for a larger amount of time while the eigenaxis maneuver introduces more abrupt force changes. The same trend is seen for the reaction moments. This indicates that, for this particular maneuver with this particular geometry, the optimal controller is easier on the components than the eigenaxis maneuver.

D. SUMMARY

Chapter VI presented a series of applications of the equations and algorithms derived in the prior chapters. Overall, the algorithms were shown to be able to rapidly analyze many different variations on a potential ACS, as well as the ability to analyze maneuvers to determine expected reaction forces and moments using only MED geometry and standard telemetry data, allowing for comparison of different controllers and different array geometries.

1. Momentum Envelope

For the RW momentum envelopes, the equations were validated by analyzing the geometry of the momentum spaces with the geometry of different arrays. Additionally, an analysis was performed on the effect of rotor imbalance and indicated that, for expected imbalance magnitudes, there was essentially no performance loss in the array.

The CMG MIA analysis was effective in rapidly generating a highly detailed maximum momentum space for different CMG array geometries. The associated angle residual plots gave an indication where interior singularity surfaces met the maximum surface.

Finally, the algorithms were used to generate a maximum momentum envelope for a hybrid RW/CMG array by summing the individually generated RW array momentum envelopes and CMG array envelopes. This resulted in the possibility of estimating the hybrid array performance with respect to spacecraft slews as well as introducing the idea of adding RWs to a CMG array to allow the CMGs to steer

around elliptic singularities thus allowing expanded utilization of the CMG performance envelope.

2. Torque Envelopes

The torque envelope was shown to be of the same shape as the momentum envelope for RW arrays.

For CMG arrays, the state space analysis algorithms were implemented and used to generate singularity free momentum spaces. It was discovered that the current state space analysis methods resulted in a momentum envelope that allowed about 12% of the capability of current CMG array capability for the semi-adjacent analysis, and about 6% for the fully adjacent analysis. This had several causes, the primary one being that the current performance metric is based on including hyperbolic singularities while the state space analyses excluded all singularities. A theoretical control algorithm was presented, and an initial test was performed showing that both the control algorithm concept was valid and the momentum space held no singularities along the trajectory.

3. Reaction Force Analysis

The developed equations were validated for RWs and CMGs using simple test cases. Third party simulators were used to generate telemetry to analyze different controllers, analyze different RW and CMG construction assumptions and prove the feasibility of using third-party telemetry for the analysis.

For both RW and CMG arrays, an eigenaxis slew and an optimal slew were analyzed. For the RW analyses, peak force and moment magnitudes were roughly equal. The

optimal slew operated the RWs at a higher duty cycle, but provided a much smoother reaction force and moment history. The eigenaxis slew tended to create abrupt changes in the reaction forces seen on the system.

For the CMG arrays, the peak magnitudes for the optimal maneuver were less than for the eigenaxis maneuver. The smoothness seen in the RW analysis carried over to the CMGs for the optimal maneuver, and the abrupt applications of relatively large forces and moments was even larger for the CMG case than the RW case.

THIS PAGE INTENTIONALLY LEFT BLANK

VII. CONCLUSIONS AND FUTURE WORK

A. CONCLUSIONS

The goal of this thesis was to develop the equations and algorithms necessary to automate the analysis of MED arrays for the purpose of ACS design and analysis. This involved looking at three specific areas: momentum envelope analysis, torque envelope analysis, and reaction force and moment analysis.

For RWs, a simple matrix equation, Equation (23), was developed that can rapidly create a point cloud of momentum states. This provided a means to estimate possible ACS performance based on the minimum momentum point on the maximum surface. This, in turn, allowed array geometry or the physical characteristics of the RW (such as inertia tensor or maximum wheel speed) to be varied and the result of this variance with respect to array performance to be analyzed. It was also shown that the RW torque space has the same shape as the RW momentum space, with the torque space magnitude being defined by the maximum wheel accelerations.

For CMGs, the MIA process was developed to rapidly analyze the maximum momentum surface by removing the need to perform a sweep analysis through all gimbal angle combinations. It also provided an indication of where interior singular surfaces meet the maximal momentum surface via an angle residual plot.

When analyzing torque space, it was shown that CMG arrays produce torque that is state dependent. This led to the development of the state space analysis in order to

generate singularity free momentum spaces by limiting the gimbal angles of each CMG in the array. The idea of contiguousness was introduced to ensure that an enclosed area within the reduced dimensional state space analysis map would only contain states that yield a realizable gimbal angle trajectory. Both of the two primary state space analyses, reduced dimensional and full dimensional, successfully created singularity free spaces.

The reaction force and moment analysis involved a topic that had received little discussion in the researched literature. The equations were developed using a combination of first principle derivations and standard reference tables. The analysis was formulated such that common telemetry data and known MED array geometry, consistent with the previous momentum and torque analyses, would be sufficient to solve the equations. Results from the verification and validation tests showed expected trends and provided useful relationships between MED geometry changes and resulting reaction force/moment changes. Initial telemetry testing indicated that optimal controllers and eigenaxis controllers created reaction forces and moments that were of the same magnitude for RWs, while for CMGs the optimal controller showed smaller force and moment magnitudes. Additionally, eigenaxis controllers tended to impact the system with sudden, large forces and moments while the optimal controllers resulted in smoother reaction forces and moments. In all cases, the average duty cycle of all MEDs operating with the optimal controllers was higher than the average duty cycle under the eigenaxis controllers.

Overall, this thesis showed that automated analyses for generic MED arrays was feasible, and should prove useful for the rapid iteration of initial ACS design.

B. FUTURE WORK

Although the goal of developing algorithms to rapidly analyze arrays of RWs and CMGs was achieved, there are several additional features that can be added to improve analysis fidelity and usefulness.

1. Momentum Analysis

- Very tight tolerances in fly-wheel balancing are required to ensure the long life of RWs and CMGs. This does allow for some imbalances, however, and could impact the performance of platforms that require very tight pointing requirements. Especially for RWs, it would be useful to modify Equation (28) so that it included tracking of RW frame rotation as the wheel rotates.
- For CMGs, the rotor provides the bulk of the component's momentum. The rotation of the gimbal, however, adds some momentum and this should be included as part of the analysis. This may also benefit the singularity free state space analysis as it would then provide for the possibility of angular momentum vectors outside the plane of rotation.
- The maximal surface detection algorithm is a very rudimentary one that sections a unit sphere and finds the point furthest from the point in any given section. Anomalies can present themselves at the north and south poles of the sphere. A voxel-based approach could provide a more robust solution as well as a possible performance improvement.
- Though the momentum algorithm can easily be used to find the extreme vertices of a RW momentum envelope, identification of connected points must be done manually. Automating this task would

provide an extremely rapid creation of the edges of the geometry.

- The generation of the quasi-maximum space for a hybrid array currently depends on a very simplistic method examining every CMG point, finding the nearest RW point and adding the momentum values, subject to an angle-error constraint. Due to the highly irregular distribution of the RW points and the very regular distribution of CMG points, there can often be a miss where a CMG point has no corresponding RW point. Due to the geometrically simple shape of RW momentum spaces, it should be possible to determine the momentum value at any point on the surface and add that value to the CMG point.
- Further analysis should be conducted to determine the reasonableness of including small RWs with a CMG array to allow torque-free elliptic singularity avoidance within the entire CMG momentum space.

2. Torque Analysis

- The box/hypercube singularity free search algorithm misses a significant amount of adjacent singularity free space due to the simplicity of implementation for both the search algorithm and the resulting singularity free momentum space analysis. This unnecessarily restricts CMG capability. An improved search algorithm would restore some of the lost performance.
- Due to the numerical nature of the singularity free space created by the state space analysis, another method must be developed to verify that the space is actually singularity free. Ideally, this could be done analytically as it would possibly allow an analytic determination of allowable gimbal angle ranges, obviating the need for a numerical analysis.
- Adding limited gimbal angles to the momentum inversion algorithm would allow the singularity-free momentum space to be created with the same method as the normal maximal surface.

- Further development of the control law in Equation (94) would allow full utilization of the singularity free space provided by the gimbal angle limitations.

3. Reaction Analysis

- The value of the variables and parameters involved in the force analysis can vary across many orders of magnitude. To prevent the insertion of numerical errors when performing arithmetic between very large and very small numbers, scaling should be introduced to the equations.
- The simplified model may not accurately model the physical MEDs. Further analysis should be performed to improve the simplifications.
- The design of a MED array could be optimized for a specific mission by assuming the operating regime of a spacecraft and designing the MED based on the calculated loads

THIS PAGE INTENTIONALLY LEFT BLANK

LIST OF REFERENCES

[1] H. Schaub and J. L. Junkins, *Analytical Mechanics of Space Systems*. Reston, VA: AIAA, 2003.

[2] P.C. Hughes, *Spacecraft Attitude Dynamics*. Mineola, NY: Dover Publications, Inc., 1986.

[3] P.W. Likins, *Elements of Engineering Mechanics*. New York: McGraw-Hill, 1973.

[4] S.R. Crews, "Increasing slew performance of reaction wheel attitude control systems," M.S. thesis, Mech. and Aero. Eng. Dept., NPS, Monterey, CA, 2013.

[5] M.H. Kaplan, *Modern Spacecraft Dynamics & Control.* New York: John Wiley & Sons, 1976.

[6] F.L. Markley, R.G. Reynolds, F.X. Liu, and K.L. Lebsock, "Maximum torque and momentum envelopes for reaction wheel arrays," *J. of Guidance, Control, and Dynamics*. Vol. 33, No. 5, pp. 1606-1614, 2010.

[7] G. Margulies and J.N. Aubrun, "Geometric theory of single-gimbal control moment gyro systems," The *J. of the Astronautical Sciences*. Vol. 26, No. 2, pp. 159-191, Apr.-Jun. 1978.

[8] B. Wie, *Space Vehicle Dynamics and Control*, 2nd ed. Reston, VA: AIAA, 2008.

[9] B. Wie, D. Bailey, and C Heiberg, "Singularity robust steering logic for redundant single-gimbal control moment gyros," *J. of Guidance, Control, and Dynamics*. Vol. 24, No. 5, pp. 865–872, Sep.-Oct. 2001.

[10] H. Kurokawa, "A geometric study of single gimbal control moment gyros singularity problems and steering law," Mechanical Engineering Lab. TR 175, Tsukuba, Japan, Jan. 1998.

[11] J.A. Paradiso, "A search-based approach to steering single gimbaled CMGs," Draper Lab. Cambridge, MA, Mar. 1991.

[12] T.A. Sands, J.J. Kim, and B. Agrawal, “2H singularity free momentum generation with non-redundant single gimbaled control moment gyroscopes,” in *IEEE Conf. on Decision and Control*, San Diego, CA, 2006 pp. 1551-1556.

[13] W.C. Young, R.G. Budynas, and A.M. Sadegh, *Roark’s Formulas for Stress and Strain, Eighth Edition.* New York: McGraw-Hill 2012.

[14] K.L. Ackman, “Prototyping of an open-architecture CMG system,” M.S. thesis, Mech. and Aero. Eng. Dept., NPS, Monterey, CA, 2012.

[15] E.J. van der Keide, R. Ferreira, P. van Put, and P. Le, “Reaction wheels at Bradford Engineering,” in *8^{th} International ESA Conf. on Guidance, Navigation, and Control Systems*, Karlovy Vary, Czech Republic, 5–10 Jun. 2011, pp. 1–10.

[16] X. Chen and J. Ji, “The minimum-norm least-squares solution of a linear system and symmetric rank-one updates,” *J. of Linear Algebra*. Vol. 22, pp. 480-489, 2011.

[17] B. Wie, “Singularity analysis and visualization for single-gimbal control moment gyro systems,” *J. of Guidance, Control, and Dynamics*. Vol. 27, No. 2, pp. 271–282, Mar.-Apr. 2004.

INITIAL DISTRIBUTION LIST

1. Defense Technical Information Center
   Ft. Belvoir, Virginia

2. Dudley Knox Library
   Naval Postgraduate School
   Monterey, California